Identifying and characterising post-encounter disintegrating systems

Alexandra Ka Po Yip

Instituto de Física y Astronomía
Facultad de Ciencias

Universidad de Valparaíso
Doctorado en Astrofísica

Julio 2023
Valparaíso. Chile.

I dedicate this work to science, as it is my dream to make a contribution to it, as well as my way to give back to society.

This thesis is solely my own composition,
except where specifically indicated in the text.

Alexandra Ka Po Yip
Julio 2023.
Valparaíso. Chile.

Acknowledgements

A massive thanks to Professor Radostin Kurtev, my principal supervisor, who allowed me to work on this very interesting Ph.D project. Thank you very much for hanging in there with me this whole time, even when, for a while, things were not looking too promising due to various reasons on my end. I would also like to thank Professor David Pinfield, who was the principal supervisor of my MSc. I will be forever grateful for the opportunity you gave me, and for introducing me to such fascinating science, which eventually inspired my Ph.D project. I also cannot be more thankful to Dr. Federico Marocco's full support during this entire programme. You were always there any time I needed help, and I will always appreciate your understanding, kindness and clear guidance to say the least. I would also like to thank Dr. Julio Carballo Bello for the help with my DECam data reduction and the thorough feedback on the draft of my first paper, which improved the article and contributed to making the peer review process much faster and smoother. I am also very thankful to the Proyecto CONICYT-REDES140024, "SOCHIAS grant through ALMA/Conicyt Project 31150039" and Ministry of Economy, Development, and Tourism's Millennium Science Initiative through grant IC120009, awarded to The Millennium Institute of Astrophysics, MAS for the financial support. I am extremely grateful as you have granted me the possibility to carry on chasing, and coming a step closer, to my childhood dream.

Thank you very much to Professor Verónica Motta and Professor Mónica Zorotovic for assisting and guiding me with the application for the program extension, at a time when I was undergoing a very difficult period in my life. I would also like to express my thanks to Professor Jura Borissova, for making sure that I was being paid timely at the beginning of the programme, so I did not have to survive on "manzana y agua" alone. Big thanks to Dr. Mariusz Gromadzki, also known as my "big brother", who helped me to get started with my project, and to settle down when I first arrived in Valparaiso. Furthermore, I really appreciate all the help with providing documentations and advises from the amazingly helpful staff of the Centre of Astrophysics Research (CAR) of the University of Hertfordshire, who helped me get through some

of the bureaucracy while I was in Chile.

I am very thankful to María Isabel Figueroa Zavala, also known as Bel Bel. You have played a very big and important role during my time in Valparaiso. You were already looking out for me the instant you met me; you are very trustworthy, and you have never let me down. I consider myself very lucky to have ever met you. Edgar Sanders, I would like to thank you for the truly excellent technical support you provided. You are also such a polite, down to earth and well balance person and very enjoyable to chat with. Thank you very much also to Pamela Caballero for showing me that lovely tea house for macaroons and taking me out to celebrate New Year and more. I would also like to thank Josefina Morales for being so lovely and sweet all the time, seeing you around always put a smile on my face.

Juan Magaña, you are a very important colleague and friend. I am beyond thankful for your help in general, but in particular for the time I have accidentally injured myself. You were like a hero to the rescue, and you were there for me the whole time attending all necessary aids I required and more. Further, I really enjoyed our coffee time together and whenever we hang out. You are always very funny, extremely generous, with tremendous patience and good temper. I still remember that surprise birthday celebration for me with Andreina Mariel. It meant a lot to me, and I had a great time. I also still remember the 'correct' chicken wings you promised you would cook for me, but failed to do so. I can assure you I will be holding a grudge on it for all eternity. I would also like to thank Javier Arancibia for being such a lovely friend. I remember an occasion when you have attempted to cater for me, some delightfully "drinkable" pasta which I had a very interesting time consuming. Daniela Iglesias, I would like to thank you for patiently trying to teach me how to roll the "R", which unfortunately I am still not very good at. You are very kind and helped me buy skincare, and being very generous you presented me with some skincare gifts which I liked a lot. All in all, I would like to express my thanks to all the very helpful and friendly colleagues from the Instituto de Física y Astronomía (IFA), whether they have been explicitly mentioned here or not.

When I first moved to Chile, I found myself in a place that I knew very little about, and of which I did not speak the language. Therefore, I am very grateful to have met a lot of amazing people who helped me settle in. I cannot thank Prof. Michel Curé's mum enough for letting me stay at her place and taking great care of me when I first landed. I am very thankful for the wonderful food you offered, introducing me to the first taste of Chile. I rather enjoyed it. I am also very grateful for your reassurance, and for showing me around when I was very new to the environment. Lorena Rivera

Cisternas, thank you very much for looking after me not long after I first arrived. I really enjoyed the food that you made for me, and I have a lot of fun hanging out with you. I am forever grateful for your comforting and looking out for me. You have also inspired me to learn Spanish, which eventually became very useful.

Thank you very much, Velia Lutjens Depolo, for all the good times we had together. The family BBQ at Christmas, the open Karaoke bar at your birthday, a lot of new experiences that I would have never had if it were not thanks to you. I still cannot forget about that best croissant with cream that you gave me, and all the other little surprise gifts from you which I really liked. I will always appreciate your sweet thoughts. Fernando Hinostroza, you are for sure one of my best friends over there, and I will always be very thankful for getting to know you. I remember we used to spend a lot of time together in person and on the phone as I really like your personality. I think you are a very clever and thoughtful gentlemen which is also very nice to chat with and fun to jam with. The video of a stray dog rejecting the food you offer it from that sushi place still makes me laugh to this day. I would also like to thank Lijuan Wang for being such a good friend. I had a blast hanging out with you and have learned so much from you. You are a genuine person with real emotions and are always true to your feelings. You are also very generous and thoughtful. I still remember you told me once about the person who would peel prawn for you and that prawn dish you made for me, and I am forever grateful to you. Tata and Tota, if I could speak the language of cats I would very much like to thank you two for that extra little "colour" and all the shenanigans added to my stay in Chile. You two are very special to me and will always be in my heart wherever I go.

Once upon a time I thought out of all the relatives I have got there would be more that I would like to explicitly mention in this thesis. I am beyond grateful for all the extremely generous help I have received from them, and I can beyond any doubt say that they played a very crucial role at this juncture in my life. However, this down time in my life lasted much longer than I would have liked, and I understand why most people eventually lost faith in me. Yet I am still thankful to them regardless. Uncle Alfred is the only one who did not doubt me, and still believed in me this whole time, so I really want to give him an extra big shout out here. Thank you very much, I really appreciate your support a lot, much more then you can ever imagine.

Finally, I would just simply like to thank Melody Wong for being the most understanding and supportive friend in my life, always. Although I often fail spectacularly at remembering your birthday year after year, you are just accepting it like the Sun does rise every day.

I am very glad and grateful to have you all walk alongside me in my Ph.D. journey. May every one of you still be in the following chapters of my life, so that we can have many more wonderful times together.

Abstract

Disintegrating multiple systems are thought to be very common based on numerical simulations, which predict that 50% to 95% of non-hierarchical triple systems and 10% of hierarchical triple systems undergo an ejection at some point in their evolution. However, very few of these systems have so far been observed. Kinematic studies of the *Hipparcos* catalogue have revealed only 10 disintegrating triple candidates. They are presumably the result of dynamical encounters taking place in the Galactic disk between single/multiple systems. In this thesis, I expanded the search for such systems to study their properties, as well as to characterize possible low-mass ejecta (i.e. brown dwarfs and planets). I have assembled a list of 20 candidate systems using astrometry from the Tycho-Gaia astrometric solution (later upgraded with *Gaia* DR3), and here I present the follow-up of 9 of them. I have obtained medium-resolution spectra for 4 of them and used the spectra to determine their radial velocity and metallicity. These measurements allowed me to conclude that two of the systems observed with ISIS are likely genuine disintegrating systems, for which I have reconstructed the most probable interaction scenario. I have obtained DECam imaging for 5 systems and by combining near-infrared photometry and proper motion, I searched for ultra-cool ejected components. I found that the system consisting of TYC 7731-1951-1, TYC 7731-2128-1 AB, and TYC 7731-1995-1ABC?, contains one very promising ultra-cool dwarf candidate. Using additional data from the literature, I have found that 3 out of the 5 disintegrating system candidates observed with DECam are likely to be true disintegrating systems. Overall, this thesis demonstrates the feasibility of searching for disintegrating multiple systems with the method described, as well as the feasibility of identifying additional low-mass ejected components. Future Gaia data releases and upcoming large area near-infrared surveys and new space telescopes (e.g. LSST, EUCLID, SPHEREX, NEOSurveyor) will enable me to search for even larger samples of disintegrating systems and more low-mass ejecta. This population will be fundamental to observationally constrain the rate at which this type of systems interact in the Galactic disk. The fundamental importance of searching for possible disintegrating

multiple systems is its contribution in providing further constraints to the formation models of binaries and multiple systems and their evolution.

Contents

CHAPTER 1

Background

1.1 Introduction

Disintegrating multiple systems can further our understanding of the formation and evolution of binaries and multiple systems (e.g. Szebehely, 1972). This in turn can help us paint a more complete picture of the process of star formation (Reipurth, 2000). In certain circumstances, when a binary or multiple system interacts with another close by star or multiple system the binding energy between the components can be gradually reduced, causing one or more of the components to become unbound. Wide binaries and multiple systems have a large cross-section, so they are more likely to interact with stellar or substellar objects. Usually, such interactions are relatively weak, but occasionally there are more violent interactions that can lead to the break-up of the system or all of the systems involved (Heggie, 1975; Weinberg et al., 1987).

Disintegrating systems are expected to be common (Li et al., 2009), but the average time for disintegration is short, approximately 1 Myr (Szebehely, 1972). Therefore, disintegrating systems are very difficult to find. Studies in this field have generally focused on kinematic studies (e.g. Retterer & King, 1982) or numerical simulations (e.g. Mikkola, 1983; Weinberg et al., 1987), but overall they have so far been limited. Marchal (1990) developed an analytical technique to identify escaped objects from N-body systems. The technique, known as Marchal's test, involves only a one-dimensional projected motion vector of the system at any given time. This makes it very useful

to study stellar systems of which the full motion vectors are unknown. Later, Li et al. (2009) attempted to adapt the Marchal's test to triple stars from the *HIgh Precision PARallax COllecting Satellite* catalogue (HIPPARCOS; Perryman et al., 1997; van Leeuwen, 2007).

Triple systems in hierarchical configuration (i.e. with two stars forming a tight pair and a third component on a wide orbit) are found to be more common than those in random arrangements (van den Berk et al., 2007; Toonen et al., 2016). This suggests that systems not in hierarchical configuration are unstable or, at least, less stable than hierarchical systems. Nevertheless, hierarchical systems can become unstable too. Numerical simulations on systems with hierarchical configurations have shown that $\sim$95% of them have had an ejection in their life-time (e.g. Anosova, 1990). Moreover, triple systems can form via binary-binary interactions, leading to the ejection of one of the components of the original binaries (Saslaw et al., 1974). This is inferred from the dynamical evolution of stellar clusters (e.g. Aarseth, 2003, 2004) and is predicted by numerical simulations on binary-binary encounters (Mikkola, 1983). Finally, since the hierarchical configuration appears to be the more stable layout, newly formed triple systems rearrange into a hierarchical arrangement shortly after their formation (Li et al., 2009). Therefore, many of the hierarchical triple systems we observe today are likely to reach a disintegration phase shortly or to be undergoing that process currently. The Marchal's test is not universally applicable. For example, in the case of binary-third body systems, their period often exceeds the baseline covered by available observations, therefore leading to unreliable orbital solutions (Lattanzi et al., 2005). Multiple systems can also disintegrate as a result of the evolution of one of the components from main sequence star to white dwarf (Veras et al., 2014; El-Badry & Rix, 2018). Wide binaries and multiple systems are particularly vulnerable (Veras et al., 2014), because the binding energy of the system is low and therefore even weaker interactions such as Galactic tides can lead to a break up.

Studies of disintegrating multiple systems need very precise parallaxes and proper motions (hereafter PM) to be able to distinguish between genuine systems and mere chance alignments. The lack of such measurements has limited the studies of these important systems, but now with the advent of Gaia (Gaia Collaboration et al., 2016a, 2021) there has never been a better time to look for such extremely rare yet unquestionably interesting systems. Using Gaia DR2, Bailer-Jones et al. (2018) searched for possible close encounter to the Solar System and found that on average our own Sun has 19.7$\pm$2.2 encounters within 1 parsec every million years. Therefore, studying dis-

integrating multiple systems can also provide us fundamental information on the risk of possible disruption to our own Solar System due to these close encounters.

1.2 Multiple systems

When two stars in a star system orbit around their common centre of mass as a result of the gravitational pull/interaction between them, they are called a "binary star". The same principle applies to multiple systems. The brighter/more massive star between the two is called "primary" and the dimmer/less massive one is called "secondary" or "companion" star. The secondary could be either a substellar object or a main-sequence star. There is observational evidence from the study of a few pre-main-sequence systems indicating a strong likelihood for both components to be born very closely in time, with a maximum difference of about 10^6 years (e.g. Bodenheimer et al., 1993; Strom, 1991). The secondary shares the same metallicity as well as the same age of the primary, given they both originate in a short time interval, giving extra constraints on its composition and mass (e.g. Burgasser et al., 2000). Furthermore, if the components are consistent with having equal brightness, this implies that they are likely to be a near equal mass binary. There is evidence that binary systems (independently of their range of orbital periods) and isolated young stars are more likely to have a disk around them (Mathieu, 1992).

One of the fundamental goals for this project is to look for disintegrating multiple systems, which are considered to be extremely rare. The estimated fraction of single stars is approximately 2/3 of the total stellar population of the Milky Way, while 1/3 of it consists of binaries or multiple star systems (Lada, 2006; Offner et al., 2022). Moreover, hierarchical multiple systems are relatively common and, according to Fekel (1981), most of their period ratios are usually within the range of 10–10^4. To improve the understanding of these binary/multiple systems, various observational facts such as the non-negligible occurrence of multiple systems, the overall binary frequency, as well as the distributions of eccentricity, period, and mass ratio among the individual binaries are still awaiting to be fully constrained.

In addition, the star formation process can also be tested by the observation of binary properties. Dynamical interactions, star formation and even the origin of Galactic field stars can be deduced from the chief characteristics of multiple systems, e.g. mass ratio, separation distribution and multiplicity fraction. For orbital separations in diverse ranges, close-by M dwarfs (that have low luminosity and high PM) allow the

identification of multiple systems and co-moving binaries with very low-mass components. The first type of these low-mass components are brown dwarfs (hereafter BDs), which have masses below the hydrogen burning limit (i.e. below 75 $M_{\rm Jup}$ for solar metallicity) that separates them from the low-mass stars (hereafter LMSs). Giant extra-solar planets (hereafter GESPs) are the second type of these low-mass components, and they are defined via the deuterium burning limit (mass $< 13 M_{\rm Jup}$) separating them from the BDs. Initial studies focused mainly on solar-type stars (Duquennoy & Mayor, 1991; Raghavan et al., 2010) but were subsequently expanded with the first informative study of M dwarfs (Fischer & Marcy, 1992) and also of A-type stars (De Rosa et al., 2014). The advent of Gaia (Gaia Collaboration et al., 2016a) has provided much larger and more complete samples of binaries spanning the entire mass range, allowing for on-going, more comprehensive studies of the population of multiple systems (e.g. El-Badry & Rix, 2018; Hawkins et al., 2020; Hartman & Lépine, 2020; El-Badry et al., 2021; Gaia Collaboration et al., 2022a). The binary fraction of the least massive stellar objects (also the most common stellar population) became more accurate thanks to these studies that looked for binaries consisting of components with various masses. This is fundamental to understand the formation and nature of stellar and substellar binaries. Brief background/properties of these binary/multiple systems will be presented in the following sections.

1.2.1 General properties

Observational classification of binary systems

Overall, there are four main types of binaries, each one further divided into a variety of sub-types. The first main type is the Visual Binaries (e.g. the Mizar system), where the periodic motion of one or both components is observable in the sky (e.g. Dupuy & Liu, 2012; Pearce et al., 2020). One variety of this type is called Astrometric Binaries when only the motion of one star is visible, and the other component cannot be directly observed (Penoyre et al., 2022). Astrophysicists can obtain their orbital pattern (e.g. Söderhjelm, 1999; Malkov et al., 2012; Chulkov & Malkov, 2022), but a lot of them have very long orbital periods of a few centuries (or even millennia), leading to poorly known or very uncertain orbits. A way to estimate the orbital period for a wide binary is to use Kepler's third law, i.e. $4\pi^2 a^3 = G(M_1 + M_2)P^2$, where a is the semi-major axis of the orbit, G is the gravitational constant, M_1 and M_2 are the masses of the two stars, and P is the orbital period. This method relies on the assumption that a is equal

to the projected separation (since one cannot measure a directly) so it can only lead to a lower limit on the period.

Another way in which binaries can be detected is via indirect techniques such as spectroscopy. The binary components' orbital motion causes periodic Doppler shifts, which are detectable in one or more spectral lines, hence the name Spectroscopic Binaries. When the Doppler shifts are measurable for both binary components, then the system is called double-lined spectroscopic binary (Struve & Huang, 1958). Otherwise, the system is named single-lined spectroscopic binary when only one of the component's Doppler shift can be measured (Struve & Huang, 1958). In addition, the time variation of these spectroscopic binaries' spectrum can also be obtained (e.g. Burgasser et al., 2010).

Another type of binary systems is the Eclipsing binaries, where during part of the orbit, one star eclipses the other, i.e. one star passes in front of the other, causing a significant variation in the light output for the system. The binary will only eclipse if the orbital plane is aligned with the line of sight, or if it is tilted by a very small angle. If the orbit is tilted by a large angle, then the binary will not eclipse. This type of binaries is fundamental to determine the basic stellar parameters of stars, i.e. mass and radius (e.g. Pols et al., 1997; Prša et al., 2011; Kirk et al., 2016).

The last main type of binary systems is the Photometric Binaries, where the colour or flux of the system appears to have a periodic variation (e.g. Tal-Or et al., 2015). There are three ways in which the components of non-eclipsing binaries that are close to each other can be affected, and this can be detected photometrically. Accurate photometry is necessary in order to search for these BEaming, Ellipsoidal, and Reflection binaries (BEER binaries; Faigler & Mazeh, 2011). Beaming binaries are systems where one can observe the effect on the apparent magnitude of the stellar objects due to relativistic beaming (Rybicki & Lightman, 1979; Maxted et al., 2000). This method is highly dependent on if the secondary component of the system is tiny and dim in comparison to the primary object. This will ensure the secondary cause no other effect on the primary. Only the speed at which the components are orbiting around each other is relevant in this case (Rybicki & Lightman, 1979). The second way in which the components of these binaries affect each other, in particular if one of the objects is exceptionally dense, is by causing the deformation of the shape of the stars. This effect can be distinguished by observing the variations of the light curve, and they are known as Ellipsoidal variables (Morris, 1985; Mazeh, 2008). Lastly, Reflection modulations in light curves induced by a short period companion is when the separation

between the stars is small enough, extra light from a star can be observed due to it reflecting from its companion (Maxted et al., 2002; Harrison et al., 2003; For et al., 2010; Reed et al., 2010). However, the three effects described here are not a reliable way to be certain that these systems are real binaries, as they can be confused with variable stars (e.g. Cepheids, RR Lyrae variables) since they can as well have similar periodic variations.

Ultimately, these binary systems are crucially important because astronomers can obtain the masses of their components by calculating their orbits (e.g. Konopacky et al., 2010; Malkov et al., 2012; Dupuy & Liu, 2017; Brandt et al., 2019). In addition, their subsequent evolution (Hurley et al., 2002, and references therein) and their formation (Boss, 1993) can be revealed by their orbit.

Orbital period properties and eccentricities of binary systems

Binary/multiple systems can either be so tight to the point where the components are almost in contact with each other ($\sim$ a few AU or less) or so far apart ($\sim$ a few hundreds of thousands AU) that one can only indicate that they are indeed in connection by looking at their common PM. Generally, the separation of binary/multiple systems determines their orbital period ($P_{\rm orb}$), ranging from $\sim$minutes to 10^6 yrs (Raghavan et al., 2010; Moe & Di Stefano, 2017). The larger the separation, the longer the $P_{\rm orb}$, and vice versa.

Duquennoy & Mayor (1991) were the first to find that the period distribution of main-sequence binaries in the range $-1 < \log P_{\rm orb}$ (days) < 10 is unimodal and best described by a Gaussian-type relation (a smooth distribution) with a median period of approximately 180 years. Fischer & Marcy (1992) later found a similar distribution of periods for multiple systems with M dwarf primaries. Figure 1.1 shows the period distribution for multiple systems with solar-type primaries determined by Raghavan et al. (2010). Their Gaussian fit to the distribution has a peak at $\log P_{\rm orb} = 5.03$ and a standard deviation of $\sigma \log P_{\rm orb} = 2.28$.

Moreover, given that binaries/multiple systems are likely to have formed with a wide range of eccentricities, there is also a relationship between the eccentricity of the orbit and the period of a binary star. Field main-sequence binary systems where the eccentricity is small and with a short period (i.e. $P_{\rm orb} < 12$ d), end up being circularized via tidal interactions, while if the separation between the components is wide, then a highly elliptical orbit is possible (Duquennoy & Mayor, 1991; Raghavan et al., 2010). The distribution of eccentricities for these systems is in general widely scat-

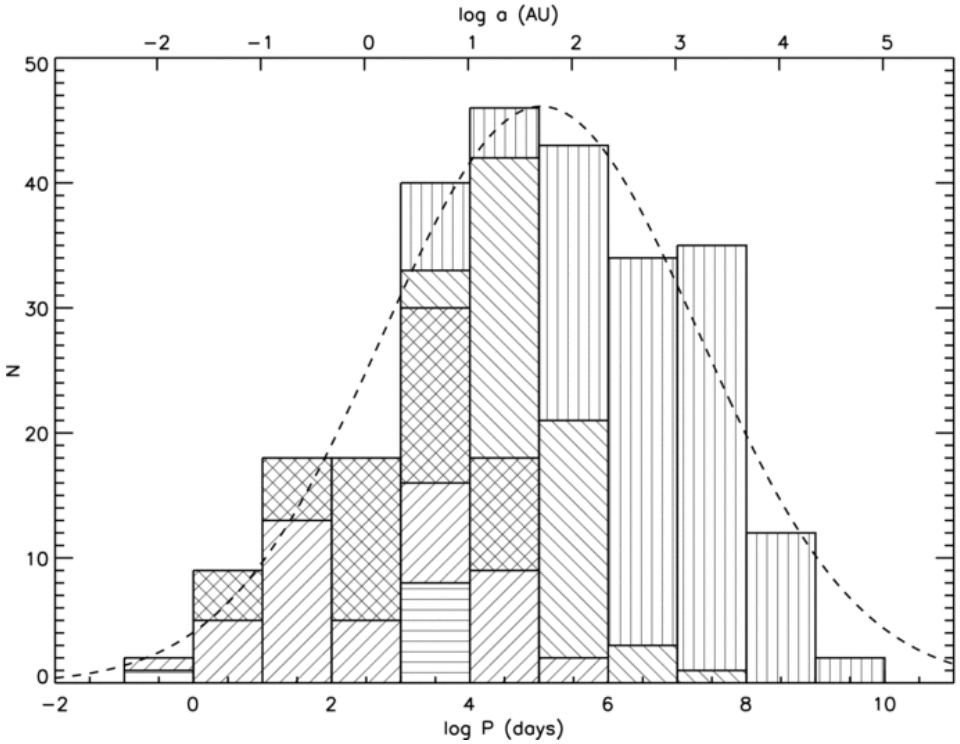

Figure 1.1: The period distribution for multiple systems with solar-type primaries determined by Raghavan et al. (2010). The dashed curve shows their Gaussian fit to the distribution, with a peak at log $P_{\rm orb}$ = 5.03 and standard deviation of σ log $P_{\rm orb}$ = 2.28.

tered ($e \equiv \sqrt{1 - b^2/a^2}$, where a is the semi-major axis and b is the semi-minor axis). Figure 1.2 shows an example for a population of multiple systems studied by Raghavan et al. (2010).

The eccentricities from well-determined orbits are essential to derive the angular momentum of the formation process. This information can then be used to estimate other stellar parameters indirectly, such as density and radius, and, in turn, mass. Mass is the fundamental property of any stellar object, since it can be used to determine its entire life history. On the other hand, some binary properties, i.e. multiplicity fraction, orbital semi-major axes, and mass ratio can be studied in a statistical way by using a large sample without information about orbital motion. These studies have given very important constraints on formation models at very low masses (e.g. Allen, 2007). An example can be seen in Figure 1.3, showing the period distribution of BD companions to main sequence stars. There is a clear lack of short-period binaries (i.e.

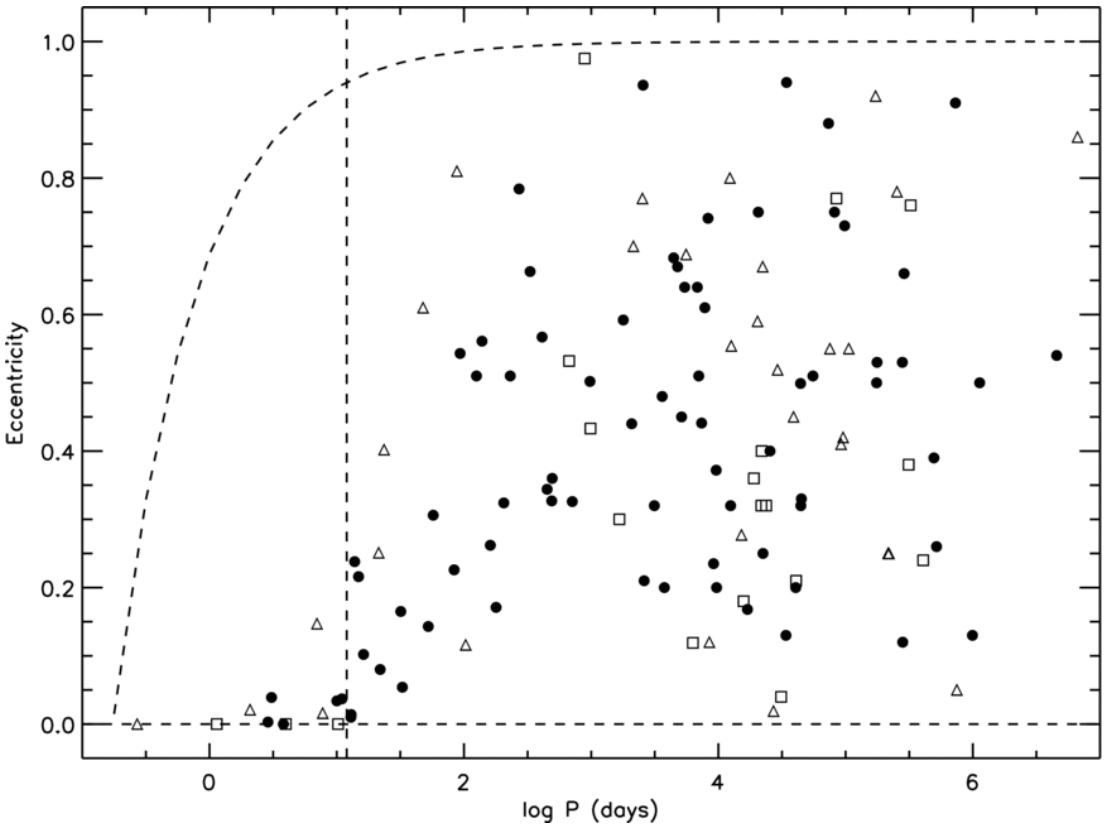

Figure 1.2: Period-eccentricity relationship for the 127 systems from Raghavan et al. (2010). Components of binaries are plotted as filled circles, of triples as open triangles, and of quadruple systems as open squares. The horizontal dashed line marks the zero-eccentricity limit (i.e. circular orbit) and the vertical dashed line marks the 12 day period limit, which roughly corresponds to the circularization period, i.e. systems with period shorter than 12 days will quickly evolve to have circular orbits. The dashed curve represents the merging boundary, i.e. pairs with eccentricity above this limit will pass within 1.5 $R_\odot$ of each other when they are at periastron, and are hence likely to collide and merge.

$P_{\rm orb} < 100$ days) compared to long period binaries (i.e. $100 < P_{\rm orb} < 10{,}000$ days). This is known as the "brown dwarf desert" (e.g. Ma & Ge, 2014; Stamatellos & Herczeg, 2015).

There are various explanations for this observation. One of which is based on the fact that the outer disk is more susceptible to gravitational instabilities, so objects that form at $a > 80$ AU could have masses beyond the deuterium burning limit of $\sim 13 M_{\rm Jup}$. However, the timescale required for such objects to be able to migrate into the inner regions of the disk exceeds the lifetime of the disk itself (Udry & Santos, 2007). Whereas if these BDs were to form in the more stable inner disk, more precisely within 5 AU of their companion star, another theory attempting to explain the existence of the BD desert suggests the possibility that those BDs end up becoming part of the central star due to inwards migration after their formation (Armitage & Bonnell, 2002). That being said, the potential migration after formation of those BD companions to FGK dwarfs could also be zero. Moreover, to be able to confirm this theory, supplementary knowledge regarding migration within a protoplanetary disk still needs to be acquired (Nelson, 2018). Note that during the formation of the more massive planets via core accretion, the rate of gas accretion declines due to the gap formation in the disk (Lubow et al., 1999). Given the disk also has a limited lifespan, this subsequently imposes a limit on the maximum mass that the low-mass companion can reach of approximately $10 M_{\rm Jup}$ (Lubow et al., 1999). Thus, it is highly unlikely for objects forming via core accretion to be able to reach the mass regime of BDs. Contrary to that, a theory suggests that eccentric perturbations in the disk could be triggered, hence largely reduce the effect of the presence of a gap, when the objects reach the mass range between $3 - 5 M_{\rm Jup}$ (Kley & Dirksen, 2006).

Mass ratio distribution

To have a reliable set of constraints on the formation models is fundamentally important to determine the possible dominant formation scenario for various stellar objects, especially very low-mass stars (hereafter VLMSs). The study of the properties of binaries and multiple systems provides the set of observational constraints necessary. The mass ratio distribution (i.e. q = M2/M1, where M1 is the primary and M2 is the secondary) is one of the properties of low-mass binaries that can provide appropriate constraints to the formation models. The distribution of q seems to be dependent on the mass regime, but the exact relation is not precisely determined yet. Generally, if the primary star is massive, then there is a much higher likelihood for the secondary to be

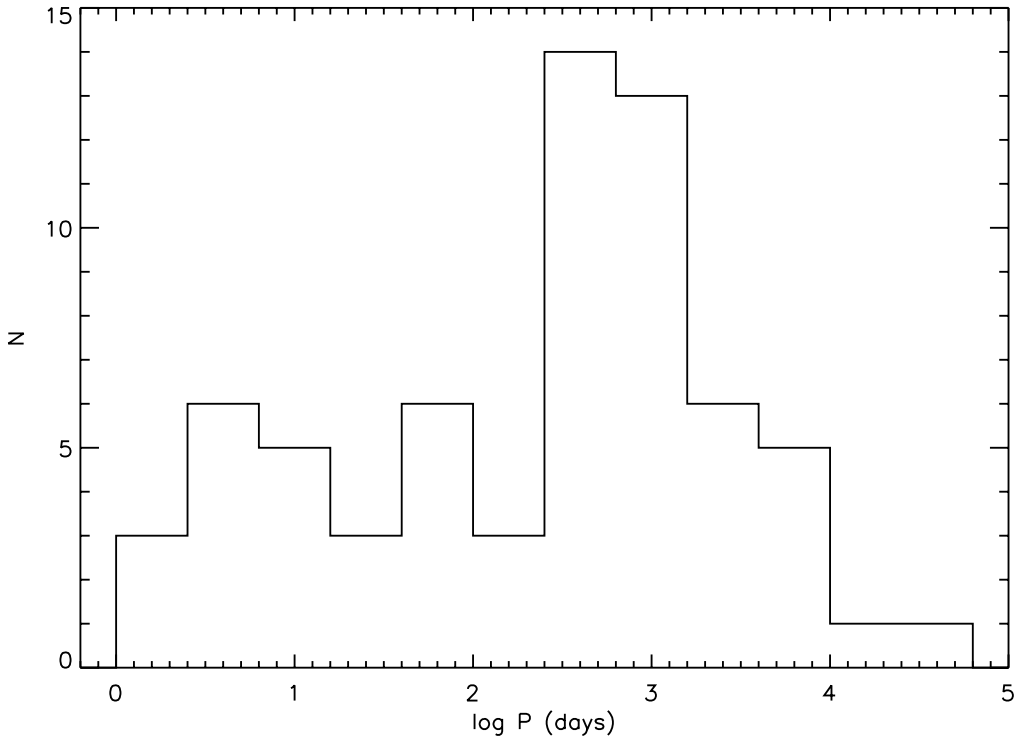

Figure 1.3: The period distribution of BDs companions to main sequence stars, from Ma & Ge (2014, their Figure 1). Long period binaries are much more numerous than short period binaries.

in a similar mass regime. However, there is not a similarly clear pattern for low-mass stars. Although the exact numbers are not known, binary surveys have suggested that massive stars have a higher fraction of interacting binary systems of 50% compared to lower mass objects, where the fraction is 30% (e.g. Duquennoy & Mayor, 1991; Kobulnicky & Fryer, 2007). The inconsistency in mass ratio distribution between massive stars and LMSs reveals a possible difference in the still uncovered formation process. Further, Abt (1983) suggested that by selecting random pairs from a population of objects, assuming that they follow the Salpeter IMF, their mass ratio distribution would match that for long period binary systems, or in other words there are more systems with long period that have small q than large q. Initially, this statement was disputed by both Duquennoy & Mayor (1991) and Halbwachs (1987), but further evidence suggests that there is indeed a relation between period and q as initially suggested by Abt (1983), for example as shown by Moe & Di Stefano (2017, see their Figure 30).

Moreover, the mass ratio between the components has an important role in determining the binary fraction, and at $q \sim 1$ is where the distribution peaks for all of the very low mass binaries discovered so far. The mass ratio distribution of very low mass binaries (spectral type $>$ M6) known to date is presented in Figure 1.4 (taken from Burgasser et al., 2007). The systems with age below 10 Myr are represented by shaded bins, with the number of binaries in each bin labelled.

It is important to bear in mind that there might be a bias in the selection of the observed mass ratios, leading to a less accurate separation distribution. Especially when the secondary is much less massive than the primary, then the possibility of measuring the radial velocity variation on the primary will be decreased. The option of direct imaging might also become unavailable as these objects are very likely too dim to carry out this technique. Such biases, however, are unlikely to affect the mass ratio peak at $\sim$1, as the majority of the modern spectroscopic and imaging surveys are capable of detecting very low mass binary systems with $q \gtrsim 0.5$. Given that over half of the confirmed very low mass binaries have $q > 0.9$ and the drop-off in the number of binaries is already visible at the highest mass ratios, it is unlikely that the observational biases described before affect this trend. The observational biases are, however, very likely to lead to underestimating the number of systems with low mass ratio.

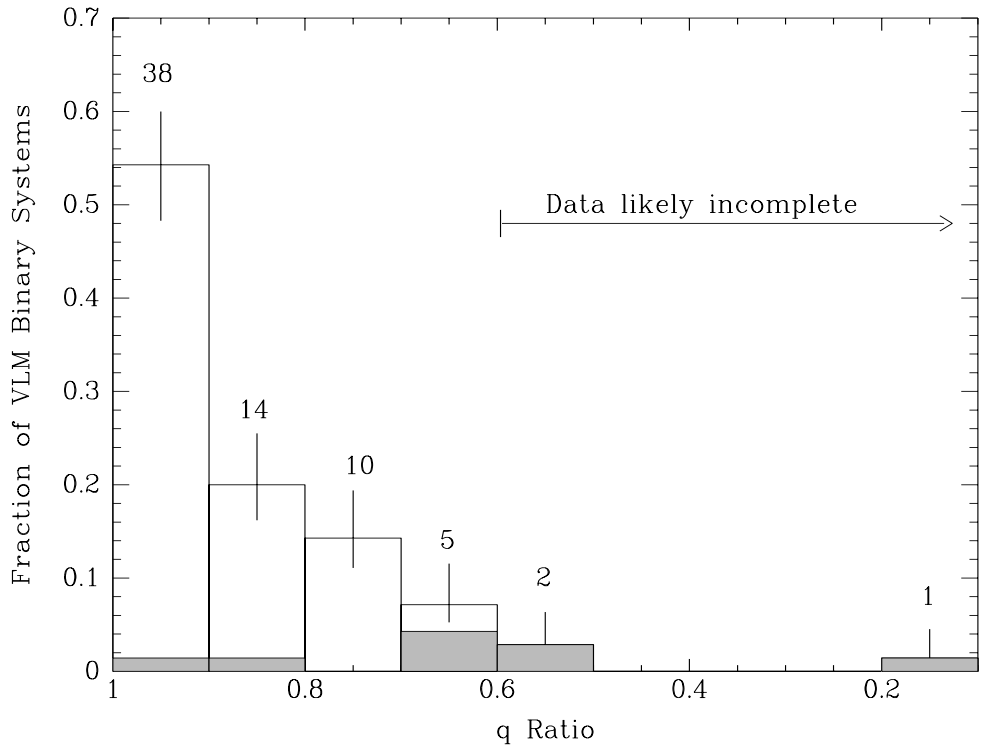

Figure 1.4: Mass ratio distribution of very low mass binaries (spectral type > M6) known to date (taken from Burgasser et al., 2007). The systems with age below 10 Myr are represented by shaded bins, with the number of binaries in each bin labelled.

Binary mass function

Mass as mentioned in the previous section is a very important parameter in determining the evolution of stellar objects, and the binary mass function helps constraining the components' mass in binary systems. The following two relations are used to work out the mass of the secondary object in a binary system:

$$f_1(M_2) = \frac{M_2^3 \sin^3 i}{(M_1 + M_2)^2} = \frac{P(v_1 \sin i)^3}{2\pi G} \tag{1.1}$$

$$f_2(M_1) = \frac{M_1^3 \sin^3 i}{(M_1 + M_2)^2} = \frac{P(v_2 \sin i)^3}{2\pi G} \tag{1.2}$$

For f_1 and f_2 being the mass functions for star 1 and star 2. These two relations are derived by equating the centripetal force and the gravitational force for both of the components. Note that this is done under the assumption of a circular orbit, and with the aid of Newtonian relations. The measurable quantities are P, which is the

orbital period (with the gravitational constant G), ($v_1 \sin i$) and ($v_2 \sin i$) which are the projected radial velocity amplitudes of the two components (where i is the orbital inclination of the binary). M_1 and M_2 are the masses of the two components.

With the two masses directly related to observable quantities by the mass function, the radial velocity amplitudes of both components can be measured, for example, from the double-lined spectroscopic binary spectrum. Both $M_1^3 \sin^3 i$ and $M_2^3 \sin^3 i$ can then be deduced using equations 1.1 and 1.2. However, the inclination is not a quantity that can be obtained easily for the majority of systems, but is necessary if one wants to determine the masses of both components. Thankfully, it is more feasible for certain types of binary systems such as visual binaries, and even more so for eclipsing binaries, where $i \simeq 90^o$. Note that the mass function can directly constrain the mass of the secondary if the mass of one of the objects is significantly smaller than the other (i.e. $M_1 \ll M_2$). The left-hand side of equation 1.1 in this case simplifies to $f_1(M_2) \simeq M_2 \sin^3 i$. This method is indeed one of the most robust ways to work out the masses of stellar objects. Further, the radii of both stars can be obtained from eclipsing binaries, and in fact these systems are the most common sources for which accurate radii and masses of stellar objects are obtained from. Moreover, if these binaries happen to have known distances too, then their luminosities can also be obtained.

Binary fraction/multiplicity

The binary fraction/multiplicity is one of the fundamental properties of binaries, offering clues to understand the formation mechanism. It provides extra constraints for testing the existing formation models. Unfortunately, the presence of unresolved binary/multiple systems induces an extra complication in obtaining, in particular for the substellar population, a precise luminosity function. Furthermore, observing faint and close binaries has proven to be a challenge, leading to a poorly constrained binary fraction for BDs and LMSs. A brief summary of the present knowledge of the stellar and substellar binary fraction is in the following paragraphs.

The percentage of solar-type stars in the main-sequence that have one or more companions is approximately 46% (Raghavan et al., 2010). The binary fraction has also been shown to be strongly dependent on the mass of the primary star, with more massive A-type stars having higher binary fraction, and lower mass M dwarfs and BDs having lower binary fractions. The results of various surveys are summarized by Ward-Duong et al. (2015) as shown in the left panel of Figure 1.5. Ward-Duong et al. (2015) combined the results of De Rosa et al. (2014) for A-type stars, of (Ragha-

van et al., 2010) for solar-type stars, their own results for M dwarfs, and the results of Allen (2007) for BDs, and demonstrated that the fraction of binaries (they only considered binaries, not multiple systems) clearly decreases as a function of mass from $\sim$33% to $\sim$7%. The right panel of Figure 1.5 shows the binary fraction as a function of separation for the M dwarfs in the sample of Ward-Duong et al. (2015). It is clear that the binary fraction decreases as a function of separation, with a much higher fraction at small separations, but it is also shown that M dwarf binaries have typically smaller separations than more massive binaries.

In addition, for spectroscopic binaries, their frequency is comparable to that of Population I stars (very old stars). This was deduced via a survey of thick-disk and halo stars (Torres, 1992). These results have been confirmed recently by combining Gaia eDR3 with LAMOST DR5 by Niu et al. (2021), who found a binary fraction of $42 \pm 1\%$ for G- and K-type stars, with a dependence on the age of the population, i.e. older populations have a higher binary fraction than the younger population. Specifically, Niu et al. (2021) found that the binary fraction for G and K stars in the thin disk is $39 \pm 2\%$ while thick disk stars have a binary fraction of $49 \pm 2\%$. Niu et al. (2021) also found that for both the thin- and thick-disk stars, the binary fractions decrease toward higher [Fe/H], but with different correlations for the thin and thick disk. They conclude that this is likely related to the different formation histories of the thin and thick disk. The thin disk is the inner part of the Milky Way disk, and has a scale height of only $\sim$300pc (Vieira et al., 2023). It is where most of the stars, gas and dust is located, and is also where star formation is still currently taking place (Allende Prieto, 2010). As a result, stars in the thin disk are on average younger and more metal-rich than the rest of the Galaxy (Allende Prieto, 2010). The thick disk is the outer part of the disk of the Galaxy, and has a scale height of $\sim$800pc (Vieira et al., 2023). It is less dense than the thin disk and has little gas and dust, and there is basically no star formation (Vieira et al., 2023). Stars in the thick disk are on average older (10–12 Gyr) and more metal poor than the thin disk (Kordopatis et al., 2011). Finally, the halo is roughly a sphere and extends for several kpc around the centre of the Galaxy. It has very low density and contains the oldest and most metal-poor stars (e.g. Prantzos, 2008).

For pre-Main Sequence (PMS) stars and young stars in general (i.e. younger than 10^5 yrs) the results are less clear. However, in those separation ranges where PMS binaries can be observed, the multiplicity frequency appears to be higher than for Main Sequence stars in the same separation ranges. Patience et al. (2002) suggests that for

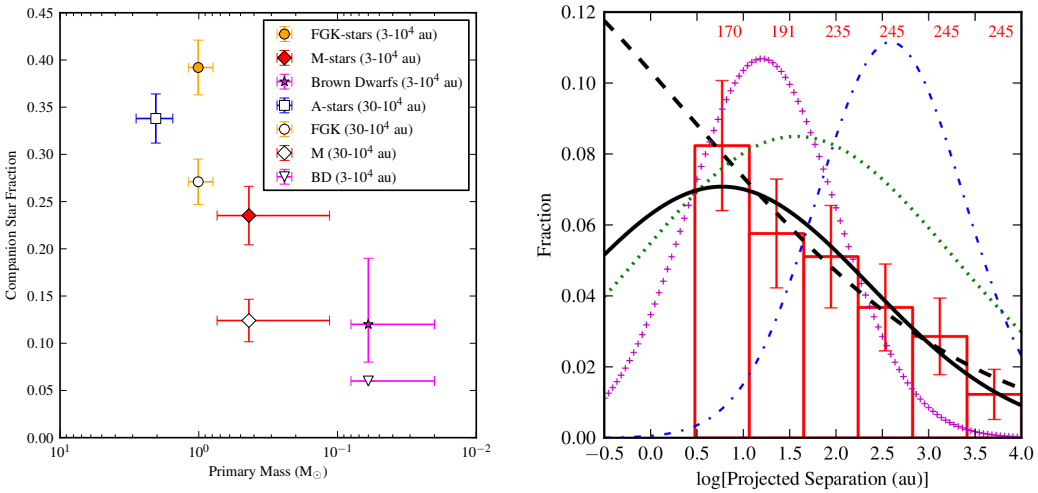

Figure 1.5: *Left:* The binary fraction measured within 30–10,000 AU (empty symbols) and within the 3–10,000 AU (full symbols) by various surveys, as a function of primary star mass (see Section 1.2.1 for references). *Right:* The binary separation distribution of the M dwarfs from the survey of Ward-Duong et al. (2015) within the separation range of 3–10,000 AU, corrected for incompleteness (red histogram). Assuming a log-normal distribution, a Gaussian was fit to the observed distribution (dashed black curve). A restricted fit was also computed by fixing the mean of the distribution to the centre of the first bin of the distribution (solid black curve). For comparison, the distribution of companion separations for A-star primaries (blue dot–dashed curve), solar-type primaries (green dotted curve), and for M-dwarf primaries in a previous lucky-imaging survey (magenta crosses). (Figure 2 from Ward-Duong et al., 2015).

PMS primaries in the mass range $0.5\ M_{\odot} < M_1 < 5\ M_{\odot}$ the multiplicity frequency is in the range $83 - 100\%$. In general, the fact that binary stars are spotted among PMS, is an indication that most binaries are formed during the collapse of the proto-star, or in the stellar formation period. Moreover, Elliott & Bayo (2016) studied the multiplicity fraction and separation distribution of companions in the β-Pictoris moving group and compared it to previous multiplicity studies in younger and older regions. They showed that the dynamic evolution of triple systems leads to the formation of wide binaries, and that the lower fraction of wide binaries in the field population compared to the younger population is a result of dynamical evolution, i.e. it is the result of the disintegration of wide binaries with time.

When it comes to LMSs and BDs, multiplicity studies have been conducted via the combination of high-resolution spectroscopy surveys (e.g. Basri & Reiners, 2006; Joergens, 2006, 2008), with peak sensitivity to tightly bound systems, and high-resolution

imaging (e.g. Ahmic et al., 2007; Delorme et al., 2012) which have a higher sensitivity at the typical distances of observed BDs ($\gtrsim 2-3$ AU). Although biased towards typical BD separations, the binary fraction that was suggested by the magnitude-limited high-resolution surveys is 7–15% (9^{+11}_{-4}%, Burgasser et al. 2003a; $7.6^{+5.9}_{-1.7}$%, Bouy et al. 2003; $13-15$%, Martín et al. 2000). On the other hand, using high-resolution spectroscopy for a sample of late-M dwarfs, an estimation of 6^{+7}_{-2}% was made by Reid et al. (2002). Then, from a sample of 25 late-M and early-L dwarfs, Guenther & Wuchterl (2003) have estimated the binary fraction to be 12^{+10}_{-4}%. Another estimation was derived by Joergens (2008) by monitoring the radial velocity of LMSs and BDs in Chamaeleon I. At separations < 3 AU the multiplicity fraction is 10^{+18}_{-8}% and 7^{+5}_{-3}% at separations $\leq$ 0.3 AU. Joergens (2008) claims that where the separations are < 1 AU, then there will be a decline in the binary fraction. This claim is supported by the results of Maxted et al. (2008) where at separations < 0.28 AU, the binary fraction in σ and λ Orionis is found to be < 7.5%. The previous results are in disagreement with Kurosawa et al. (2006), who found that at separations < 0.1 AU, the binary fraction in Upper Scorpius is 24^{+16}_{-13}%. In addition, Maxted & Jeffries (2005) derived a much higher ratio of tight binaries, after taking into account every likely source of biases and incompleteness in the surveys that were available at the time. They concluded that at separation < 2.6 AU, the binary fraction for VLMSs and BDs is $17-30$%. Assuming at separation $>$ 2.6 AU the binary fraction is 15%, then the total binary fraction would be $32-45$%. This supports the binary fraction in the Praesepe and Pleiades clusters of 50^{+11}_{-10}% that was derived by Pinfield et al. (2003). Wide very low mass binaries seem to be rare in contrast with tightly bound very low mass binaries. There appears to be a decline in binary fraction with separation, from an upper limit of 8% in α Perseus at separation > 11 AU (Martín et al., 2003) to another upper limit of 5% in IC 348 at separation > 15 AU (Luhman et al., 2005), down to an upper limit of 2% in Trapezium at separation $>$ 150 AU (Lucas et al., 2005). Note that it is the high-resolution imaging that could bias these results (causing some of the very wide systems to be excluded) due to a typical field of view of $10-20$ arcseconds (i.e. systems at 30 pc with separation $\gtrsim 150$ AU or systems in young nearby clusters with an even larger separation $\gtrsim 200-1000$ AU could be missed).

1.2.2 Formation of multiple systems

All of the binary properties that have been discussed above (from observational data and detailed numerical simulations), play an extremely important role in assisting to answer the long-standing question: what is/are the dominant formation mechanism/s for stars, BDs and planetary-mass objects (i.e. objects with mass less than the deuterium burning limit at 13 $M_{\rm Jup}$)?

Extremely young binary systems have been identified (Wootten, 1989; Sasselov & Rucinski, 1990) yet there have not been any direct observation during the formation of a binary system so far. Up-to-date observational studies show that it is likely for most binaries/multiple systems to be formed during the proto-stellar collapse, i.e. the very early stage of formation of a stellar object, which can be divided into two phases. The first is the isothermal phase, when the object is optically thin. Optically thin means that the photons can escape the gas easily, or in other words the likelihood of a photon to be absorbed is low. The second phase is the adiabatic phase, when the object is optically thick, meaning that the photons cannot escape the gas easily, or in other words the likelihood of a photon to be absorbed is high. Though various ideas have been suggested to try to explain the origin of binary systems, it is fundamental to be able to explain the observed properties of multiple systems in order to determine their dominant formation mechanism.

Although the fully explained physics was missing, Laplace in 1796 was the first person who proposed a formation mechanism for binary systems (see Tassoul, 1978). His theory was that separate stellar nuclei form during star formation and somehow come into orbiting each other later. It could be assumed that it is via fragmentation that the separate nuclei form (Bodenheimer, 1992). Then in 1876, Stoney came up with the idea of capture (see Aitken, 1935). This might happen when two independently formed unbound stars are slowed down by losing some of their initial angular momentum (i.e. via a dissipative process), and then end up sharing a common orbit (e.g. WD0837+185AB, Casewell et al., 2012). Another possible formation scenario for binary systems that was put forward by Kelvin and Tait in 1883 (see Tassoul, 1978) and had the full support of Jeans (1929) is fission. This mechanism might occur while the hydrostatic equilibrium applies, when an object undergoing a rapid rotation might become dynamically unstable and break up into fragments. In 1953, Hoyle suggested an idea that is based on the principle of increasing density of the isothermal collapsing cloud, extending the originally large-scale-dependent dynamical instability,

to continuously being unstable even when the cloud is reduced in size. This increases the chances for the cloud to fragment as the time frame of given ideal conditions extends. Rotation is an additional fundamental cause, discovered in later studies, that allows the spreading out of individual fragments after they form, hence stopping the overall collapse of the cloud, as it is not just one large cloud anymore but fragments (though the fragments will continue to collapse separately). In other words, during the hydro-dynamical collapse phase, the process of a rotating proto-star being broken up into fragments is known as fragmentation. Hierarchical fragmentation can be either triggered by rotation (Bodenheimer, 1978) or by cloud-cloud collisions (Pringle, 1989). However, the results of Lattanzio & Henriksen (1988) numerical simulations of isothermal cloud-cloud collisions show no binaries formed in their parameter range.

In addition, close binaries can be the consequence of wide binaries evolution (Pringle, 1989). Wide binaries in general are in highly elliptical orbits, and when the binary systems are young, they are likely to have a disc around them. When these discs undergo hydrodynamic interaction at the periastron, the system could lose angular momentum via the friction between the interacting discs, then the original wide orbit could get closer with each disk interaction. When the discs eventually disappear, the system might have lost enough original separation to become a close binary. "Normal" fragmentation, on the other hand, is to allow the clouds to evolve further (i.e. first undergo gravitational collapse after dense cores have been developed) before the spontaneous fragmentation takes place. Under ideal conditions, the disc that forms around young stars can become gravitationally unstable, hence leading to possible fragmentation, according to Adams et al. (1989). A brief discussion of the four types of formation scenarios that are thought to form binary/multiple systems (fragmentation, disk fragmentation, fission and capture) is in the following sub-sections.

Fragmentation

During the isothermal phase, the adiabatic collapse of rotating proto-stars is modelled by theorists, and the outcome suggests a very high likelihood of these proto-stars to fragment into multiple systems due to instability (e.g. Burkert & Bodenheimer, 1996; Guszejnov & Hopkins, 2015; Guszejnov et al., 2017). Adiabatic collapse means that during the collapse the proto-star does not exchange heat with the surrounding gas. Systems produced via this process are likely to end up with periods that exceed a few hundred years. Hence, this scenario is challenged by the existence of close binaries, because it is known to be very unlikely for the fragmentation to take place while the

gas is experiencing high pressure (optically thick and high density), which is the case in the later phase of star formation, when the original cloud has become a lot smaller.

In the early stage of star formation, the initial cloud can mainly fragment to form wide binaries as the density of the cloud is low and still large in size. Though, it is not impossible for a few of the multiple systems formed by fragmentation to be in relatively shorter periods either. According to Boss (1986), systems with orbital separations up to approximately 1 AU can be formed by fragmentation, if they form in the central regions of the collapsing cloud while in the adiabatic phase. Beside this formation mechanism, there are also other formation theories that cannot explain close binaries, such as tidal capture, fission of rapidly rotating stars and three-body capture. Other formation scenarios including hierarchical fragmentation, orbital interactions and disk-induced captures in fragmented multiple systems, orbital decay of long-period systems and gravitational instabilities in disks are under investigation at this time. On the contrary, if the collapsing cloud has low angular momentum, and that low angular momentum is removed after disk formation, or the escape from multiple systems, it could be one of the routes for single star formation.

Some of the more important numerical calculations regarding hierarchical fragmentation were done by Boss (1991) and Hacar et al. (2013). In general, the theory of hierarchical fragmentation is that a ring structure would form at a point when the rotational effects come to be significant during the collapse of the formation cloud. Then the fragmentation begins with having the ring first fragment into two parts, then a bit further on the time line, each fragment again splits into two. Though, to be considered a true hierarchical fragmentation, the first fragments of the ring will have to undergo the exact same path as the original collapse cloud (collapsing to the point that rotational effects become essential so that a ring structure is formed), e.g. similar to cellular splitting activity. Moreover, the sub-fragmentation can only occur when each fragment reaches the angular momentum of the original cloud. This requires a further substantial collapse in order for them to regain the 90 to 95% of angular momentum lost after the first fragmentation takes place. This fundamental information regarding the collapse, however, was not included in the calculations of Boss (1991). Since the resulting sub-fragments do not appear to be sharing an orbit, and also have a sub-orbit which is too small to be viewed on the numerical grid used, this calculation does not represent true hierarchical fragmentation.

Disk fragmentation

A disk like structure will form if a proto-star with a relatively slow initial angular momentum collapses through the adiabatic phase without fragmenting. Gravitational instabilities can cause possible fragmentation in Keplerian disks in equilibrium around a central star (Adams et al., 1989; Shu et al., 1990). Though the conditions have not yet been recognised, the formation of a binary system could be possible as a consequence of such instability.

Fission

In general, a uniform-density star can gain angular momentum either when it is contracting during the proto-stellar collapse (early phase of star formation) or contracting during disk accretion (later phase of star formation). The growth rate of the rotational energy surpasses the growth rate of the gravitational energy, and when the rotational energy eventually exceeds the gravitational energy, the star then becomes unstable and breaks up into smaller fragments.

Fission yields mostly close binaries due to the limited amount of spin that a star can carry. However, Tassoul (1978) pointed out a few major issues that this formation scenario could encounter, such as the slow rotation observed in T Tauri stars (TTS, variable pre-main sequence stars). Dynamical instability, therefore, is unlikely to take place due to insufficient angular momentum. Hence, fission seems to be favourable only during core accretion. Another problematic issue to this formation theory is that the binary ratio of the resulting systems is not consistent with observations. The star may also never reach the point where it will become unstable (required initial condition), and this is the third major problem with this formation mechanism.

For proto-stellar objects to form very tight binaries, their angular momentum has to be very small, which then results in the majority of their own mass collapsing onto the central core rather than onto the surrounding disk. According to Ruzmaikina (1981a,b), the core may not be prone to become unstable (when the rotational energy becomes larger than the gravitational energy) as the effects of convection or magnetism are likely to transport a substantial amount of angular momentum within the core out into the disk and lead to the formation of a single star. However, even if the proto-stars manage to reach the point where the rotational energy becomes greater than the gravitational energy, according to the 3-dimensional numerical hydrodynamical calculations of Durisen et al. (1986), the angular momentum can be transferred out

from the central core by spiral waves, preventing the instability from happening. For more information, see Bodenheimer (1992).

Capture

The last formation mechanism is capture, i.e. when two stars that formed independently are captured into an orbit. It may occur in one of the following three situations. The first one is when the excess of energy is removed by the presence of a third body, i.e. when three individual stars are close by initially, then, due to dynamical interactions between them one of the bodies is "ejected", removing some of the excess energy, and the two remaining objects then form a binary. The second situation is when two single stellar objects pass by each other very closely by chance, and friction is caused by the tidal dissipation between them, slowing them down sufficiently so that dynamical interactions can take place and form a system. The last situation is when, under the presence of a dissipative medium (i.e. residual gas in a young cluster), as the young stars are still close to each other before being separated by their increasing radial velocity, the presence of residual gas could impose friction between them and they could randomly pair up as an outcome.

The first two situations are not supported by observations, as the slow capture rates expected in young dense clusters or in the galactic disk are not able to explain the observed binary frequency (e.g. Hills, 1976; Hills & Day, 1976; Boss, 1988). On the other hand, the third situation is more favourable where the young stellar objects are in the presence of the residual gas that is around them in the form of circumstellar disks. The capture rate that is induced by disks in high stellar density environments (e.g. the Orion Trapezium cluster) is 0.4 captures per star per 10^6 yr (Larson, 1990). Though another factor that could affect this process was pointed out by Clarke & Pringle (1991a). Depending on the velocity of the encounter, disks around stars may be removed by high-velocity encounters, whereas capture is much more likely to occur during low-velocity encounters. The capture rate according to Clarke & Pringle (1991a) is 0.04 captures per star per 10^6 yr, an order of magnitude lower than (Larson, 1990). The capture rate is, however, $\approx 0.05 - 0.1$ captures per star per 10^6 yr according to the results of numerical calculations by Heller (1991), which sits between the Larson (1990) and Clarke & Pringle (1991a) results.

The separation between the components depends on the type of capture. Systems produced by the three-body capture are often far apart, and close binaries are often produced by the two-body tidal capture, while the separations between the paired

up stellar objects produced by the disk capture are comparable to the outer radius of the disk. The various sizes of orbits produced by these three types of capture cannot explain the smooth period distribution observed. However, some other observations can be explained by the predictions of the capture theory, such as a wide range of mass ratios (no relation in mass between the two components) and eccentricities. In addition, the components are non-coeval (differences in age observed so far are up to 10^6 yr) and the spin of the angular momentum of one of the components can be unaligned with the orbit, as observed in some systems. Normally, the probability for this mechanism to take place is relatively low, but in different circumstances capture can have a slightly larger effect (i.e. fragmentation of a collapsed molecular cloud core, see Miyama et al. 1984; Monaghan & Lattanzio 1984). For example, in a very high stellar-density environment (i.e. more so than the Orion Trapezium cluster) the typical separation between fragments is small (i.e. $\sim$0.01 parsec). Gravitational interactions therefore take place between the fragments, and single stars and binaries may be produced by the three-body capture process, also by the disk-induced and tidal capture (the latter in close orbits). This type of systems was studied with the aid of N-body simulations of multiple systems (see e.g. Anosova, 1989). Furthermore, for the three-body "systems" with disk dissipation (co-orbiting initially and highly unstable), numerical studies were made by Clarke & Pringle (1991b). Their results show high sensitivity to changes in the initial conditions, and also a possible wide range of eccentricities and orbital parameters.

1.2.3 BDs in multiple systems

The first L and T dwarfs, GD 165B and GL 229B respectively, were both discovered accompanying a more massive primary (i.e. white dwarf-L dwarf and M dwarf-T dwarfs; Becklin & Zuckerman 1988; Nakajima et al. 1995). In order to increase the number of identified nearby bright stellar objects that couple to BDs, various methods have been used and a lot of interesting new multiple systems hence have been discovered. With facilities such as the Hubble Space Telescope (HST), the Very Large Telescope (VLT), and the Keck Telescopes, all providing high-resolution optical and IR imaging, one of the methods is to look for low-mass companions to M dwarfs, either in the field (Reid & Gizis, 1997) or in open clusters (e.g. Martín et al., 2000; Patience et al., 2002). In fact, Teide 1, which together with GL 229B holds the title of first BD discovered, was found in the Pleiades (Rebolo et al., 1995). Alternatively, much wider

high-mass + low-mass systems can be identified by cross-matching a good selection of ultra-cool dwarfs (hereafter UCDs) with a list of higher mass stars and WDs, to establish binarity via common PM. The search for UCDs as companions to nearby stars hence becomes more conceivable now with the availability of near-infrared (NIR) all-sky surveys and of the Gaia catalogue.

The mass of BDs is fundamental in obtaining insights on the properties of these objects. However, the substellar nature of these UCDs prevents the use of the luminosity-mass relation to determine their mass. The age of these ultra-cool objects is also impossible to determine if they are isolated. This is where benchmark systems become extremely useful, especially in the study of the nature, formation and evolution of UCDs. This sort of system in general consists of main-sequence star/s and UCD/s, and note that the preferable benchmark systems are those with wide separation (i.e. > 100 AU). This is because if the faint UCD is too close to the parent star then the glare of the primary will make it difficult to observe the BDs and GESPs. In addition, the nature and the properties of the BD could also be altered by the exchange in mass within the system (e.g. when the star evolves and becomes a red giant) if the components are too close. These cannot be considered benchmark systems anymore.

Young benchmark UCDs (≤ 1 Gyr) can be found as members of moving groups and clusters (e.g. Casewell et al., 2007; Lodieu et al., 2011; Gagné et al., 2014, 2015, 2023). Besides sharing kinematic properties, the UCDs have a known metallicity and a decent constrained age as part of the cluster. Note that the formation and properties of these very young substellar objects can be derived and studied within those nursery environments, such as the Orion nebula cluster. In addition, given that these benchmark systems are very young (~ 1 Myr), hence they are much brighter, and so they can be observed out to much greater distance than that of field UCDs. Unfortunately, for field UCDs, the age, metallicity, and other physical properties are a challenge to obtain, one of the major complications being the mass-age degeneracy (i.e. the fact that they significantly fade and cool over time).

UCDs as members of binary systems, however, provide the best source of benchmark companions (e.g. Pinfield et al., 2006). This is because the stellar primaries can be characterised well, and given they were formed from the same molecular cloud, it is quite safe to assume both objects have identical age and composition (i.e. metallicity). Note that several methods can be used to calculate the age of the main-sequence primary. Such methods include comparison to theoretical models with their location on the HR diagram, age-metallicity relations, kinematical or rotational velocity age,

Lithium test, and coronal or chromospheric activity (Ca II H&K, Hα, X-ray). Note that for eclipsing benchmark systems, their mass (from Kepler's law) and radius (from the light curve) can be calculated from the dynamical interaction of the system. However, depending on the type of primary stellar object, a precise measurement of the age could be a challenge (e.g. variable stars).

The later phases of stellar evolution show age calibrators that are more reliable than the main-sequence phase, where the uncertainty on the age can be large. For example, the subgiant stage is relatively well constrained, and also very short in comparison to the lifetime on the main sequence. Furthermore, there are also benchmark systems that consist of a UCD companion to a white dwarf (e.g. Luhman et al., 2011; Casewell et al., 2012; French et al., 2023). Such systems include DA WDs-L dwarf (e.g. Becklin & Zuckerman, 1988; Steele et al., 2009), DA WD-mid-T dwarf (Casewell et al., 2012; Day-Jones et al., 2011) and DQ WD-Y dwarf (Luhman et al., 2011). The cooling age of the WD can be measured with precision as the WD stage is well understood (e.g. Fontaine et al., 2001). By studying the spectral energy distribution, a decent estimation of the effective temperature (hereafter $T_{\rm eff}$) can be obtained. Then, by fitting the hydrogen lines, which are strong and can be easily observed and measured in WD spectra, with an appropriate atmospheric model, the surface gravity (log g) of a WD can be obtained. If the distance hence the luminosity is known, one can then compute the radius and therefore one can readily calculate the mass of the WD. Once the mass and temperature of a WD is known, the cooling time, i.e. the time taken by the WD to cool down to the current temperature, can be estimated using cooling models (e.g. Bergeron et al., 2011; Tremblay et al., 2011; Bédard et al., 2020). Applying the relation between the WD and the progenitor, the mass of the progenitor can then be obtained (this is known as the initial-final mass relationship; Cummings et al., 2018). Using evolutionary models for main-sequence stars to get the total time that took the progenitor from being born to first becoming a WD (e.g. Choi et al., 2016), combining it with the cooling age that was previously acquired, one can determine the age of the WD.

In general, these wide benchmark systems also provide extra constraints to test important models and theories, e.g. evolutionary models (Mohanty et al., 2004a,b; Dupuy et al., 2010) and atmospheric models (Leggett et al., 2008; Burningham et al., 2009; Pinfield et al., 2012).

Population properties of BDs

It is relatively common for wide main-sequence binaries to have separation >1000 AU. Gizis et al. (2001b) first estimated an L dwarf companion fraction of 1.5%, although from a sample consisting of only three wide L dwarf companions to main-sequence stars. A total UCDs companion fraction of $18 \pm 14\%$ was also then calculated by assuming $\alpha = 1$ into the companion mass function (Chabrier, 2005). Using a larger sample consisting of 14 wide common-proper-motion companions down to a limiting magnitude of $J = 16.1$ mag to stars from the HIPPARCOS catalogue, Pinfield et al. (2006) deduced a larger L dwarf companion fraction of $2.7^{+0.7}_{-0.5}\%$ and a larger UCD companion fraction of $34^{+9}_{-6}\%$ (under the same assumptions as Gizis et al. 2001b). This result implies that a sufficient number of wide companion UCDs to main-sequence stellar objects are available for studying.

A mass-age plot of benchmark UCDs is shown in Figure 1.6 (taken from Figure 6.3 of Day-Jones 2009; see also Deacon et al. 2014 and dal Ponte et al. 2020). The distance-magnitude limit can clearly be observed, corresponding coarsely to a detection limit of $J \sim 19$ mag. This is represented by the black dotted line, corresponding to a distance limit of 50 pc, reflecting the sensitivity of the surveys used to discover these UCDs. Being extremely faint, the expectation of detecting old, very low-mass UCDs using these surveys is very low. More, due to the fact that for young UCDs there are more age indicators (e.g. activity, rotation, and Lithium detection), hence their age can be more easily constrained. So in comparison there are many more young benchmark UCDs than old benchmark UCDs. Note that most of the benchmarks in the younger region have known metallicity as they are members of moving groups or clusters. In addition, the figure also shows that the number of benchmark UCDs decreases beyond the age of 2 Gyr.

The importance of benchmark UCDs is shown further in Figure 1.7, taken from Figure 10 in Burningham et al. (2013). The two plots show a comparison between the observed colours of a number of benchmarks and the model grid from Saumon et al. (2012) in the top part of the plot and the model grid from Morley et al. (2012) in the bottom part of the plot. Each benchmark is linked to a box indicating the colour predicted by the models. It can be seen that the model predictions are wrong by almost 0.5 magnitudes in many cases, showing that the models need improvements.

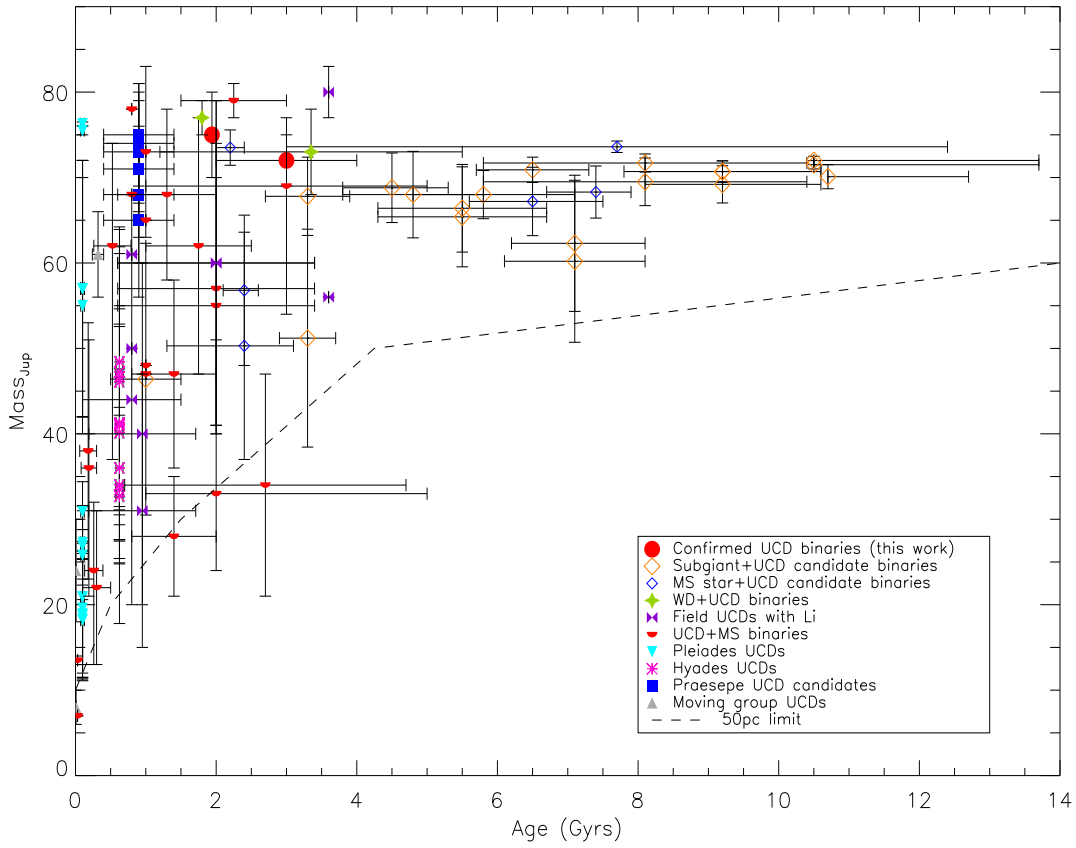

Figure 1.6: A mass-age plot showing the distributions of the benchmark systems from the literature, taken from Figure 6.3 of Day-Jones (2009)

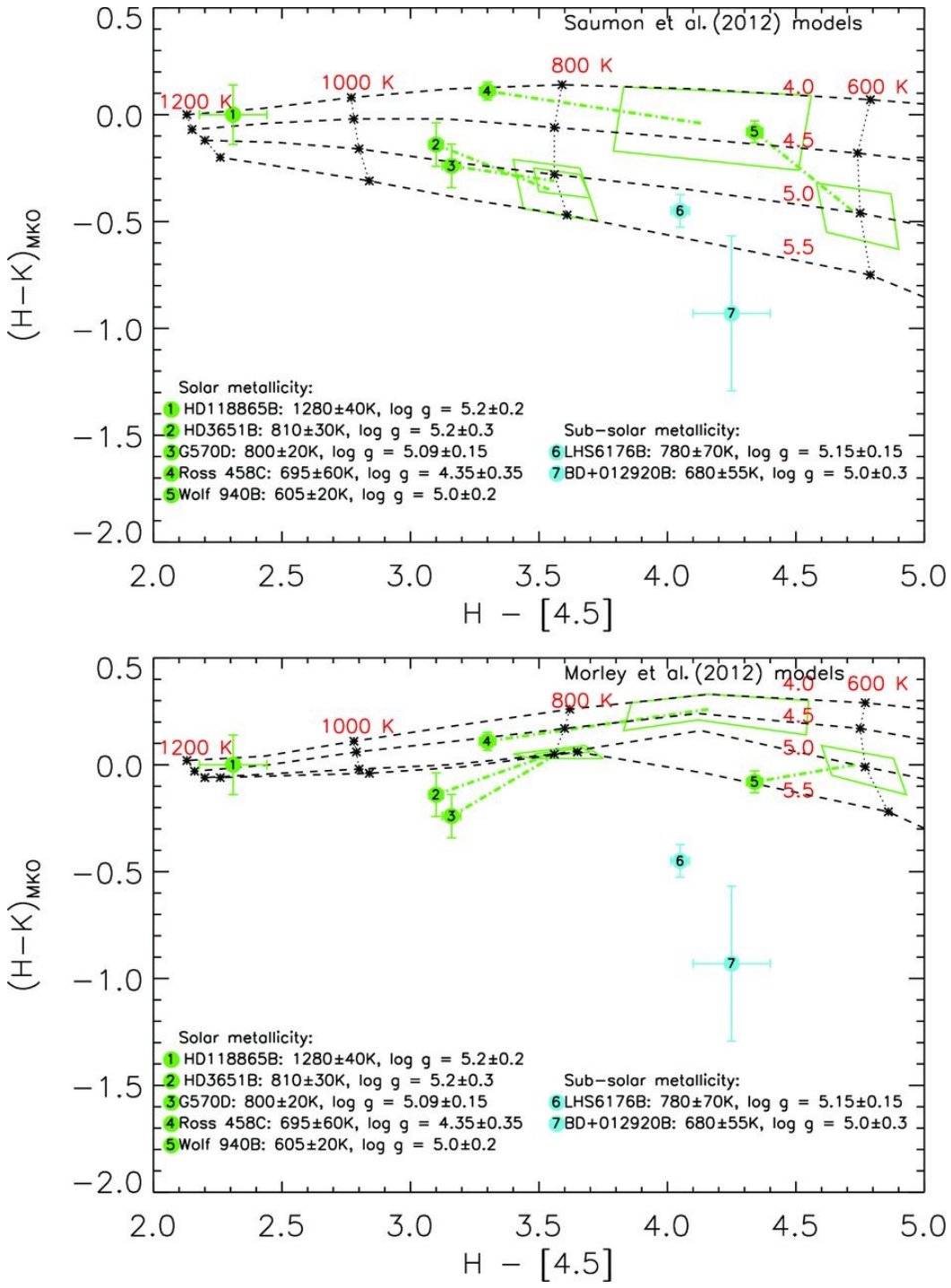

Figure 1.7: Colour-colour plots of the benchmark systems from the literature. Model colour tracks for Saumon et al. (2012, top panel) and Morley et al. (2012, bottom panel) are shown for comparison. Each benchmark is linked to a box indicating the colour predicted by the model. Taken from Figure 10 from Burningham et al. (2013).

1.3 Disintegrating systems

In a particular case, when a binary system is interacting with a close by object, or with another binary/multiple system, over time the binding energy within the components of the binary is gradually reduced, causing the system to eventually become unbound. Note that binaries that have a large cross-section (i.e. wide binaries) are more likely to interact with other stellar or substellar objects. Normally, such interactions are relatively weak, but there are some more severe interactions that can lead to a more violent break-up of the systems.

Disintegrating systems are thought to be common (Li et al., 2009), but the average time for disintegration is short, approximately 1 Myr (Szebehely, 1972). Therefore, disintegrating systems are very difficult to identify. To search for disintegrating multiple systems, I will first have to look for binary/multiple systems whose components have a wide separation between each other. This is because widely separated systems will naturally have a greater possibility of disintegrating in comparison to much tighter systems. In principle, a system with weaker bonds within the components is easier to be disrupted by chance dynamical interactions than systems with stronger bonds. In theory, this could be the cause of some of the disintegrating multiple systems seen in the HIPPARCOS Main Catalogue (Li et al., 2009). I will be looking into binary/higher order systems and use their PM and metallicity to see if they are disintegrating systems, and if so I will try to reconstruct the interaction leading to the disintegration. Then I will look for their low-mass ejected components.

1.3.1 Dynamical interaction of multiple systems

In general, celestial objects interact with each other gravitationally (for basic interaction physics, see e.g. Fregeau et al. 2004; Malmberg et al. 2007 for interactions in clusters; and for interactions in disks, see e.g. Moeckel & Veras 2012). Discussing in detail the properties and evolution of the numerous types of interacting binary systems is beyond the scope of this thesis. In the following sections I will therefore focus on the disintegrating systems, since these are the target of my work.

1.3.2 Disintegration as a result of galactic tides

Galactic tides (Jeans, 1919; Lindblad, 1925) play an important role in the evolution of wide binaries (e.g. Weinberg et al., 1987), planets in wide orbits (e.g. Veras et al., 2009),

and even the evolution of the Oort cloud (e.g. Heisler & Tremaine, 1986; Fouchard et al., 2006).

Antonov & Latyshev (1972) determined the zero-velocity surface for the motion of a particle with respect to the Sun. That is the surface inside of which a particle which has zero velocity relative to the Sun is stable against tidal disruption (i.e. it won't be ejected as a result of galactic tides), while if it is outside this surface it will be unstable (i.e. it will be ejected). The tidal radius a_T is the corresponding maximum distance from the central star. This radius depends on the local density (usually measured in $M_\odot$ pc^{-3}), the mass of the central star, and the velocity of the star around the Galaxy (Antonov & Latyshev, 1972). Using the parameters given by Antonov & Latyshev (1972), Weinberg et al. (1987) calculated a_T = 0.93 pc for a binary of total mass M = 1 $M_\odot$ at the Sun's position in the Galaxy. Repeating the calculation for modern values of the Oort constants, they found a_T = 0.63 pc. By comparison, Heisler & Tremaine (1986) found a_T = 0.98 pc, using different Galactic parameters, showing that the exact number is uncertain.

For a planet in a wide orbit around a star, Veras et al. (2009) found that the maximum semi-major axis for a stable orbit is given by the equation:

$$a_T \simeq 1.7 \times 10^5 \text{ AU} \left(\frac{M_*}{M_\odot}\right)^{\frac{1}{3}} \left(\frac{\rho}{0.1\ M_\odot\ pc^{-3}}\right)^{-\frac{1}{3}} \tag{1.3}$$

where M_* is the mass of the host star and ρ is the local galactic mass density. Planets with a semi-major axis greater than a_T will be ejected within one orbit around the Galaxy. This equation only applies to planetary mass companions.

1.3.3 Disintegration as a result of close encounters

While Galactic tides lead to gentle breakup of wide multiple systems and wide planetary systems, close encounters between a wide multiple system or a wide planetary system and an external object (a star, or another multiple system, or a giant molecular cloud) can lead to more catastrophic and more violent break-ups.

Weinberg et al. (1987) developed a theory of close encounters which is based on the concept that close encounters can be treated as "impulses", i.e. they assume that the result of a close encounter can be described simply by determining the increase of orbital energy for each component of the binary. Let us now call a the semi-major axis of the binary, and call b_1 and b_2 the impact parameters of the encounter, which are the perpendicular distances between the path of the incoming external star (also called

"perturber") and each component of the binary. Weinberg et al. (1987) divided close encounters into two extreme cases. Case 1 is when the perturber passes very close to one component and very far from the other, e.g. when $b_1 \ll a$ and $b_2 \approx a$. This case is called by Weinberg et al. (1987) the "single kick limit" because the energy gained is all gained by star 1, i.e. $\Delta E_2 \sim 0$. In this case, Weinberg et al. (1987) determined that the change in orbital energy is:

$$\Delta E = 2 \left(\frac{G\, M_p}{b\, V_{\rm rel}} \right)^2 \tag{1.4}$$

where G is the gravitational constant, M_p is the mass of the perturber, b is the impact parameter, and $V_{\rm rel}$ is the relative velocity between the perturber and the binary. Case 2 is when the perturber passes almost exactly at the same distance from the two components of the binary, i.e. $b_1 \approx b_2$ and the impact parameter is much greater than the semi-major axis of the binary, i.e. $b \gg a$. The energy change in this case is almost equally split between the two components of the binary, i.e. $\Delta E_1 \approx \Delta E_2$. This case is called the "tidal limit", because in this case the effect of the encounter is similar to the effect of the Galactic tides. Weinberg et al. (1987) determined that the change in orbital energy is:

$$\Delta E = \frac{7}{3} \left(\frac{G\, M_p}{b\, V_{\rm rel}} \right)^2 \left(\frac{a}{b} \right)^2 \tag{1.5}$$

In both equations, ΔE is an approximation, because the actual energy change depends on the exact direction from which the perturber is coming from, the eccentricity of the orbit of the binary, and the orbital phase in which the binary is when the close encounter happens.

If ΔE for a close encounter is greater than the binding energy of the binary, i.e. $\Delta E > -GM/2a$, the binary will disintegrate.

Using the above equations, Weinberg et al. (1987) then developed a Montecarlo simulation to determine the time it would take a binary to be disintegrated as a result of repeated close encounters with other stars as well as giant molecular clouds in the Galactic disk. They found that the time for a binary to be disintegrated can be calculated as follows:

$$t \sim 3.6 \times 10^5 \left(\frac{n_*}{0.05\ {\rm pc}^{-3}} \right)^{-1} \left(\frac{M_{\rm tot}}{M_\odot} \right) \left(\frac{M_*}{M_\odot} \right)^{-2} \left(\frac{V_{\rm rel}}{20\ {\rm kms}^{-1}} \right) \left(\frac{a_0}{\rm AU} \right)^{-1} {\rm Gyr} \tag{1.6}$$

where t is the time in which the binary is expected to be disintegrated, n_* is the average stellar density of the Galactic disk, $M_{\rm tot}$ is the total mass of the binary, M_* is the typical

mass of the perturbers, $V_{\rm rel}$ is the typical relative velocity of the perturbers, and a_0 is the initial semi-major axis of the binary. Given the typical values known at the time, Weinberg et al. (1987) concluded that binaries with $a_0 \sim 0.1$ pc should disintegrate within 10 Gyr, i.e. within the age of the Milky Way. So they conclude that there should be very few binaries with $a > 0.1$ pc.

Using the equations above and with more recent estimates for the parameters of the Galactic disk, Close et al. (2007) found that the maximum separation ($a_{\rm max}$) for a binary to be able to survive for the age of the Milky Way is $a_{\rm max} \sim 33,000\,(M_{\rm tot}/M_\odot)$ AU, so for a binary made of two solar-mass stars the maximum separation is ∼66,000 AU, i.e. ∼0.3 pc.

Veras et al. (2009) also using the equations by Weinberg et al. (1987) found that the maximum distance from the parent star at which a planet is likely to survive is:

$$a_{ps} \simeq 10^5 \text{ AU} \left(\frac{\text{Gyr}}{t_*}\right) \left(\frac{M_*}{M_\odot}\right) \left(\frac{0.15\ M_\odot\ \text{pc}^{-3}}{\rho}\right) \tag{1.7}$$

where t_* is the age of the system, M_* is the mass of the host star, and ρ is the density of the Galactic disk. In other words, there should be no planetary systems with planets in an orbit larger than a_{ps}.

1.3.4 The Marchal's test

The field of disintegrating triple/multiple systems has not been widely explored. However, Marchal in 1990 developed an analytical test to look for escaped objects from a general N-body system (Marchal, 1990). Later, Li et al. (2009) adapted the Marchal's test to real triple stars.

For triple systems, there are several analytical tests of escape (see Georgakarakos, 2008, and references therein). The common idea for all of those tests is to combine somehow two of the bodies in the system so that their joint attraction on the third body can be computed. It is not easy to extend this to much more complicated cases where N>3. By analyzing the projected motion of the general N-body system on a given axis, Marchal (1990) obtained a sufficient condition for escape. If the N-body system is arbitrarily divided in two subsystems, the condition for escape is:

$$\frac{d\lambda}{dt} \geq \sqrt{\frac{2GMA}{\lambda}} \tag{1.8}$$

where λ is the distance between the centers of mass of the two subsystems, G is the

gravitational constant, and M is the total mass of the N-body system, and A is calculated as follows:

$$A = \frac{M^2}{M - m_1} \sum_{k=2}^{N} \frac{m_k}{[m_1 + 2(m_2 + ... + m_{k-1}) + m_k]^2} \tag{1.9}$$

where m_1, m_2, ..., m_k are the mass of the individual components of the N-body system. Note that λ is calculated along an arbitrarily chosen axis and, once the axis is chosen, then the stars are labelled 1, 2, ... k following the condition that the position of the stars on that axis, x, is increasing, i.e. $x_i > x_{i+1}$. The condition 1.8 has to be checked for all possible divisions of the N-body system in all of its possible subsystems.

The Marchal's test involves only a one-dimensional projected motion state of the system at any given instant. This makes it well-adapted to studying real stellar systems, multiples in particular, of which the full motion states are generally unavailable. Though determining the motion state of a hierarchical multiple can be achieved by orbit fitting, the results are unreliable if the multiple is in the disintegration phase. Moreover, for systems with such a long orbital period that they display almost no orbital motion during the observation periods, one can only determine the PM of the component stars. This would make Marchal's test a preferable, if not indispensable, tool for identifying disintegrating systems.

To test visual triple stars, Li et al. (2009) have designed an algorithm for practicality to make good use of two-dimensional kinematic data. They then applied this algorithm to 24 HIPPARCOS triple systems with the estimated mass of their components already obtained. A reliable set of probabilities for a real triple star disintegrating system was eventually calculated. Ten out of 24 of their triple systems were believed will have an unavoidable escape event, i.e. those systems will disintegrate eventually.

Ultimately, the main difference between my method, which I will describe in Chapter 2, and Li et al. (2009) method is that they use the dynamics of the system, i.e. they need to know the mass of the objects in the system and their velocity. Velocity is easy to obtain, but masses are hard to measure and mass estimates can be very uncertain. On the other hand, my method relies solely on PM, distance and separation, which are easier quantities to measure and obtain.

1.4 Ultra-cool populations

Among the population of celestial objects, those with $T_{\rm eff}$ below 2700 K (spectral type M7 and later) are generally referred to as UCDs. This class includes VLMSs, BDs and GESPs, and it is in particular on the first two types of objects that I will focus in this thesis, as possibly ejected members of disintegrating multiple systems. A more detailed discussion of the properties of these ultra-cool objects will be present in the following sections.

1.4.1 Effective temperature

To clarify, UCDs as mentioned above is a temperature-based definition, referring to objects that have $T_{\rm eff}$ that are below 2700 K, whereas BDs are objects that have a mass that is below 0.075 $M_\odot$ (although the mass limit depends on metallicity and can be as high as 0.090 $M_\odot$ for metal-poor stars). Hence, not all UCDs are BDs. For example, LMSs will cool, but eventually reach a minimum luminosity they can maintain through steady internal fusion, becoming mid-L spectral type UCDs. On the other hand, since BDs cannot sustain stable hydrogen burning, they will just darken gradually over their lifetime while most of the energy produced from gravitational contraction is radiated away. So, overall, this means that late-M, early-L, and mid-L are a mixture of VLMSs and BDs, while late-L, T and Y dwarfs are all BDs.

There are four types of UCDs observed up to date: M, L, T and Y. One of the main differences between them is their $T_{\rm eff}$. Most M dwarfs are stars and have $T_{\rm eff}$ ranging between 2300 K and 3800 K whereas the $T_{\rm eff}$ for L dwarfs is approximately between 1400 K and 2300 K. The $T_{\rm eff}$ of T dwarfs is from around 500 K to 1400 K, and since Y dwarfs are cooler than the T dwarfs so their $T_{\rm eff}$ is below 500 K. I will explain the atmospheric differences that occur with the temperature changes in section 1.4.3 to 1.4.6 below. Both the age and mass of these substellar objects influence the distribution of their $T_{\rm eff}$ and luminosity (i.e. (Luminosity, $T_{\rm eff}$) = Function (Mass, Age); lower mass BDs are cooler and fainter than the more massive ones of the same age but are physically larger) and can be predicted by evolutionary models (e.g. Chabrier & Baraffe, 2000; Saumon & Marley, 2008; Allard et al., 2013; Allard, 2014). The evolution of $T_{\rm eff}$ (in K) with age (in Gyrs) for various objects of various masses (e.g. LMSs, BDs and GESPs) is shown in Figure 1.8 (Figure 8 from Burrows et al., 2001). The blue lines represent the stars and the green lines correspond to BDs that have mass above 13 $M_{\rm Jup}$ (the deuterium-burning limit) whereas the GESPs that have mass equal to or

below 13 $M_{\rm Jup}$ are shown by red lines. The gold dots mark the ages for a given mass at which 50% of the deuterium has been burned and the magenta dots mark, for a given object, when 50% of the lithium has been burned. The horizontal dashed lines indicate the approximate realms for the L and T dwarfs as the regions of L and T dwarf are still poorly determined and depend also on metallicity. It also shows that the majority of BDs evolve from spectral types M (late) to L to T to, lastly, Y.

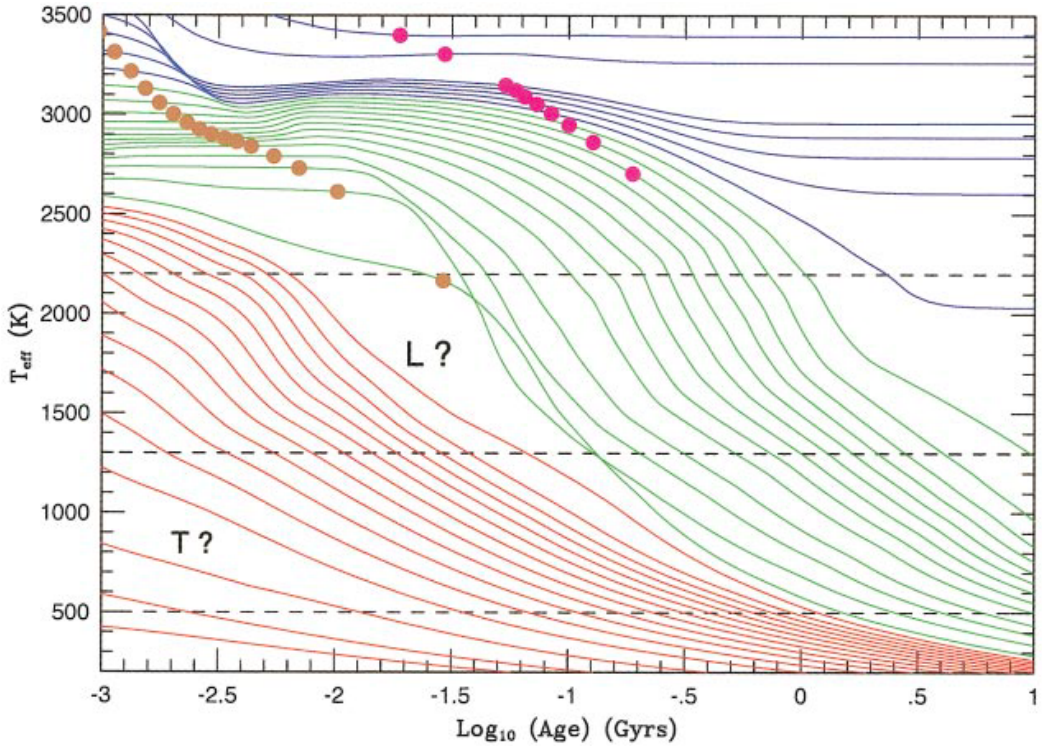

Figure 1.8: The evolution of $T_{\rm eff}$ (in K) with age (in Gyrs) for various mass such as LMSs, BDs and GESPs (Figure 8 from Burrows et al., 2001).

Essentially, stars at the lowest mass end contract at a rapid rate as pre-stellar objects; hence they undergo a decline in luminosity in the first phases of their evolution. They will then join the main sequence and become stable due to the energy output from the fusion within their core. Their radius, luminosity and $T_{\rm eff}$ remain constant throughout their lifetime and become late-M or early-to-mid-L dwarfs, and reach relatively compact states where the radius is roughly equivalent to the radius of Jupiter. At the beginning of the evolution of these LMSs and high-mass BDs, there is a short deuterium burning phase (within $\sim$20 Myr) depending on their mass (Chabrier & Baraffe, 2000). Substellar objects will then carry on with their contraction, cooling and

fading slowly and steadily. They will then evolve from spectral type late-M to L, then T, and the least massive ones will eventually become Y dwarfs. Objects below the deuterium burning limit (i.e. GESPs) never reach the tremendously compact phases where their radii stabilize to approximately the radius of Jupiter, which is typical at the higher mass end of the BDs regime. In general, the radius of a stellar object is approximately a linear function of its mass. On the other hand, BDs and GESPs undergo a mass-radius relation inversion after $\sim$100 Myr. More massive objects will end up with smaller radii because their internal structure is under the influence of electron degeneracy pressure, and the electron density is the only parameter that plays a role. In this case, more massive objects become extremely dense in order to balance their higher self-gravity (the objects with the largest radii are those with masses around 4 $M_{\rm Jup}$, i.e. GESPs; e.g. Zapolsky & Salpeter 1969; Hubbard 1977).

1.4.2 Spectral type distribution

The Morgan-Keenan (MK) system of classification (Morgan et al., 1943) is the standard stellar classification for stars based on their spectral characteristics. The measurement of the photospheric temperature of an object can describe the ionization of its photosphere. Analysing it can help deduce the chemical elements present in the candidate object from the absorption lines in the spectrum. The temperature conditions that are necessary for a certain excitation of those elements can be determined from the spectrum as well. The different spectral classes being used for main sequence stars are OBAFGKM (Morgan et al., 1943), where type O indicates the most massive and hottest stars and type M indicates the smallest and coolest stars in the main sequence. There is a number accompanying each letter between 0 and 9 representing tenths of the range between two classes. To determine the spectral type of a star, both its optical spectrum and NIR spectrum are used. More often, astronomers use optical spectra for O to M as they are more temperature dependent (Morgan et al., 1943) and the majority of the flux is emitted at optical wavelengths. In addition, the earlier spectral types in the main sequence are determined via atomic lines but molecular absorption bands are used to classify M dwarfs as these bands start to appear in G stars and strengthen along K and M. Spectral type L (Kirkpatrick et al., 1999), T (Burgasser et al., 2006) and Y (Cushing et al., 2011; Kirkpatrick et al., 2012) were later added to the previous MK system after the discovery of colder and colder BDs. Note that while the temperature of these substellar objects drops, dust grains and clouds start to form. In addition, their metallicity

and surface gravity also play an important role in affecting their spectral type. In the case of metallicity, this is because the objects look increasingly red with high metallicity, as with higher metallicity there is more dust (e.g. Hiranaka et al., 2016). BDs with lower metallicity on the other hand have less dust and so appear bluer (e.g. Zhang et al., 2019, and references therein). Moreover, log g is another atmospheric parameter that alters the appearance of these faint objects. The higher the log g is, the denser the BD becomes. This then not only leads to more collision-induced-absorption (CIA) by H_2 (Saumon et al., 1994) but also leads to more dust sinking down towards the center of the star, hence less dust remains in the atmosphere (Saumon & Marley, 2008). The source will then look bluer as a result. On the other hand, BDs look redder with lower log g. Since the ultracool object is less dense in comparison and so dust stays higher up closer to the surface, as well as having less CIA by H_2 altogether (Faherty et al., 2014, 2016).

Kirkpatrick et al. (1993) was the first group to analyse the spectrum of GD 165B and deduced it to be an intermediate transition object between stars and GESPs. In general, the spectrum of GD 165B lacks common and typical features of M dwarfs such as the absorption bands of titanium oxide (TiO). Additionally, it cannot be a planet either, due to the absence of the spectral features of Jupiter and Saturn, methane (CH_4) and ammonia (NH_3) respectively. However, the first unambiguous BD ever observed was GL 229B, by Nakajima et al. (1995). The absorption bands of CH_4 can be seen in its spectrum, and also shows a general similarity with the spectrum of Jupiter (Oppenheimer et al., 1998). PPI 15 and Teide 1 in the Pleiades were also identified to be BD candidates around the same time (Stauffer et al., 1994; Rebolo et al., 1995) and lithium (Li) was detected in their spectra for the first time; they were then confirmed to be substellar objects as well (Basri et al., 1996; Rebolo et al., 1996). As more and more of these new objects were found, it became clear that they belonged to two different groups. The spectra of some of these newly found substellar objects were similar to GD 165B, therefore very different from M dwarf. Additionally, objects with spectra similar to GL 229B showed a clear distinction from both M dwarf and GD 165B alike. This made necessary an extension to the MK system of classification and two new spectral classes were then added. Type L was introduced for GD 165B type of objects and type T was introduced for GL 229B type of objects (Kirkpatrick, 2005). An example of the spectral sequence from M dwarfs to GESPs is shown in Figure 1.9 (reproduced from Marley & Leggett, 2009).

However, even cooler objects were discovered continuously (e.g. Lucas et al., 2010)

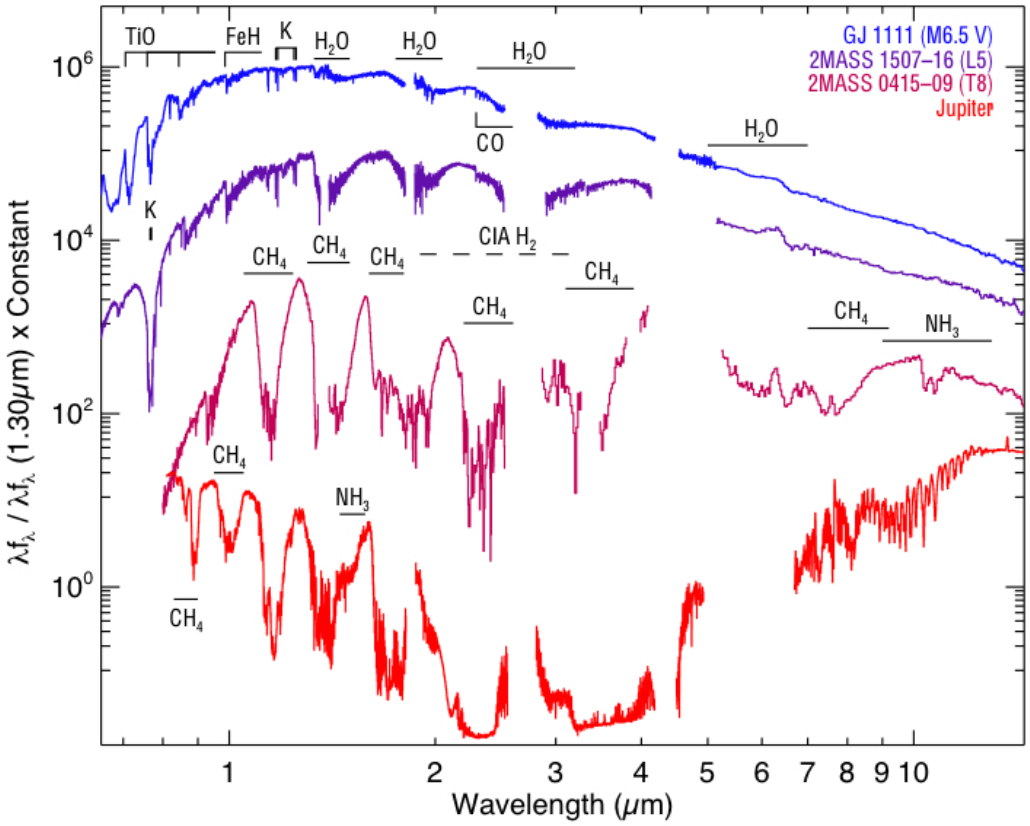

Figure 1.9: An example of spectral sequence, showing a late M dwarf (in blue, at the top) a L dwarf (in purple), a T dwarf (in magenta) and the spectrum of Jupiter (in bright red, at the bottom). The differences between the 4 types of object are clear (reproduced from Marley & Leggett, 2009).

but the coolest and faintest objects identified to date (Cushing et al., 2011; Kirkpatrick et al., 2012) were found by the NASA's Wide-field Infrared Survey Explorer (WISE; Wright et al., 2010). A more detailed description of the spectral types will be given in the following sub-sections.

1.4.3 M dwarfs

M dwarfs are a mixture of cold and old hydrogen burning VLMSs as well as high-mass and young BDs. Only the very young BDs are hot enough to be late M dwarfs i.e. from ∼M6.5 and onward. An example of these young BDs are the members of the young open cluster Pleiades, which have an estimated age of ∼100 Myr (Almeida

et al., 2023). In 1991, one way to classify objects between K5 to M9 was suggested by Kirkpatrick et al. (1991), where spectral features as well as the spectral slope around the 6300 to 9000 Å region were used. This is because the peak of the spectral energy distribution of M dwarfs, as well as the main absorption features, are located in the redder part of the optical spectrum because of their lower temperature (Berriman & Reid, 1987; Liebert et al., 1984). The most characteristic features of M dwarfs in the red part of the electromagnetic spectrum are the absorption bands of water (H_2O) and the metal-oxide bands. TiO is found from K7 onward and produces especially strong absorption bands in the early-M dwarfs' spectra and become progressively weaker towards the later types. Vanadium oxide (VO) is also found in late-type objects (e.g. Kirkpatrick et al., 1991). The presence of metal hydrides such as magnesium hydride (MgH), calcium hydride (CaH), and iron hydride (FeH) also causes additional important absorption bands for this spectral type. Calcium (Ca I and Ca II), sodium (Na I), and potassium (K I) cause the main atomic lines within M dwarfs' optical spectra.

1.4.4 L dwarfs

The following spectral class is type L, which was defined and categorized by Kirkpatrick et al. (1999) for the optical spectra and Geballe et al. (2002) for the NIR spectra. L dwarfs contain a mixture of old LMSs and intermediate age BDs. The combination of both atomic lines and molecular absorption bands can be found in the spectra of early-Ls. The most prominent lines and bands that were used to distinguish L dwarfs from other low-mass objects are caused by the presence of alkali metals such as K, rubidium (Rb), Na, and cesium (Cs), metal-oxides (mainly TiO and VO) and hydrides such as MgH, CaH, chromium hydride (CrH), and FeH. The absorption lines of Na and K start to deepen while the absorption bands of TiO and VO become shallow and almost invisible for objects in mid-L spectral classes, because TiO and VO condense into dust grains. Then, in the spectra of late-Ls, it can be seen that the bands of H_2O have deepened while hydride bands have become weaker. Moreover, the deep line of Ca and the strong band of carbon monoxide (CO) at wavelength $\sim$2.1 μm and $\sim$2.3 μm respectively are the main sources of opacity in the red end of the spectra (i.e. $\sim$2–2.3 μm). More complex molecules are "trapped" into dust grains that form layers of clouds inside the photosphere of L dwarfs, having a strong influence in shaping the emergent spectral energy distribution (e.g. Helling et al., 2008; Helling & Casewell, 2014). In addition, while Rayleigh scattering by dust clouds reddens the emerging

flux, warm dust can also "re-warm" the atmosphere. Though the optical and the IR classification schemes are influenced by different atmospheric phenomena, numerous studies show that, with a few exceptions, optical-based and IR-based L spectral types overlap (i.e. Reid et al., 2001; McLean et al., 2003).

1.4.5 T dwarfs

As time progressed, more low-mass objects were discovered and it was the discovery of GL 229B (Nakajima et al., 1995) that forced the introduction of the new spectral class T. Its classification scheme based on optical spectra was defined by Burgasser et al. (2003b). Nevertheless, as most T dwarfs are too faint for optical spectroscopy, the classification scheme based on NIR spectra by Burgasser et al. (2006) is the one being widely used. There are solely BDs in this class as hydrogen burning stars never become cold enough to be T dwarfs. In addition, due to the recognizable CH_4 absorption bands that can be observed within their spectra, T dwarfs are also called methane dwarfs. Moreover, hydride bands disappear in this class while the depth of H_2O bands increases as they become the main absorbers in mid- and late-T type objects. Furthermore, the absorption lines of alkali metals (K and Na) in the optical spectrum ($\sim$7000 Å) are on the edge of merging due to their depth and width (Burgasser et al., 2006). Separated by the absorption bands of CH_4 and H_2O, the four peaks (1.08, 1.27, 1.59 and 2.08 μm) in the spectrum are a characteristic of late-T spectra. Note that the CIA of H_2 causes the peak at $\sim$2.08 μm to be further damped (flattened). The combination of CIA of H_2 with the strong absorption by H_2O and CH_4 in the H and K band, besides the absence of dust, means that T dwarfs look relatively blue in terms of NIR colours.

1.4.6 Y dwarfs

The coolest BDs discovered so far are classified as Y dwarfs. They share similar masses and temperatures as GESPs. Although the theory has not yet been confirmed, the existence of H_2O clouds in these objects at 300–400K has been predicted (Morley et al., 2014). Only a few of these cool objects have been discovered (Cushing et al., 2011; Kirkpatrick et al., 2012; Meisner et al., 2020a,b) and the most representative Y Dwarf is WISEP J1828+2650 (Cushing et al., 2011). The classification scheme is only preliminary due to the limited sample size, but from the spectra obtained by Kirkpatrick et al. (2012) some peculiar characteristics have been identified, which can be used to distinguish type Y from type T. T dwarfs, which are hotter than Y dwarfs, are blue

in NIR colours. Y dwarfs, whose $T_{\rm eff}$ is below 400K, turn red again because the peak of the spectral energy distribution moves to longer wavelengths. The turning to red of the NIR spectrum was one of the characteristics predicted by models for the new Y spectral type (Burrows et al., 2003; Kirkpatrick, 2008). Y dwarfs show absorption bands of H_2O and CH_4, and NH_3 also begin to play a more important role in shaping the NIR spectra. Note that moving to later types, H_2O bands become deeper. On the other hand, atomic lines such as K and Na become shallower because K condenses into clouds of potassium chloride (KCl), and Na condenses into sodium sulfide (Na_2S). Though, at $T_{\rm eff}$ of approximately 350K, a reasonable amount of H_2O, CH_4 and NH_3 condenses into clouds too, and since all three bands blend together, the detection of NH_3 is a challenge (note that only if the spectra have high enough signal-to-noise ratio, NH_3 might be observable in the H-band in some Y dwarfs).

1.5 Motivation

In this thesis I aim to identify and study LMSs, BDs, and GESPs ejected from post-encounter disintegrating multiple systems. These objects can be characterised more easily because they avoid the technological challenge of having to block the glare of the bright parent stars, a problem that has so far limited the characterisation of exoplanets. Well studied LMSs, BDs and GESPs are fundamental benchmarks to constrain the formation theory and the atmospheric models for these very cold objects.

Moreover, the recent discovery of candidates for free floating planets (Mróz et al., 2020; McDonald et al., 2021) begs the questions of how these objects came to exist. It is unlikely that they form on their own and the most likely explanation is that they are ejected from their own planetary systems (Rasio & Ford, 1996), but how these ejections happen is still an open question. One possibility is that they get ejected during the disintegration of a multiple system because it is likely that the planets orbiting the components get disrupted during the close interactions that lead to the disintegration of the systems (Veras & Tout, 2012; Veras et al., 2014).

Disintegrating multiple systems must also be taken into account when measuring the initial mass function and the multiplicity fraction of stars. These observational constraints then can be compared to the predictions of the current stellar formation models (e.g. Bate, 2012), helping to test and to improve them.

Also, the low-mass community has been trying to find out which is the dominant formation mechanism for UCDs. One of these theories is the disk fragmentation (e.g.

Stamatellos et al., 2007), which says that BDs form from a disk around a star and then get ejected. Determining the rate at which multiple systems with low-mass components disintegrate can help to test this theory by establishing if the ejection rate is high enough to explain the observed population of UCDs.

Last but not least, studying disintegrating multiple systems can help us establish the initial conditions for capture, because disintegration and capture are both possible results of a close encounter of a multiple system with a star or with another multiple system (e.g. Heller, 1991). So, by observing disintegrating multiple systems we can understand which type of close encounters result in capture and which type result in disintegration.

CHAPTER 2

Analysis methods and candidate samples

In this chapter I will describe the catalogues and the selection method used in this thesis to identify the initial list of candidate disintegrating multiple systems. The method is also described in Yip et al. (2016) and Yip et al. (2023).

2.1 Catalogues

In this chapter and in the following part of my thesis I have used several astrometric, photometric and spectroscopic surveys. In the following subsections I give a brief overview of the main ones.

2.1.1 Gaia

Gaia launched in 2013 and its primary goal is to measure extremely precise positions, parallaxes, and PMs for $\sim$2 billion stars, mostly in the Milky Way (Gaia Collaboration et al., 2016a). Gaia uses a wide band, called G, which covers the wavelength range 3200–10000 Å. Gaia also has two additional bands called the blue and red photometers (BP and RP) which can also be used to determine stellar properties such as

temperature, mass, age and metallicity. The BP and RP instruments also provide low-resolution spectra. The blue photometer operates in the wavelength range 3300–6800 Å while the red photometer covers the wavelength range 6400–10500 Å. Gaia also has a spectroscopic instrument, called the Radial-Velocity Spectrometer (RVS) which is used to determine the RV of bright stars by acquiring high-resolution spectra in the spectral band 8470–8740 Å (centered on the Ca triplet) for objects up to magnitude ∼17. RVs are measured with a precision between 1 km s^{-1} for the brighter stars (V = 11.5 mag) and 30 km s^{-1} for the fainter stars (V = 17 mag).

The latest Gaia data release is DR3 (Gaia Collaboration et al., 2022b), which contains positions, parallaxes, PMs, magnitudes, RV, and atmospheric parameters ($T_{\rm eff}$, log g, [Fe/H]). It also contains a huge number of additional data and parameters, e.g. the BP, RP, and RVS spectra, the light curves and variability information, orbital parameters for multiple systems, etc.

2.1.2 Tycho-Gaia Astrometric Solution (TGAS)

Gaia DR1 is based on the first 14 months of Gaia's observations. This is not long enough to reliably distinguish between parallax and PM. For most stars, therefore, Gaia DR1 gives only positions and magnitudes. Parallaxes and PMs were nevertheless measured for about two million bright stars by combining the Gaia observations with the much earlier HIPPARCOS and Tycho-2 positions (epoch 1991.25). These data serve as additional "observations" in the astrometric solution for these stars. The ∼25 year time difference between the earlier catalogues and Gaia makes it possible for the PMs to be determined with reasonable precision, which can then be disentangled from the parallax. This method is described in details in Michalik et al. (2015), and the results, known as the Tycho-Gaia Astrometric Solution (TGAS), are described in details in Arenou et al. (2017). Since TGAS was the catalogue I used for the initial selection of candidate disintegrating systems, here I summarize the most important limitations (for more details, see Arenou et al., 2017).

TGAS has a hard cutoff at $G < 4.5$ mag because very bright stars often have poor astrometric solutions. There is a faint TGAS tail ($G > 13.5$ mag) which is mainly due to Tycho-2 stars that have been resolved into fainter components by Gaia, and also a few variable stars that were brighter in Tycho-2 and are now fainter in TGAS. Stars with nearby neighbors are prone to astrometric errors in TGAS due to mis-matching.

For bright stars ($G < 12$ mag) Gaia uses "gate voltages" to avoid saturation. But

sometimes the gates didn't work, which lead to some bright G magnitudes being wrongly measured as fainter G magnitudes. This causes some erroneous colours, so very blue and very red sources ($G - G_{BP} > 3$, $G - G_{RP} > 3$) have been rejected from TGAS. Although this was done to get rid of wrongly measured objects, it also gets rid of any objects that are genuinely very red or very blue.

TGAS is also quite incomplete for stars with high PM. Arenou et al. (2017) found that 40% of stars in the range $0.5 <$ PM < 3.5 arcsec yr^{-1} are missing. Also, all stars with PM > 3.5 arcsec yr^{-1} have been excluded from TGAS because the astrometric solutions are poor in this range. Stars with neighbors < 2 arcsec away have unreliable astrometric solutions, so most have been rejected from TGAS. Also stars with 2 or more brighter neighbors ($\Delta G \geq 0.2$ mags) within 2–4 arcsec often have poor astrometric solutions, which Arenou et al. (2017) shows leads to incompleteness in this separation range in crowded fields.

Moreover, a lack of $G < 6$ mag calibration sources with a wide range of colours leads to non-calibrated G magnitudes in Gaia DR1, and thus missing sources in TGAS because sources are required to have a measured G magnitude to enter the release. There is also incompleteness at low ecliptic latitude (near the ecliptic plane), because due to the Gaia Ecliptic Pole Scanning Law there are fewer observations on either side of ecliptic latitude $\pm 45^{o}$, with fewest around the ecliptic plane. Finally, there is also some incompleteness around $G = 10.5 - 11.5$ mag due to reduced astrometric accuracy resulting from duplicate sources being more common in this G range. This is quantified by Arenou et al. (2017) in TGAS as a $\sim 10 - 15\%$ level of incompleteness for $G = 10.5 - 11.5$ mag.

2.1.3 GALactic Archaeology with HERMES (GALAH)

The GALactic Archaeology with HERMES (GALAH) survey is a large observing program using the High Efficiency and Resolution Multi-Element Spectrograph (HERMES) on the Anglo-Australian Telescope. GALAH obtained the highest spectral resolution spectra for over a million stars of all ages and locations in the Milky Way, with the main goal being to trace the full history of the Galaxy. The GALAH Survey had three data releases (Martell et al., 2017; Buder et al., 2018, 2021), which provide stellar parameters ($T_{\rm eff}$, log g, [Fe/H], α-elements enrichment [α/Fe]), RV, distance modulus and reddening. Their sample was selected using a catalogue built from the Two Micron All Sky Survey (2MASS; Skrutskie et al., 2006), The AAVSO Photometric All-Sky

Survey (APASS; Munari et al., 2014) and The Fourth US Naval Observatory CCD Astrograph Catalog (UCAC4; Zacharias et al., 2013) data, and contained main sequence stars out to a maximum distance of 3 kpc and giant stars out to a maximum distance of 10 kpc.

2.1.4 The Apache Point Observatory Galactic Evolution Experiment (APOGEE)

The Apache Point Observatory Galactic Evolution Experiment (APOGEE, Majewski et al., 2017) is a large-scale, stellar spectroscopic survey conducted in the H band. The high-resolution APOGEE spectra (R$\sim$22,500) provide detailed chemical and kinematic information for target stars. The first part of the APOGEE Survey (Eisenstein et al., 2011) happened from September 2011 to July 2014 using the APOGEE-North spectrograph on the Sloan Foundation 2.5m Telescope of Apache Point Observatory (APO). The second part of the survey (Blanton et al., 2017) was carried out from July 2014 through Summer 2020 and continued taking data at APO but also with the APOGEE-South spectrograph on the Irénée du Pont 2.5m Telescope of Las Campanas Observatory (LCO).

Combined spectra obtained during multiple observations are one of APOGEE's primary data products. Stellar atmospheric parameters and chemical abundances are derived from these combined spectra using the APOGEE Stellar Parameters and Chemical Abundances Pipeline (ASPCAP).

The latest data release is DR16 (Jönsson et al., 2020) and contains the spectra of about 430,000 stars covering both the northern and southern sky, from which RVs, stellar parameters, and chemical abundances of up to 26 species are determined.

2.1.5 The Radial Velocity Experiment (RAVE)

The Radial Velocity Experiment (RAVE, Steinmetz et al., 2006) is a magnitude-limited ($9 < I < 12$) spectroscopic survey of Galactic stars randomly selected in the southern hemisphere. The RAVE medium resolution spectra (R $\sim$ 7500) cover the Ca-triplet region (8410–8795 Å). The final data release is DR6 (Steinmetz et al., 2020a,b), and contains the wavelength-calibrated and flux-normalized spectra for 451,783 stars obtained from 12 April 2003 to 4 April 2013. The final data release consists of spectra, error spectra, spectral classification, derived RVs, and cross matches with other rele-

vant catalogs.

Further data products provided by the RAVE survey are spectroscopically derived stellar atmospheric parameters ($T_{\rm eff}$, log g, and the overall metallicity), abundances of the elements Fe, Al, and Ni, as well as an overall [α/Fe] ratio.

2.1.6 Other catalogs

Data for few of the candidate disintegrating multiple systems were taken from other surveys, which I briefly mention here.

Large Sky Area Multi-Object Fibre Spectroscopic Telescope (LAMOST)

The Large Sky Area Multi-Object Fibre Spectroscopic Telescope (LAMOST) surveys are conducted with the Guo Shoujing Telescope, in China. The stellar spectroscopy survey measures RV and atmospheric parameters for $\sim$5 million stars using mid-resolution spectra. The latest public data release was DR8 (Wang et al., 2022).

PASTEL

PASTEL is a bibliographical catalogue compiling estimations of stellar atmospheric parameters (Soubiran et al., 2010). It provides $T_{\rm eff}$, log g, and [Fe/H] obtained from detailed analyses of high-resolution (R $\geq$ 25,000), high signal-to-noise spectra (S/N $\geq$ 50). The 2016 version of the catalogue (Soubiran et al., 2016a) includes 64,082 estimations of either just $T_{\rm eff}$ or $T_{\rm eff}$, log g, and [Fe/H] for 31,401 stars, taken from 1142 papers.

TESS Input catalog (TIC)

The Transiting Exoplanet Survey Satellite (TESS) Input Catalog (TIC) is a compiled catalog of stellar parameters for every persistently visible, stationary object in the sky. The current version is TIC-8.2 (Paegert et al., 2022). TIC uses the GAIA DR2 catalog as a base and adds a large number of other photometric catalogs, including 2MASS, UCAC4, APASS, The Sloan Digital Sky Survey (SDSS; York et al., 2000), WISE, etc. Then, they use the magnitudes and various empirical/observational relations to estimate $T_{\rm eff}$, log g, and [Fe/H]. If spectroscopic estimates of $T_{\rm eff}$ and [Fe/H] are available, those are used instead. There are roughly 1.5 billion stellar and extended sources in TIC.

Ammons et al. (2006)

Ammons et al. (2006) used a procedure to uniformly estimate fundamental stellar properties of Tycho-2 stars using spline functions of broadband photometry and PM found in HIPPARCOS/Tycho-2 and 2MASS. They provide estimates of $T_{\rm eff}$ and distance for 2.4 million stars and for stars that appear to be FGK dwarfs they also derive [Fe/H].

The Penn State - Toruń Centre for Astronomy Planet Search (PTPS)

The Penn State - Toruń Centre for Astronomy Planet Search (PTPS) used the High Resolution Spectrograph of the 9.2 m Hobby-Eberly Telescope (Zieliński et al., 2012). Niedzielski et al. (2016) presented a sample of 744 evolved stars from the PTPS. Their atmospheric parameters were determined using equivalent widths of Fe I and Fe II lines. Rotational velocities were obtained from fitting synthetic spectra and RVs were from cross-correlation. They determined stellar masses, ages, and luminosities with a Bayesian analysis of theoretical isochrones.

2.1.7 Comparison of [Fe/H] values from different surveys

When comparing [Fe/H] measurements from different surveys it is important to take into account possible systematic offsets between surveys. The metallicity used for the majority of the objects in this thesis come from three surveys: GALAH, RAVE, and Gaia DR3. The exceptions are TYC 6813-286-1 for which I get the metallicity from Allen & Barbuy (2006), and TYC 9281-2422-1 and TYC 7731-2128-1A for which I get the metallicity from Ammons et al. (2006).

GALAH validated their metallicity estimates using the Gaia FGK Benchmark Stars (Version 2.1; Jofré et al., 2018) and found a systematic [Fe/H] shift of +0.1 which they applied to their published metallicity values (see section 4.1.3 in Buder et al., 2021). RAVE performed an extensive comparison of their metallicities with several other surveys, including GALAH. Kunder et al. (2017) found negligible [Fe/H] systematic offsets between RAVE and GALAH of -0.07 ± 0.45 for stars with signal-to-noise ratio < 50 and $+0.04 \pm 0.13$ for stars with signal-to-noise ratio > 50 (see Section 7.5 and Table 5 in Kunder et al., 2017). Gaia DR3 also checked the accuracy of their metallicity estimates against a number of surveys, including GALAH and RAVE. Fouesneau et al. (2022) found that the GSP-Phot metallicities from Gaia are typically too low by 0.2 and have a median absolute deviation with respect to the other surveys of 0.2 (see

Section 3.2.1 in Fouesneau et al., 2022). In this thesis I have applied the 0.2 systematic correction to the values taken from Gaia, and I use ± 0.2 as their uncertainty. Finally, I found no systematic comparison between the [Fe/H] published by Allen & Barbuy (2006) and Ammons et al. (2006) and other surveys, so I cannot comment on possible systematic offsets in those values. Overall, I conclude that there are no remaining systematic offsets in the [Fe/H] values we use here, with the possible exception of the [Fe/H] values from Allen & Barbuy (2006) and Ammons et al. (2006).

2.2 Identifying initial candidate associations

To identify candidate disintegrating systems I used a method first described in Yip et al. (2016), where I applied it to the HIPPARCOS (van Leeuwen, 2007) and *Gliese-Jahreiß* catalogues (Gliese & Jahreiß, 1979). With the release of TGAS (Michalik et al., 2015), I applied this method to extend the search for further studies. The method is described in details in this Section and also in Yip et al. (2023).

2.2.1 Separation constraints

First, I searched for objects close in the sky and with common distance. I used TGAS because it provides very accurate PM and distance measurement for 2.5 million stars with a wide range of spectral types.

I began by trimming the TGAS catalog and only kept stars with total PM > 30 mas yr^{-1} because I want systems/stars that can collide with each other with a significant relative PM, so that the components will disintegrate with significantly different PM that I will be able to measure. Given the typical distance of TGAS stars (30-100 pc) this PM cut corresponds to a tangential velocity of 5-15 km s^{-1}. This cut risks removing real disintegrating systems where one or more of the components have low tangential velocity (because their velocity vector is aligned with the velocity vector of the Sun). When Gaia DR3 (Gaia Collaboration et al., 2022b) was released, I updated all of the astrometric information for our systems, but I did not redo the the initial selection of candidates. However, with the more accurate parallaxes by Gaia DR3 and future Gaia data releases I will be able to lower the minimum PM threshold or even remove it entirely during future searches. Then I kept only stars with PM/$\sigma_{PM} > 10$ in order to select only very accurate measurements, so that the relative PM of the components can be determined with high significance. I also cut at a distance of ≤ 300 pc (where dis-

tance = $1/\varpi$) because I want to identify UCDs in these systems and, given the intrinsic faintness of UCDs, even the hottest and brightest among them can only be detected by Gaia out to $\sim$300 pc. The resulting sample had typical parallax uncertainties in TGAS of $<$10%.

The following step was to search systems out to a maximum separation. The widest known stellar binary systems have separations of $\sim$200 kAU (e.g. Caballero, 2010; Caballero et al., 2006) however the maximum separation observed for main sequence star-brown dwarf binaries and white dwarf-brown dwarf binaries is in the 20–30 kAU range, though they are more common out to $\sim$5 kAU (see e.g. Pinfield et al., 2006; Gizis et al., 2001a; Day-Jones et al., 2011; Zhang et al., 2010; Faherty et al., 2010; Burgasser et al., 2005; Deacon et al., 2014). Overall, considering the fact that the systems I am searching for are disintegrating hence are expected to be extremely wide, I apply a conservative projected separation constraint of 50 kAU. This strikes a balance between the need to reduce the number of contaminants and our objective of selecting all possible candidates.

2.2.2 Spatial/Distance associations

Afterwards, I removed from the sample all systems where the components were at a distance that is not consistent with each other within 3 times their TGAS uncertainties. Once I identified the initial group of candidates, I also had to find the possible cause of disintegration. As discussed in the introduction (see Section 1.3.3), this could be the dynamical interaction between the candidate and a nearby star or system. I therefore searched for additional objects out to a 1 degree radius around our candidate systems. This separation cut was chosen as follows. First, I can only identify a disintegrating system as such if the disintegration has happened within the last few thousand years, otherwise the objects involved would have moved so far apart that a confident reconstruction of the events would be impossible. Therefore, if the disintegration has happened only a few thousand years ago, the components cannot have travelled further than 1 degree from each other, even assuming the highest PM known for a star ($\sim$10 arcsec yr^{-1} for Barnard's Star; Gaia Collaboration et al., 2018a).

2.3 Removing common PM systems

I then needed to differentiate between gravitationally bound systems and unbound disintegrating systems. If the components are still bound, then they should have common PM (hereafter CPM). On the other hand, disintegrating systems should not have CPM. So I removed systems where the difference between the PM of all components are within the combined errors, and I keep groups where the PM of at least one object diverges from the others by at least three times the combined errors. The resulting sample consists of two types of candidate systems. The first group (hereafter Group A) consists of associations where all components are moving away from each other, i.e. these are groups that are completely disintegrating. They are the result of more violent interactions. The other group of candidate systems (hereafter Group B) are groups where only one object is breaking away while the rest of the system remains bound. These systems are the result of a more gentle break up. Note that, while the initial selection searched for groups of three objects, during further analysis of the candidate systems I found additional components, usually found thanks to the deeper and more precise data from the latest Gaia data releases compared to TGAS.

Finally, I established whether the components of the systems were moving away from each other as expected for a disintegrating system or if they were moving towards each other, indicating a future close encounter. The separation between components as a function of time was computed as follows:

$$\begin{aligned} \mathrm{Sep(t)} = &\sqrt{[(\alpha_1 + \mu^*_{\alpha_1} \times t) - (\alpha_2 + \mu^*_{\alpha_2} \times t)]^2 \times cos(\delta_1)^2} \\ &+ \sqrt{[(\delta_1 + \mu_{\delta_1} \times t) - (\delta_2 + \mu_{\delta_2} \times t)]^2} \end{aligned} \tag{2.1}$$

Where α_1, α_2 and δ_1, δ_2 are the right ascension and the declination of the components in the system respectively, $\mu^*_{\alpha_1}$, $\mu^*_{\alpha_2}$ and μ_{δ_1}, μ_{δ_2} are the PM in right ascension and the PM in declination of the components in the system respectively[1].

Equation 2.1 can be used to trace both the past and future motion of the system. However this equation assumes straight line motion for the components and ignores any gravitational attraction between them. This is a reasonable approximation for the majority of the systems because at wide separation the effect of gravity should be small. Nonetheless, this approximation can lead to a small bias in the estimate of the time of closest approach and, therefore, I expect larger scatter in higher order systems where the complex gravitational interactions between the components add up. Using

[1] In this thesis, I use μ^*_α to indicate that the PM in the R.A. direction is already multiplied by $\cos\delta$.

Equation 2.1 I computed the time of closest encounter for all of our candidate systems. I propagated the uncertainties on the coordinate and PM using a Monte Carlo method.

Finally, I only keep systems that have the time of closest encounter in the past, meaning that they are currently dispersing, and that have come within 20 kAU of each other during the close encounter. For some systems, some of the components had their closest encounters in the past and some in the future. In those cases, I visually inspected the plot of separation as a function of time and interpreted case by case whether the system was disintegrating or not. Figure 2.1 shows an example of a disintegrating system and of additional un-associated objects in the field.

As mentioned above, although the initial selection of candidates was done using TGAS, when Gaia DR3 (Gaia Collaboration et al., 2022b) was released I updated all of the astrometric information for our systems. All of the results presented in this thesis are based on this updated astrometry.

The above method yielded 20 candidate disintegrating systems. Among these 20, I have followed-up 9 to further investigate their nature as disintegrating systems, and to search for additional low-mass components that may be getting ejected from them. They are listed in Table 2.1, where for every object I give the Gaia DR3 coordinates, parallaxes, and PM, as well as the current separation between the components and the time of their closest encounter. The details of the follow-up are given in the following chapters.

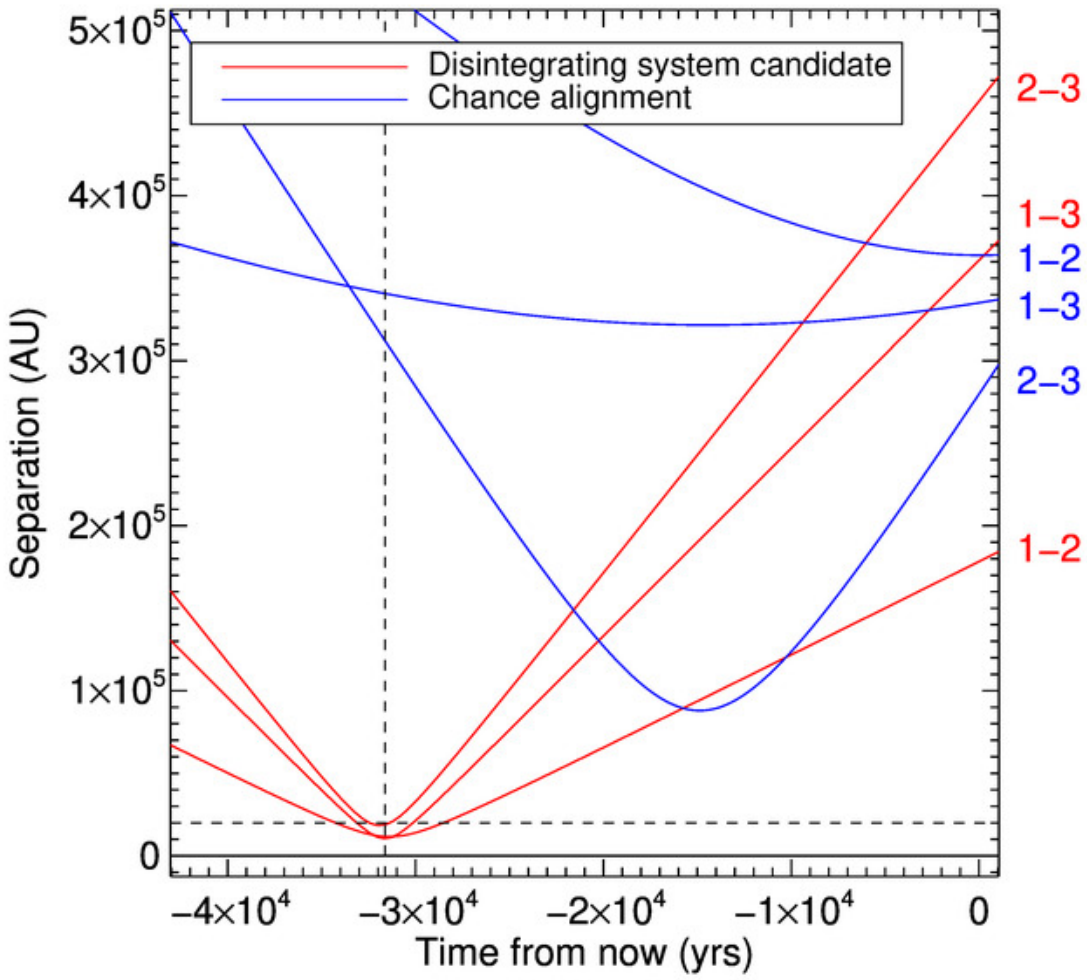

Figure 2.1: Back-tracked projected separation (AU) for the system consisting of TYC 4936-84-1 AB, TYC 4933-912-1 AB, and TYC 4934-796-1, which is one of the candidate disintegrating systems presented here. The separation between members of the system are plotted in red, while the separation between un-associated stars in the field are shown in blue. The horizontal dashed line indicates a projected separation of 20 kAU which is the typical separation of a wide binary. All three components of the system were within this limit ∼32,000 years ago.

Table 2.1: Astrometric data for the candidate disintegrating systems presented here. The name is from SIMBAD, and a "?" next to the name indicates that the association of this object with the system in question is dubious (see Chapter 3 and 4 for further details). Gaia ID is the Gaia DR3 designation. R.A., Dec, PM (μ_α^*, μ_δ) and parallax (ϖ) are from Gaia DR3. Sep. is the current separation between the components. The time of closest encounter ($t_{\rm closest}$) is derived using equation 2.1.

Name	Gaia ID	R.A. (deg)	Dec. (deg)	μ_α^* (mas yr^{-1})	μ_δ (mas yr^{-1})	ϖ (mas)	Sep. (arcsec)	$t_{\rm closest}$ (yr)
TYC 6813-1293-1	6046875561183621120	251.840515	-24.706553	-28.89±0.08	-34.89±0.06	8.42±0.07	0.0	-29956.0
TYC 6813-286-1	6046740488740710016	251.183212	-25.216904	-107.2±0.3	-98.5±0.2	9.8±0.2	2824.5	-29956.0
TYC 6813-643-1A	6046753549752392576	251.784424	-25.158779	-25.55±0.03	-88.66±0.03	8.82±0.03	1638.3	-29956.0
TYC 6813-643-1B	6046753584102505856	251.784139	-25.158305	-28.3±0.1	-87.59±0.07	8.98±0.09	1636.7	-29956.0
TYC 7240-1438-1	3462138227811420160	184.133972	-34.44865	-33.19±0.02	-2.45±0.02	5.49±0.02	0.0	-92590.0
TYC 7240-1159-1	3462913078568848256	183.732773	-34.064308	-47.13±0.03	11.41±0.02	4.84±0.03	1827.4	-92590.0
TYC 7240-850-1	3462739321372618112	182.755676	-35.062286	-73.6±0.02	-23.96±0.01	5.64±0.02	4636.6	-92590.0
TYC 4936-84-1A	3593854124477499520	174.488144	-5.006651	-49.37±0.05	-34.00±0.02	10.50±0.03	0.0	-30233.0
TYC 4936-84-1B	3593854124477587328	174.488539	-5.006091	-51.9±0.3	-32.6±0.1	10.3±0.1	2.5	-30233.0
TYC 4933-912-1A	3792133076403723904	173.969406	-4.017341	-106.85±0.03	74.58±0.02	11.91±0.02	4018.7	-30233.0
TYC 4933-912-1B	3792133076402865792	173.968396	-4.013940	-106.00±0.02	74.05±0.01	11.89±0.01	4031.2	-30233.0
TYC 4934-796-1	3599814851889741056	175.038681	-4.947755	15.44±0.02	-23.85±0.02	10.13±0.02	1985.8	-30233.0
TYC 9281-3037-1	5806792421244550656	241.931213	-71.349174	-367.21±0.02	288.76±0.03	6.11±0.03	0.0	-9677.0
TYC 9281-2422-1	5806506204622362112	244.929993	-72.214973	-20.04±0.05	-43.30±0.06	5.18±0.06	4593.2	-9677.0
TYC 9281-1175-1A	5806506685658712832	244.605225	-72.236076	-46.59±0.01	-31.74±0.01	5.46±0.01	4385.7	-9677.0
TYC 9281-1175-1B?	5806505208191451008	244.606052	-72.236789	…	…	…	4388.2	-9677.0
TYC 7731-1951-1	5391597005019395200	162.216339	-41.780659	-95.21±0.05	10.88±0.08	6.32±0.07	0.0	-8663.0
TYC 7731-2128-1A	5391592538253547648	162.319901	-41.896751	-56.518±0.009	-31.27±0.01	4.35±0.01	501.8	-8663.0
TYC 7731-2128-1B	5391592538254935296	162.319848	-41.896005	-57.34±0.09	-31.5±0.1	4.4±0.1	499.5	-8663.0
TYC 7731-1995-1AB?	5391594668557342592	162.366165	-41.806747	-36.77±0.01	3.08±0.02	4.04±0.02	413.0	-8663.0
TYC 7731-1995-1C?	5391594668558722048	162.367068	-41.806130	…	…	…	414.8	-8663.0
TYC 3023-1691-1	1529358453045295616	194.652451	43.726544	-42.25±0.01	17.42±0.02	3.77±0.02	0	-38623
TYC 3024-1493-1	1529282071350395264	195.358399	43.194831	4.20±0.01	-33.17±0.02	4.98±0.02	2658.3	-38623
TYC 3023-1688-1A	1529329831386038656	194.860547	43.216019	-29.55±0.01	-30.33±0.01	4.47±0.02	1916.6	-38623
TYC 3023-1688-1B	1529329655289938944	194.870658	43.222764	-29.7±0.1	-30.2±0.1	4.4±0.2	1901.1	-38623
TYC 3023-1688-1C?	1529329831386690048	194.860118	43.215513	…	…	…	1918	-38623
TYC 3440-338-1	828251358901595776	150.505219	52.381645	-139.89±0.02	7.12±0.02	9.08±0.02	0	-40958
TYC 3441-520-1	848336790641106176	154.384411	52.270422	65.85±0.01	0.40±0.02	9.44±0.02	8543.2	-40958
TYC 3440-300-1A	851212799526109824	152.466234	51.862281	-34.62±0.01	-38.63±0.02	8.95±0.02	4720.3	-40958
TYC 3440-300-1B	851212803821677696	152.466683	51.861956	-32.27±0.09	-39.1±0.2	8.9±0.1	4721.6	-40958
TYC 2061-642-1	4568436870286983936	258.375700	22.745615	24.83±0.02	-19.16±0.03	5.46±0.03	0	-29208
TYC 2061-148-1	4568675219493678080	258.235225	23.297989	10.357±0.009	49.22±0.01	4.86±0.01	2042.2	-29208
TYC 2061-270-1	4568260673546093312	257.736730	22.757966	-43.47±0.02	-20.11±0.02	5.55±0.02	2121.7	-29208
TYC 3160-1812-1	2068212295611195008	307.469884	42.357534	-94.1±0.1	-12.9±0.1	7.34±0.09	0	-34135
TYC 3161-177-1	2069513120946090496	309.330544	42.826703	51.11±0.01	36.23±0.01	7.59±0.01	5212.3	-34135
TYC 3161-434-1A	2069465292190285056	309.460325	42.769905	60.06±0.03	29.28±0.03	6.88±0.02	5482.2	-34135
TYC 3161-434-1B	2069465296487349760	309.460822	42.769879	61.9±0.1	31.7±0.3	7.0±0.1	5483.5	-34135
TYC 3161-434-1C	2069471240722080384	309.509966	42.794321	60.08±0.09	29.5±0.1	6.8±0.09	5632.0	-34135

CHAPTER 3

Confirming disintegrating system candidates through relative motion

In this chapter I will discuss the spectroscopic follow-up of four disintegrating system candidates. This follow-up allowed me to measure the RV and the metallicity of the objects in each system. The RV is needed to obtain the full kinematic of the system, which in turn will be fundamental for future dynamical simulations of the close encounter. The metallicity is needed to distinguish which of the components had common origin (i.e. those that have similar metallicity) and those that did not (i.e. those that have different metallicity). This will enable me to identify which objects used to form a multiple system and which object/s is/are the cause of the disintegration.

3.1 Observation with ISIS

High signal-to-noise-ratio spectra (SNR$\sim$100) of 18 targets were obtained using the Intermediate-dispersion Spectrograph and Imaging System (ISIS), through the Isaac Newton Group of Telescopes (ING) program SW2017a08. The aim was to have a set up closely resembling that of the Gaia RVS, which spans the wavelength range between 8450 to 8720 Å, and has a resolution of 11,500. The observations, therefore, used the standard ISIS spectral configuration, and were conducted in the ISIS red arm, which is

optimized for wavelengths similar to those covered by the Gaia RVS. With the R1200R grating, a central wavelength of 8600 Å (which covers the wavelength between 8291 to 8909 Å), and the 0.7 arcseconds slit, the resolution delivered by this set up is 16,600 (an intermediate resolution i.e., R=1800-20000). To minimize read-out noise, we used the default slow read-out mode. The total integration time for the spectra of our 18 targets, under the assumption of an airmass of 1.3 (where 2 would be the maximum), bright time, and seeing of 1 arcsecond, was computed using the exposure time calculator SIGNAL from the ING website, and found to be 1606s. Overheads were accounted for with the aid of the Total Observing Time Estimator (TOTE) tool on the ING website, leading to a total on-target time of 03hr 06mins. To perform telluric correction, 5 telluric standard stars were observed. In order to compute RVs for the 18 targets via cross correlation, 3 RV standards, covering approximately the same spectral type range as the targets, were observed with the same configuration described above. The observation of these 5 telluric standards and 3 RV standards added a total of 01hr 48min of observing time, leading to a total program time of 04hr 54min (or 17,640s). In this thesis, we will discuss only 10 of the 18 objects observed.

3.2 Data reduction

The data were reduced using the Image Reduction and Analysis Facility (IRAF; Tody, 1986). The spectra images were first de-biased and flat-fielded. Then, we extracted the spectra using IRAF *apall* and using a linear fit to estimate the background. Next, we used CuAr and CuNe arc lamps to perform the wavelength calibration of the spectra, and we achieved a typical wavelength calibration precision of ± 0.015 Å. The flux calibration of the spectra was done using the observed telluric standards as reference and using IRAF *sensfunc*. Finally, we performed telluric correction on the observed spectra. First, the telluric standards were continuum-normalized by fitting their observed spectra with a polynomial. Then, we removed hydrogen absorption lines and bad pixels by manually interpolating over them using IRAF *splot*. The resulting telluric correction was applied to the targets, and for each target we used the telluric correction derived from the standard that was observed closest in time and airmass to the target.

3.3 Analysis of the spectra with iSpec

3.3.1 Radial velocity

To determine the RV of our targets, we first analyzed the reduced spectra using iSpec[1] (Blanco-Cuaresma et al., 2014; Blanco-Cuaresma, 2019), which cross-correlates the spectrum of our star with their database of absorption lines. This program, however, does not apply barycentric correction, hence we have used the IDL program *barycorr* from the library EXOFAST[2] to calculate it. The barycentric-corrected RV is computed by *barycorr* using the julian date of the observations, the R.A. and Dec. of the targets, the measured RV, and the coordinates of the observatory.

To examine the quality of our measured RV, we have applied the same method to obtain the RV of the 3 standards, and compared them to the values listed on the Set of Identifications, Measurements and Bibliography for Astronomical Data (SIMBAD). We found a small systematic shift of -0.8 km s^{-1} by taking the difference between the iSpec and the literature RV for all 3 standards, then calculated their weighted mean:

$$\bar{x} = \frac{\sum w_i x_i}{\sum w_i} = \frac{w_1 x_1 + w_2 x_2 + w_3 x_3}{w_1 + w_2 + w_3} \tag{3.1}$$

where x_i are the individual differences and w_i are the individual weights, and $\bar{x}$ is the average systematic shift. The individual weights are just the inverse of the individual RV uncertainties measured with iSpec, i.e. $w_i = 1/\sigma_{i,\mathrm{RV}}$. We applied this systematic shift to all of our measured RVs.

All of the new RV from iSpec have error < 1 km s^{-1} except for TYC 2061-642-1 with error $\sim$6 km s^{-1} because it is an A type star, so it only has a few hydrogen lines, and they are very broad due to the high rotational velocity.

We found that TYC 3161-434-1 is a new double-lined spectroscopic binary. We have measured the RV for both the components of the binary, and we will refer to them as TYC 3161-434-1A and TYC 3161-434-1B.

Using the astrometric information from Gaia DR3 and either the RV measured here or the one from the literature depending on which measurement has the smallest uncertainty, we computed the U, V, and W components of the Galactic velocity as well as the X, Y, Z, Galactic coordinates for our targets. The results are shown in Table 3.1.

[1] `http://www.blancocuaresma.com/s/iSpec`

[2] `http://astroutils.astronomy.ohiostate.edu/exofast/barycorr.html`

Table 3.1: The kinematic information for the objects presented here. UVW are calculated using the Gaia DR3 coordinates, parallax, PM, combined with the value of RV with the smallest uncertainty (see Table 3.2).

Name	U (km s^{-1})	V (km s^{-1})	W (km s^{-1})	X (pc)	Y (pc)	Z (pc)
TYC 3023-1691-1	41.5±0.3	-9.73±0.07	-39.95±0.03	-187±1	-50.4±0.3	184±1
TYC 3024-1493-1	-33.69±0.08	-18.60±0.09	-20.60±0.04	-141.4±0.6	-38.7±0.2	139.4±0.6
TYC 3023-1688-1A	0.38±0.04	-29.0±0.2	18.66±0.05	-156.4±0.7	-42.4±0.2	154.0±0.7
TYC 3023-1688-1B	...	...	...	...	...	...
TYC 3023-1688-1C?	...	...	...	...	...	...
TYC 3440-338-1	75.6±0.1	14.92±0.02	-5.2±0.1	-58.5±0.1	31.00±0.07	85.7±0.2
TYC 3441-520-1	-51.9±0.1	14.08±0.04	2.4±0.2	-58.7±0.1	29.11±0.06	84.7±0.2
TYC 3440-300-1A	0.1±0.2	-11.27±0.08	-6.3±0.2	-61.0±0.1	31.28±0.07	88.7±0.2
TYC 3440-300-1B	...	...	...	...	...	...
TYC 2061-642-1	-24.7±0.1	17.0±0.1	-15.1±0.2	-34.6±0.2	-165.1±0.9	71.3±0.4
TYC 2061-148-1	57.7±0.4	16.2±0.4	-14.2±0.4	-39.20±0.08	-186.8±0.4	80.6±0.2
TYC 2061-270-1	12.7±0.2	-46.5±0.2	6.2±0.2	-34.5±0.1	-163.7±0.6	70.7±0.3
TYC 3160-1812-1	-36.0±0.5	-81.0±0.4	47.9±0.5	63.8±0.8	-81±1	94±1
TYC 3161-177-1	31.83±0.07	-5.1±0.4	-5.73±0.02	61.33±0.08	-76.2±0.1	89.6±0.1
TYC 3161-434-1A	42.7±0.1	-54.7±0.6	-15.51±0.06	68.5±0.2	-84.9±0.2	100.0±0.3
TYC 3161-434-1B	36.6±0.6	-2.3±0.8	-14.3±0.3	66.5±0.9	-82±1	97±1
TYC 3161-434-1C	...	...	...	63.6±0.8	-77±1	100±1

3.3.2 Metallicity

Next, we measure the metallicity of our targets. The four main parameters that determine how deep and wide an absorption line is are: (1) [Fe/H], (2) rotational velocity (v sin i), (3) effective temperature ($T_{\rm eff}$) and (4) surface gravity (log g). Though, unfortunately, there are degeneracies between these parameters, i.e. there are various combinations of stellar parameters that can lead to identical depth and width for a line. To break these degeneracies, we searched the literature for measurements of $T_{\rm eff}$ and log g. Afterward, we used iSpec with the known input value of $T_{\rm eff}$ and log g and a selected line list to determine the [Fe/H] and v sin i of our target spectra.

To ensure the reliability and accuracy of these newly attained values, we have further checked two of the previous results by eye. We first check if the plot of our normalized spectrum is flat or not. If not, then we improve the normalization, e.g. by adjusting the degree of the polynomial used. We next check if the model synthetic spectrum fits well with the spectrum of our target. The two spectra should look similar to each other, i.e. the absorption lines in the resulting model should roughly appear to be as deep and wide as in the observed spectrum. Otherwise, we would enhance the fit via iSpec. This can be achieved by testing the impact of various combinations of codes, models, and line lists as well as with different normalization polynomials.

The different model fitting codes integrated in iSpec are: SPECTRUM (Gray, 1999); Turbospectrum (Plez, 2012); Spectroscopy Made Easy (SME; Valenti & Piskunov, 1996; Piskunov & Valenti, 2017); MOOG (Sneden et al., 2012); Synthe/WIDTH9 (Kurucz, 2005). The spectral synthesis codes have been adapted in iSpec to work with the Model Atmospheres with a Radiative and Convective Scheme (MARCS; Gustafsson et al., 2008) and the ATLAS9 model atmospheres (Kurucz, 2017). iSpec also offers different choices for the line lists to be used with the previously mentioned codes and models. The line lists available are the Gaia-ESO Survey (GES; Jofré et al., 2014) line list and the Vienna Atomic Line Database (VALD; Piskunov et al., 1995).

The procedure described above was calibrated by first applying it to a reference atlas spectrum of the Sun provided by iSpec (Hinkle et al., 2000). Because the atlas spectrum of the Sun has a much higher resolution compared to our ISIS spectra ($\sim$80,000 vs. $\sim$16,600) we first degraded the resolution of the atlas spectrum by convolving it with a gaussian. Then we used a spline to fit and normalize the continuum. Finally, we used combinations of different codes, models, and line lists among the ones provided by iSpec to measure [Fe/H] for the Sun. The input $T_{\rm eff}$ and log g we used were 5777 K

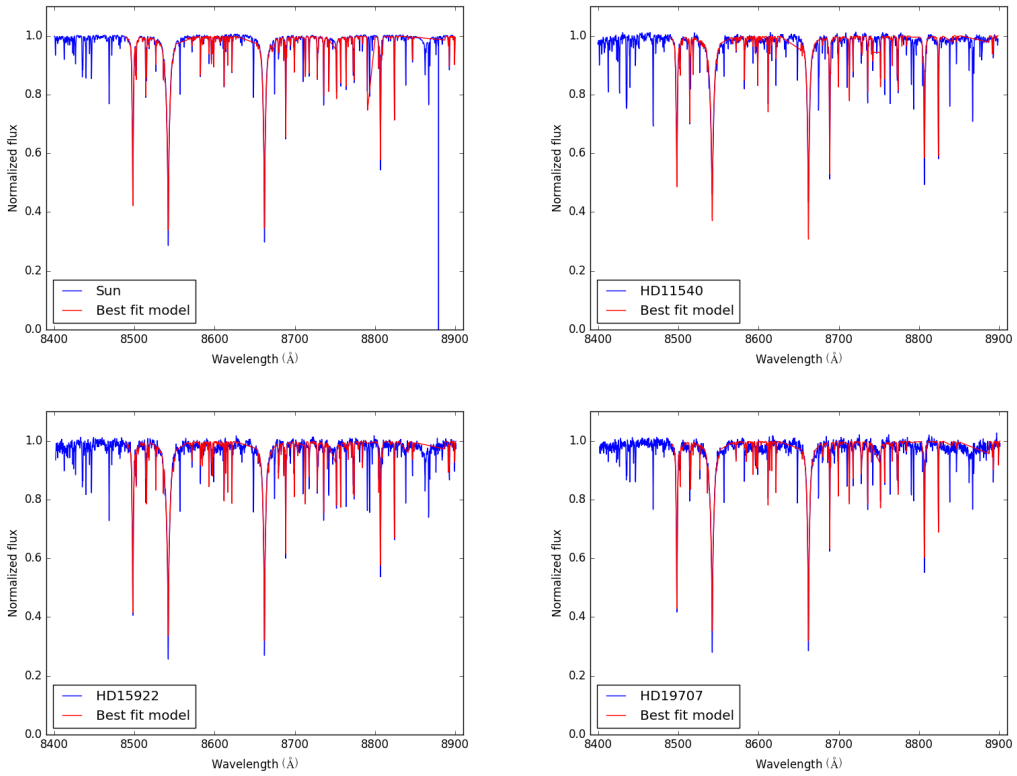

Figure 3.1: *Top left:* The atlas spectrum of the Sun (plotted in blue; Hinkle et al., 2000) and the best fit obtained with iSpec (red). The fit is performed only over certain regions of the spectrum, hence the gaps in the best fit model. For further detail see Section 3.3.2. *Top right:* same as the top left panel, but for HD115404. *Bottom left:* same as the top left panel, but for HD159222. *Bottom right:* same as the top left panel, but for HD1197076.

and 4.44 (Smalley, 2005). We assumed the macroturbulence velocity is 0, and we computed the microturbulence velocity using the GES relation (Jofré et al., 2014), which is included in iSpec. Finally, iSpec only uses [Fe/H] and v sin i as free parameters of the fit, and we set the initial guesses for the fitting procedure to 0 for [Fe/H] and 1.6 km s^{-1} for v sin i (Pavlenko et al., 2012). The limb darkening coefficient is set to 0.6 (Moon et al., 2017). We found that the combination of SME with the ATLAS9 models and the VALD line list gives the [Fe/H] and v sin i results that are closest to 0 and 1.6 km s^{-1}, respectively. So, we used this combination to fit the spectra of all of the rest of our targets. The normalized atlas spectrum of the Sun and the best fit model are shown in the top left panel of Figure 3.1 in blue and red, respectively. The fit is performed only in regions of the spectrum around the lines included in the chosen line list (in this case the VALD list), so the best fit model appears to have gaps.

To validate our results, we applied the method described above to our RV standards, and compared the [Fe/H] and v sin i we obtained with those in the literature. We did two slightly different tests. In one set of tests, we used the literature values of [Fe/H] and v sin i as our initial guess; in the other set of tests, we used [Fe/H] = 0 and v sin i = 1 km s^{-1} as our initial guess. In the first set of tests we find that the [Fe/H] have a systematic offset of 0.13 and a median absolute deviation of 0.03, while the v sin i have a systematic offset of 0.2 km s^{-1} and a median absolute deviation of 1.2 km s^{-1}. In the second set of tests we find that the [Fe/H] have a systematic offset of 0.13 and a slightly larger median absolute deviation of 0.04, while the v sin i have a systematic offset of 0.4 km s^{-1} and a median absolute deviation of 1.4 km s^{-1}. If our target had estimates of [Fe/H] and v sin i in the literature, we used them as initial guesses and we then corrected the measured values with the offsets derived in the first set of tests. We also assumed as our measurement uncertainties the median absolute deviation for the first set of tests. If our target did not have estimates of [Fe/H] and v sin i in the literature, we used 0 and 1 km s^{-1} as initial guesses respectively, and we then corrected the measured values with the offsets derived in the second set of tests. We also assumed as our measurement uncertainties the median absolute deviation from the second set of tests. The best fit models from the first set of tests are shown in the top right, bottom left, and bottom right panels of Figure 3.1. In each panel we show the normalized observed spectrum in blue and the best fit model in red.

The iSpec results and the literature value for all targets are presented in Table 3.2

Table 3.2: The properties of the objects presented here. For each object we give the spectral type, mass, effective temperature ($T_{\rm eff}$), surface gravity ($\log g$), the metallicity ([Fe/H]) from the the literature and the one measured here, the RV from the literature and the one measured here, and the rotational velocity ($v \sin i$) from the literature and measured here. $v \sin i$ values from the literature were published without uncertainties in the original papers. References: 1- Jönsson et al. (2020); 2- Niedzielski et al. (2016); 3- Paegert et al. (2022); 4- Anderson & Francis (2012); 5- Gaia Collaboration et al. (2018b); 6- Glebocki & Gnacinski (2005); 7- Luo et al. (2019); 8- Soubiran et al. (2016b); 9- Gaia Collaboration et al. (2022b).

Name	Sp. T	Mass ($M_\odot$)	$T_{\rm eff}$ (K)	$\log g$ (dex)	ref.	[Fe/H] (dex)	ref.	Our [Fe/H] (dex)	RV (km s^{-1})	ref.	Our RV (km s^{-1})	$v \sin i$ (km s^{-1})	ref.	Our $v \sin i$ (km s^{-1})
TYC 3023-1691-1	F8V	1.02±0.05	5786±120	4.40±0.09	1	-0.20±0.01	1	-0.06±0.03	-43.49±0.02	1	-46.3±0.6	2.92	1	4.2±1.2
TYC 3024-1493-1	F8	1.18±0.05	6069±135	4.30±0.09	1	-0.41±0.02	1	-0.52±0.03	-37.13±0.03	1	-39.7±0.6	4.15	1	0.2±1.2
TYC 3023-1688-1A	F5	1.25±0.05	6114±133	4.24±0.08	1	-0.14±0.01	1	-0.10±0.03	2.39±0.02	1	0.1±0.5	8.48	1	5.4±1.2
TYC 3023-1688-1B	M4.5V	0.15±0.03	...	...	...	...	...	...	...	...	...	...	...	...
TYC 3023-1688-1C?	M1.5V	...	...	...	...	...	...	...	...	...	...	...	...	...
TYC 3440-338-1	K0	1.33±0.05	5502±15	3.90±0.04	2	0.15±0.01	2	...	43.22±0.02	2	...	...	...	...
TYC 3441-520-1	F8	1.33±0.05	6393±113	4.20±0.08	3	-0.29±0.08	4	...	-28.4±0.2	5	...	5.4	6	...
TYC 3440-300-1A	K3	0.78±0.05	4802±26	4.59±0.04	7	0.03±0.02	7	-0.19±0.03	-7.6±0.5	5	-9.5±0.3	...	...	0.2±1.2
TYC 3440-300-1B	M3.5V	...	...	...	...	...	...	...	...	...	...	...	...	...
TYC 2061-642-1	A2	2.15±0.05	7360±175	4.1±0.2	8	-0.3±0.1	8	-0.31±0.03	0.9±0.2	1	41.3±6.1	85.72	1	67.2±1.2
TYC 2061-148-1	G5V	0.87±0.05	5614±3	4.491±0.002	9	-0.2±0.2	9	0.02±0.03	-49.1±0.7	5	-50.1±0.8	...	...	4.0±1.2
TYC 2061-270-1	G8IV	0.90±0.05	5376±7	4.44±0.01	9	0.5±0.2	9	0.51±0.03	-45.5±0.5	5	-48.6±0.3	...	...	0.2±1.2
TYC 3160-1812-1	F5	1.14±0.05	6496±20	4.18±0.02	9	-1.2±0.2	9	-0.71±0.03	-87.3±0.4	9	-89.6±0.7	...	...	4.5±1.2
TYC 3161-177-1	F8	1.14±0.05	6004±8	4.250±0.004	9	0.1±0.2	9	0.17±0.03	-24.2±0.4	5	-25.9±0.5	...	...	3.5±1.2
TYC 3161-434-1A	K3	0.82±0.05	4822±22	4.71±0.04	7	-0.47±0.02	7	-0.72±0.03	-60±3	7	41.3±6.1	...	...	16.7±1.2
TYC 3161-434-1B	M2.5V	1.20±0.03	...	...	...	...	...	...	...	...	-22.2±0.8	...	...	...
TYC 3161-434-1C	M4.5V	0.19±0.03	3319±10	5.04±0.04	9	-0.62±0.2	9	...	...	...	...	...	...	...

3.4 Discussion of individual systems

3.4.1 TYC 3023-1691-1, TYC 3024-1493-1, TYC 3023-1688-1ABC?

TYC 3023-1691-1 is an F8V (Pickles & Depagne, 2010). We measure a metallicity of [Fe/H] = -0.06 ± 0.03, which is similar to TYC 3023-1688-1A and about $8\times$ higher than TYC 3024-1493-1 (see below). Its RV is -43.49 ± 0.02 km s^{-1} (Jönsson et al., 2020). It has a probability of 91% to belong to the thin disk. The probability was calculated by first computing the UVW velocity for our targets using the Gaia PM, parallax (Gaia Collaboration et al., 2021) and RV (Gaia Collaboration et al., 2018a), and then assuming that the three components of the Galaxy (i.e. thin disk, thick disk, and halo) have gaussian UVW velocity distributions. The σ of the three distributions was taken from (Bensby et al., 2003). The probability to belong to each of the three components is then calculated as follows:

$$k_i = \frac{1}{(2\pi)^{3/2}\sigma_{Ui}\sigma_{Vi}\sigma_{Wi}} \tag{3.2}$$

$$f(U,V,W)_i = k_i\, exp\left(-\frac{U^2}{2\sigma_{Ui}^2} - \frac{(V - V_{asym_i})^2}{2\sigma_{Vi}^2} - \frac{W^2}{2\sigma_{Wi}^2}\right) \tag{3.3}$$

$$Prob_i = \frac{X_i\, f_i}{X_{\rm thin}\, f_{\rm thin} + X_{\rm thick}\, f_{\rm thick} + X_{\rm halo}\, f_{\rm halo}} \tag{3.4}$$

where the subscript i indicates either the thin disk, thick disk, or halo, σ_{Ui}, σ_{Vi}, and σ_{Wi} are the velocity dispersion for each component of the Galaxy from Bensby et al. (2003), and V_{asym_i} is the asymmetric velocity drift for the same component, also taken from Bensby et al. (2003), and X_i is the fraction of stars belonging to each component as estimated from the Solar neighborhood population (also taken from Bensby et al., 2003). The assumption that the UVW distributions are Gaussian is an approximation. For example we could model the thin disk distribution better using a combination of several Gaussian components with dispersion that depends on the age (as it is done for example in the Gaia Universe Model Snapshot; Robin et al. 2012). However, we believe that our approximation causes only small underestimations of the probability of an object to belong to the thin disk.

TYC 3024-1493-1 is also an F8 (Roeser & Bastian, 1988) with a low metallicity of [Fe/H] = = -0.52 ± 0.03 as measured by us, and an RV = -37.13 ± 0.03 km s^{-1} as measured by Jönsson et al. (2020). It has a probability of 98% to belong to the thin disk.

TYC 3023-1688-1A is the most massive star in this system, classified as F5 (Roeser & Bastian, 1988). We measured its metallicity and found it to be [Fe/H] = -0.10 ± 0.03, while Jönsson et al. (2020) measured it RV and found it to be RV = 2.39 ± 0.02 km s^{-1}. It has a probability of 98% to belong to the thin disk. TYC 3023-1688-1A is also part of the SUPERWIDE catalog (Hartman & Lépine, 2020), where it is listed as object SWB73753. Its companion, which we call TYC 3023-1688-1B, has a spectral type of M4.5V, which we have estimated using the Gaia *G* magnitude, the Gaia parallax, and Table 5 from Pecaut & Mamajek (2013). No [Fe/H] or RV measurement is available for this object. Finally, while inspecting the images for TYC 3023-1688-1A using ALADIN, we found that it is resolved by Gaia in two objects. Gaia does not provide parallax or PM measurements for this new object, so we cannot verify if it is a new companion to the TYC 3023-1688-1AB system, or simply a background object that happens to be close to TYC 3023-1688-1A. We call the new object TYC 3023-1688-1C?, and we estimate its spectral type to be M1.5V by using the Gaia *G* magnitude, Table 5 from Pecaut & Mamajek (2013), and assuming that it is at the same distance as TYC 3023-1688-1A. We have checked if TYC 3023-1688-1A appears as a double line spectroscopic binary in the medium resolution spectroscopy of ISIS, but we do not find any evidence for it. This could mean either that TYC 3023-1688-1C? is a background object, or that the binary has a relatively low orbital velocity given its separation. We checked TYC 3023-1691-1, TYC 3024-1493-1, TYC 3023-1688-1A using BANYAN (Gagné et al., 2018) and found that they all have a probability of 99.9% to be field objects.

TYC 3023-1691-1, TYC 3024-1493-1, and TYC 3023-1688-1A all have [Fe/H] measurements from APOGEE-2 DR16 (Jönsson et al., 2020), and although the [Fe/H] of APOGEE-2 DR16 have slightly smaller uncertainties, we decided to use our measurements of [Fe/H] to avoid possible systematic errors due to the use of different models, line lists, and fitting codes. Also, since the metallicities in APOGEE-2 are measured using H-band spectra, this could introduce additional systematic uncertainties because of the use of NIR spectra in comparison to our optical spectra. By using ISIS [Fe/H] whenever available, we have a more homogeneous set of measurements. For RV on the other hand, since they are more simple measurements based only on cross-correlation of the spectra with a template, we think it is unlikely that there are large systematics between different surveys, so we adopt whatever measurements have the smallest uncertainties. The best fit models obtained with iSpec for all three objects are shown in Figure 3.2. In each panel, the spectrum of the target is shown in blue and the best fit model is shown in red.

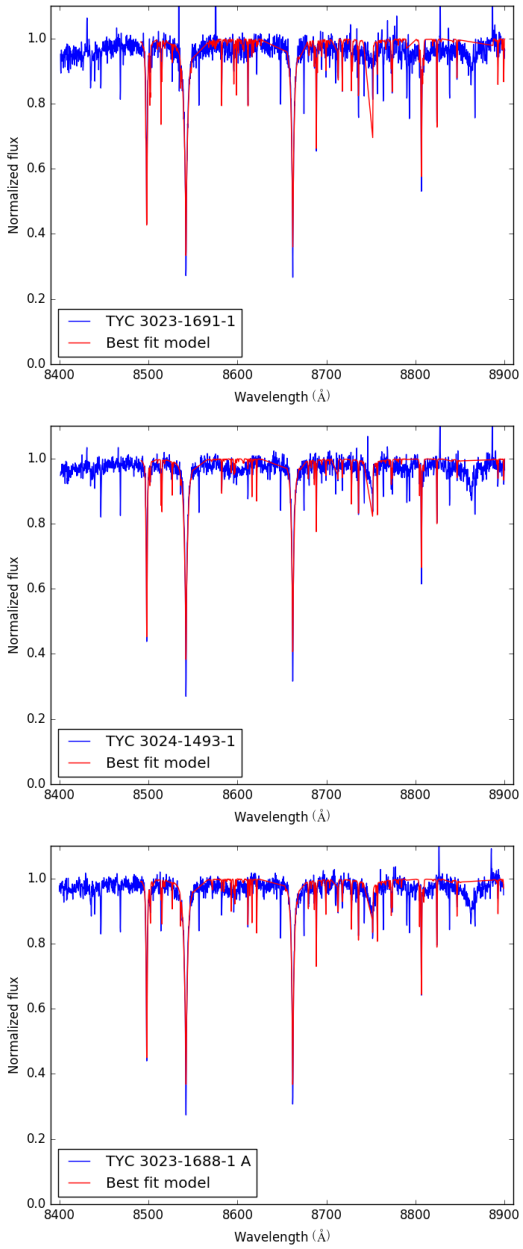

Figure 3.2: *Top panel:* The normalized spectrum of TYC 3023-1691-1 (blue) and the best fit model obtained with iSpec (red). *Middle panel:* The normalized spectrum of TYC 3024-1493-1 (blue) and the best fit model obtained with iSpec (red). *Bottom panel:* The normalized spectrum of TYC 3023-1688-1 A (blue) and the best fit model obtained with iSpec (red).

TYC 3024-1493-1 could be the cause of the disintegration of the TYC 3023-1691-1 + TYC 3023-1688-1AB (and C?) system. It has quite a different [Fe/H] from them, about 5-8$\times$ lower, while TYC 3023-1691-1 and TYC 3023-1688-1A have [Fe/H] consistent with each other. TYC 3024-1493-1 could have broken up the possible triple (quadruple) system composed of TYC 3023-1691-1 and TYC 3023-1688-1ABC? while passing between them. The new direction of motion of TYC 3023-1691-1 and TYC 3023-1688-1AB are quite different from each other, so TYC 3023-1691-1 or TYC 3023-1688-1AB (or both) would have changed their path violently. The top panel of Figure 3.3 supports this explanation. We can see from the top and middle panel that TYC 3024-1493-1 passed between TYC 3023-1688-1A and B or passed by them if the orbital motion is causing the position of TYC 3023-1688-1B to be a little bit inaccurate. This interaction causes the disintegration of the triple system. Furthermore, the bottom panel of Figure 3.3 also shows that the interaction between TYC 3024-1493-1 and TYC 3023-1688-1A (i.e., the dark green parabola) happens at the same time as all of the others (except the dark grey parabola), so the triple system of TYC 3023-1691-1 and TYC 3023-1688-1AB begins to break when this interaction occurs. Note that the parabola between TYC 3023-1691-1 and TYC 3024-1493-1 is much narrower than the parabola between TYC 3023-1691-1 and TYC 3023-1688-1A and B even though the separation between TYC 3023-1691-1 and TYC 3024-1493-1 is much larger than the separation between TYC 3023-1691-1 and TYC 3023-1688-1A and B. This is due to the high PM of both TYC 3023-1691-1 and TYC 3024-1493-1 as well as the direction of their relative path.

3.4.2 TYC 3440-338-1, TYC 3441-520-1, TYC 3440-300-1AB

TYC 3440-338-1 is a K0 (Roeser & Bastian, 1988). It has a metallicity of 0.15 ± 0.01 and an RV of 43.22 ± 0.02 km s^{-1} (both taken from Niedzielski et al., 2016). This object is in the Catalog of Accelerations (Brandt, 2021), which means it could be an unresolved binary. However, the RV has relatively small errors, which could be due to the fact that the orbit of the companion is perpendicular to the line of sight, so the contribution of the orbital velocity to the RV is relatively small. We find that it has a probability of 96% to belong to the thin disk. TYC 3441-520-1 is an F8 according to Roeser & Bastian (1988). The metallicity of this object is -0.29 ± 0.08 (Anderson & Francis, 2012) and the RV is -28.4 ± 0.2 km s^{-1} (Gaia Collaboration et al., 2018a). Similarly to TYC 3440-338-1, TYC 3441-520-1 is also in the Catalog of Accelerations, so it could also be an

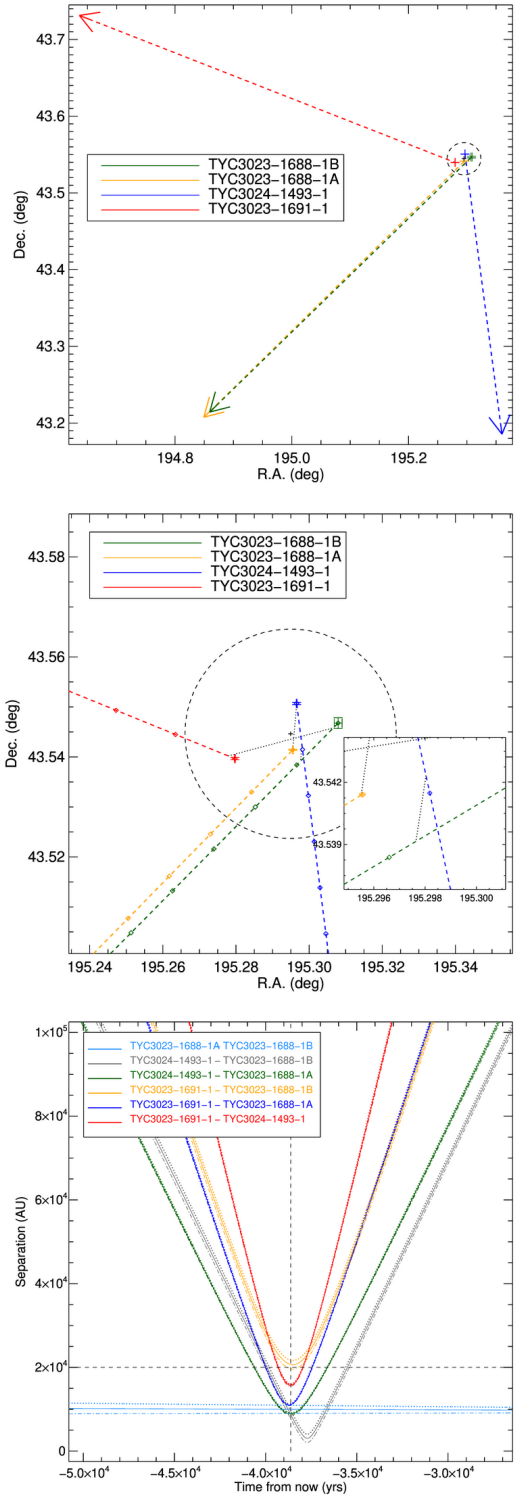

Figure 3.3: *Top panel:* The position of TYC 3023-1691-1, TYC 3024-1493-1, and TYC 3023-1688-1AB now and at the time of closest encounter of the system. For each object, the arrow indicates the current direction of motion, the dashed line connects the current position with the position at the time of closest encounter, marked by a cross. The small black cross is the centre of the system at the time of closest encounter, and the black dashed circle has a radius of 20,000 AU. TYC 3024-1493-1 passes between the other three objects, likely causing their disintegration. *Middle panel:* Same as the top panel, but zoomed in on the position of closest encounter. Symbols and colours are the same as the top panel, and we added diamonds to show the position of each object in intervals of 1,000 years after the time of closest encounter, up to a maximum of 10,000 years. For pairs of objects that reach their mutual minimum separation after the time of closest encounter for the system, a dark grey dotted line shows the position and the time when their interaction took place. TYC 3024-1493-1 (blue dashed line) is likely causing the disintegration of TYC 3023-1691-1 (red dashed line) and TYC 3023-1688-1 (orange and dark green dashed lines) by first interacting with TYC 3023-1691-1 while at their minimum separation, then with TYC 3023-1688-1A right after the time of closest encounter of the system, and last with TYC 3023-1688-1B approximately 1000 years after the time of closest encounter of the system. TYC 3023-1688-1AB remained a bound binary system throughout the whole interaction. *Bottom panel:* The separation between the components of the system as a function of time. The vertical dashed line marks the time of closest encounter while the horizontal dashed line indicates a separation of 20,000 AU. The dotted and dash-dotted lines above and below each parabola indicate the one-sigma uncertainty range. The separation between TYC 3023-1688-1A and TYC 3023-1688-1B is practically constant, i.e., the dodger blue parabola is flat, because TYC 3023-1688-1A and TYC 3023-1688-1B are still a binary. The interaction between TYC 3024-1493-1 and TYC 3023-1688-1A (i.e., the dark green parabola) reaches the minimum at the same time as all the others, and it is the lowest of all of the parabola (except the dark grey one). This indicates that the interaction between TYC 3024-1493-1 and TYC 3023-1688-1A is the one starting the breakup of the TYC 3023-1691-1 + TYC 3023-1688-1AB system. The interaction between TYC 3024-1493-1 and TYC 3023-1688-1B happened about 1000 years later. This could be due to the effect of the orbital motion of TYC 3023-1688-1B around TYC 3023-1688-1A causing the position of TYC 3023-1688-1B at the time of closest encounter to be slightly offset.

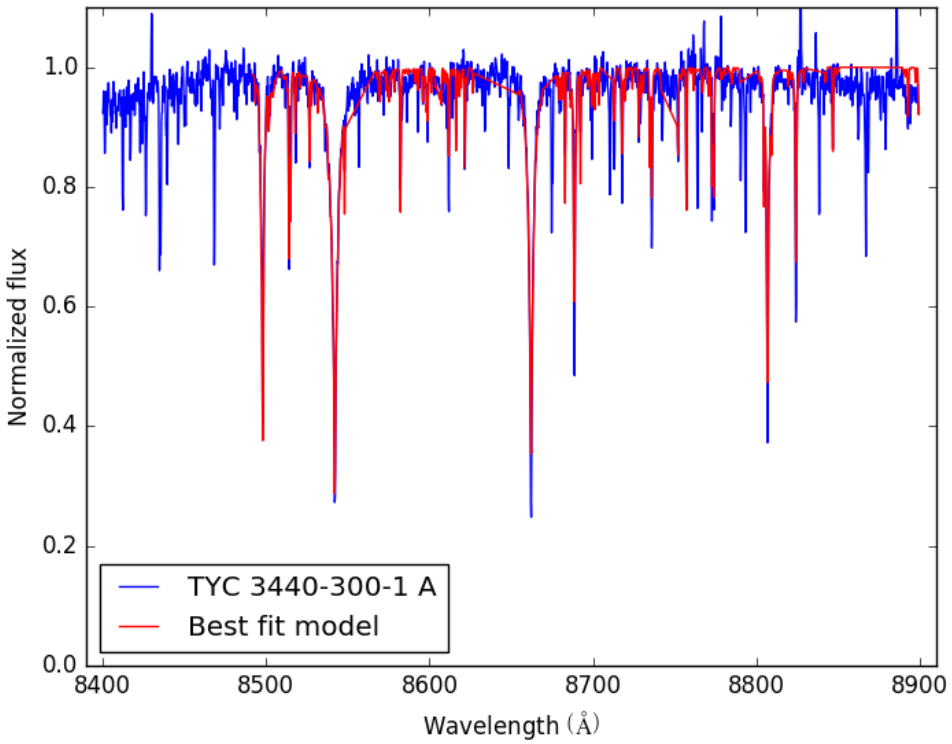

Figure 3.4: The normalized spectrum of TYC 3440-300-1 A (blue) and the best fit model obtained with iSpec (red).

unresolved binary. Also in this case, the RV has relatively small errors, which could mean once again that the orbital plane of the binary is perpendicular to the line of sight. It has a probability of 99% to belong to the thin disk. Finally, TYC 3440-300-1A is a K3 (Xiang et al., 2019). Using the ISIS spectrum, we measure a metallicity of -0.19 ± 0.03 and a RV of -9.5 ± 0.3 km s^{-1}. The best fit model is shown in Figure 3.4. Gaia resolves a companion to this star, which we will call TYC 3440-300-1B. We estimate the spectral type for this new object using the Gaia G magnitude, parallax, and Table 5 from Pecaut & Mamajek (2013) and find it to be M3.5V. No metallicity nor RV measurement is available for this new object. TYC 3440-300-1A and B both have a probability of 99% to belong to the thin disk. Using BANYAN, we have established that all objects in this system have a probability of 99.9% to be field objects.

TYC 3440-338-1 could be the cause of the disintegration of the TYC 3441-520-1 + TYC 3440-300-1AB system. It has quite a different [Fe/H] compared to them, so we can say with confidence that it was previously not associated with the system. We do,

however, note that both TYC 3440-338-1 and TYC 3441-520-1 are in the Catalog of Accelerations, so their metallicity could be a bit biased if the spectral absorption lines by the unresolved companion contaminate the spectrum of the primary. TYC 3440-338-1 could have broken up the triple (quadruple) by first interacting weakly with TYC 3441-520-1 and then more strongly with TYC 3440-300-1A and B. The TYC 3440-338-1–TYC 3441-520-1 interaction first weakened the gravitational attraction between TYC 3441-520-1 and TYC 3440-300-1AB, then the interaction between TYC 3440-338-1 and TYC 3440-300-1AB causes the breakup to become more violent, i.e. TYC 3440-300-1A and B were really diverted off their original path, away from TYC 3441-520-1. Figure 3.5 shows this possible interaction. We can see from the top and middle panels that TYC 3440-338-1 appears very close to TYC 3440-300-1AB at the time of closest encounter of the system, although this plot does not show the previous interaction between TYC 3440-338-1 and TYC 3441-520-1 which is when the disintegration of the system began. Furthermore, the bottom panel of Figure 3.5 also shows that the initial interaction between TYC 3440-338-1 and TYC 3441-520-1 (i.e., the red parabola) happens a bit before the interaction between TYC 3440-338-1 and TYC 3440-300-1A (i.e., the blue parabola) and TYC 3440-338-1 and TYC 3440-300-1B (i.e., the orange parabola). However, the minimum separation between TYC 3440-338-1 and TYC 3440-300-1A and between TYC 3440-338-1 and TYC 3440-300-1B is much smaller than between TYC 3440-338-1 and TYC 3441-520-1 in comparison. This supports the hypothesis of the two-part disintegration, i.e. the weakening of the system via the initial interaction between TYC 3440-338-1 and TYC 3441-520-1, followed by a more violent breakup of the system caused by the very close interaction between TYC 3440-338-1 and TYC 3440-300-1AB. The bottom panel of Figure 3.5 also shows that the parabola between TYC 3440-338-1 and TYC 3441-520-1 is much narrower than the parabola between TYC 3440-338-1 and TYC 3440-300-1A and B, even though the separation between TYC 3440-338-1 and TYC 3441-520-1 is much larger than between TYC 3440-338-1 and TYC 3440-300-1A and B. This is due to the very high PM of TYC 3440-338-1 rather than an indication of a violent break up between them as between TYC 3440-338-1 and TYC 3440-300-1A and B.

3.4.3 TYC 2061-642-1, TYC 2061-148-1, TYC 2061-270-1

TYC 2061-642-1 is an A2 star (Roeser & Bastian, 1988). We measured the metallicity and RV for this object using our ISIS spectra, and find the metallicity to be [Fe/H]

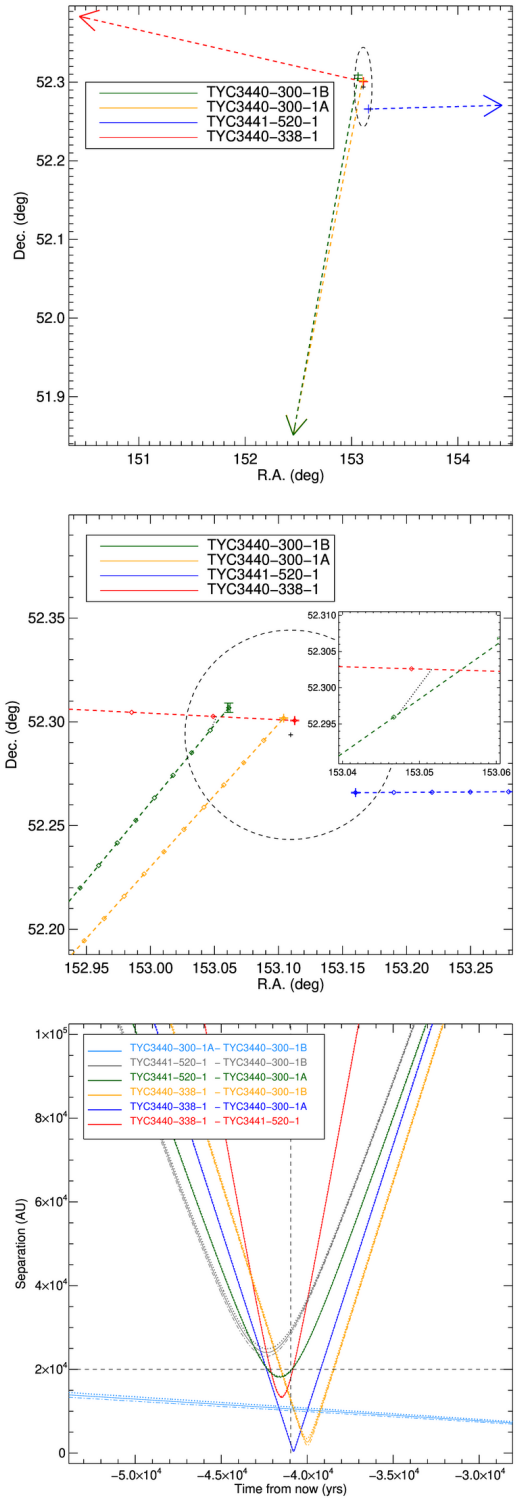

Figure 3.5: *Top panel:* Same as the top panel of Figure 3.3, but for the system consisting of TYC 3440-338-1, TYC 3441-520-1, and TYC 3440-300-1AB. We can see that TYC 3440-338-1 passes between TYC 3441-520-1 and TYC 3440-300-1AB, hence it is likely the cause of the disintegration. *Middle panel:* Same as the middle panel of Figure 3.3, but for the system consisting of TYC 3440-338-1, TYC 3441-520-1, and TYC 3440-300-1AB. All objects in this system have their initial interaction at the time of closest encounter of the system (marked by a cross) or before, except for TYC 3440-338-1 and TYC 3440-300-1B that have their initial interaction ∼1000 years after the system closest encounter. This discrepancy could be due to unaccounted orbital motion of TYC 3440-300-1B leading to a offset in the calculated position. As shown in the top panel, TYC 3440-338-1 (the red dashed line) passes between TYC 3441-520-1 (the blue dashed line) and TYC 3440-300-1A (the orange dashed line). Although it is not shown on the plot, the initial interaction between TYC 3440-338-1 and TYC 3441-520-1 happens before TYC 3440-338-1 interacts with TYC 3440-300-1A, hence the system first got their gravitational attraction weakened, then followed with a relative violent breakup caused by the further interaction of TYC 3440-338-1 with TYC 3440-300-1AB. *Bottom panel:* Same as the bottom panel of Figure 3.3, but for the system consisting of TYC 3440-338-1, TYC 3441-520-1, and TYC 3440-300-1AB. The separation between TYC 3440-300-1A and B is practically constant, i.e. the dodger blue parabola is flat, because TYC 3440-300-1AB are still a binary. The shallow slope is due to the orbital motion. TYC 3440-338-1 has a close encounter with TYC 3441-520-1 first (red parabola), causing the disintegration of the system. Later on TYC 3440-338-1 has a very close encounter with TYC 3440-300-1AB. The interaction between TYC 3440-338-1 and TYC 3440-300-1AB is much stronger than the one between TYC 3440-338-1 and TYC 3441-520-1 i.e., the blue and orange parabola are much lower than the red parabola. Even though the interaction between TYC 3441-520-1 and TYC 3440-300-1AB (i.e. the dark green and grey parabola) happens roughly at the same time as the close encounter between TYC 3440-338-1 and the other three objects, they remain at larger separations, so we believe that it is TYC 3440-338-1 that causes the disintegration of the system. TYC 3441-520-1 and TYC 3440-300-1AB appear to be disintegrating before the close encounter with TYC 3440-338-1. However, this could be due to unaccounted orbital motion, since both TYC 3440-338-1 and TYC 3441-520-1 are in the Catalog of Acceleration.

= -0.31 ± 0.03 and the RV to be 41.3 ± 6.1 km s^{-1}. The best fit model is shown in the top panel of Figure 3.6. The large uncertainty on the RV can be explained by two factors. The first factor is the fact that this object is an A-type star, and these stars typically only have strong hydrogen absorption lines which are very broad to begin with, plus they are further broadened by the fact that A-type stars are fast rotators, leading to rotational broadening of the lines. This can be clearly seen in Figure 3.6, where there are very few lines and they have very broad wings. The second factor is that this star is in the Catalog of Accelerations, which indicates that it could be a binary star. Binarity can lead to broadening of the absorption lines, contributing to the RV uncertainty, particularly if the orbit of the binary is closely aligned with the line of sight. APOGEE-2 DR16 (Jönsson et al., 2020) reports a very different RV measurement for this star (RV = 0.9 ± 0.2 km s^{-1}), but since APOGEE-2 is mostly focused on the measurement of spectra of red giants, we believe our measurement is more reliable. We find this star as a probability of 94% to belong to the thin disk, and using BANYAN we find it has a probability of 99.9% to belong to the field. TYC 2061-148-1 is a G5V star (Pickles & Depagne, 2010). With our ISIS spectrum we measure [Fe/H] = 0.02 ± 0.03 and RV = -50.1 ± 0.8 km s^{-1}. The best fit models is shown in the middle panel of Figure 3.6. This object has measured RV from Gaia DR2, which is RV = -49.1 ± 0.7 km s^{-1}, and since it has slightly smaller uncertainty than our measurement we will use the Gaia value for the rest of the analysis. We calculate a probability of 97% to belong to the thin disk, and using BANYAN we find a probability of 99.9% to belong to the field. TYC 2061-270-1 is a G8IV star (Pickles & Depagne, 2010). Using the ISIS spectrum, we measure [Fe/H] = 0.51 ± 0.03 and RV = -48.6 ± 0.3 km s^{-1}. The best fit models is shown in the bottom panel of Figure 3.6. Gaia DR2 also reports a RV which is consistent with our measurement but has slightly larger uncertainties (-45.5 ± 0.5 km s^{-1}), so we use our measurement in the rest of this work. We find this object has a probability of 97% of belonging to the thin disk and using BANYAN we find it has a probability of 99.9% of belonging to the field.

Our measurements show that all objects have very different [Fe/H] to each other, so they are highly unlikely to have been associated in the past, which in turn means that this system is just a chance alignment. The top and middle panels of Figure 3.7 show all objects moving away from each other, each at a large angle from the other two objects, which further reinforces the hypothesis that this is a chance alignment. Moreover, the bottom panel of Figure 3.7 also shows no strong indication that these objects were disintegrating from each other. Overall, this signals that TYC 2061-642-1,

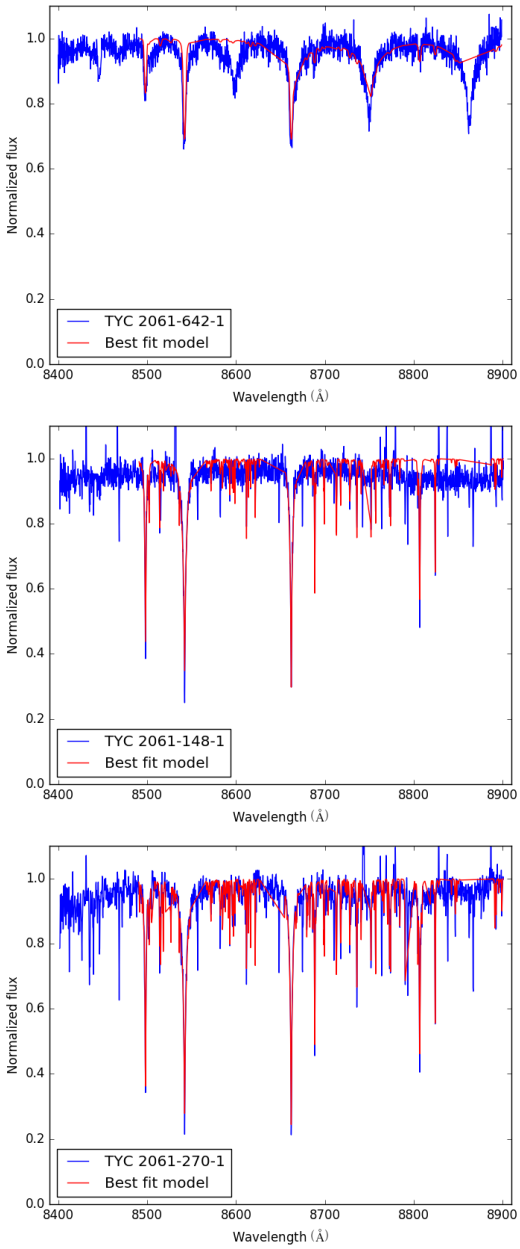

Figure 3.6: *Top panel:* The normalized spectrum of TYC 2061-642-1 (blue) and the best fit model obtained with iSpec (red). This is an A-type star, and we can see clearly that there are only few absorption lines that have very broad wings due to rotational broadening. *Middle panel:* The normalized spectrum of TYC 2061-148-1 (blue) and the best fit model obtained with iSpec (red). *Bottom panel:* The normalized spectrum of TYC 2061-270-1 (blue) and the best fit model obtained with iSpec (red).

TYC 2061-148-1, TYC 2061-270-1 were not a system to begin with and while it is possible that the interaction causes a minor change of path for some of the stars involved, this is not a disintegration. Note that even though this is likely not a disintegrating system, however, given TYC 2061-642-1 and TYC 2061-148-1 came quite close to each other, if there are any planets and/or BDs orbiting either of those stars, their orbits could be disrupted and they could get ejected. Since TYC 2061-642-1 is in the Catalog of Acceleration, it is likely to be an unresolved binary and/or have a brown dwarf or exoplanet companion that survived the close encounter with TYC 2061-148-1. However, TYC 2061-642-1 could also have had additional companions that were ejected. Whereas TYC 2061-148-1 is not in the Catalog of Acceleration, i.e., it is currently a single star, but maybe it had one or more companions that were ejected (planets and/or BDs). Given the literature data we have is not deep enough to see these possible companions, thus deeper observations are essential, e.g., with the James Webb Space Telescope (JWST; Gardner et al., 2006).

3.4.4 TYC 3160-1812-1, TYC 3161-177-1, TYC 3161-434-1ABC

TYC 3160-1812-1 is an F5 (Roeser & Bastian, 1988). Using the ISIS spectrum, we measure both metallicity and RV for this object and we find [Fe/H]$= -0.71 \pm 0.03$ and RV$= -89.6 \pm 0.7$ km s^{-1}. The best fit model can be seen in the top panel of Figure 3.8. The probability for this object to be part of the thick disk is 98%, which is consistent with its slightly low metallicity, and using BANYAN we find a probability of 99.9% to be a field object. TYC 3161-177-1 is an F8 (Roeser & Bastian, 1988), and using the ISIS spectrum we measure a metallicity of 0.17 ± 0.03 and an RV of -25.9 ± 0.5 km s^{-1}. The best fit model can be seen in the middle panel of Figure 3.8. However, Gaia DR2 reports an RV which is consistent with our measurements but with smaller uncertainties, so we use the Gaia DR2 value in our analysis. The Gaia DR2 RV is -24.2 ± 0.4 km s^{-1}. We compute a probability of 99% for this object to belong to the thin disk, and BANYAN gives a probability of 99.9% to be a field object. TYC 3161-434-1A is a K3V (Xiang et al., 2019), and using the ISIS spectrum we measure a metallicity [Fe/H]$= -0.72 \pm 0.03$, which is almost identical to that of TYC 3160-1812-1. The best fit model can be seen in the bottom panel of Figure 3.8. The RV measurement, also obtained from the ISIS spectrum, is RV$= -75.0 \pm 0.6$ km s^{-1}. It has a probability of 88% to be part of the thin disk and 12% to be part of the thick disk and, according to

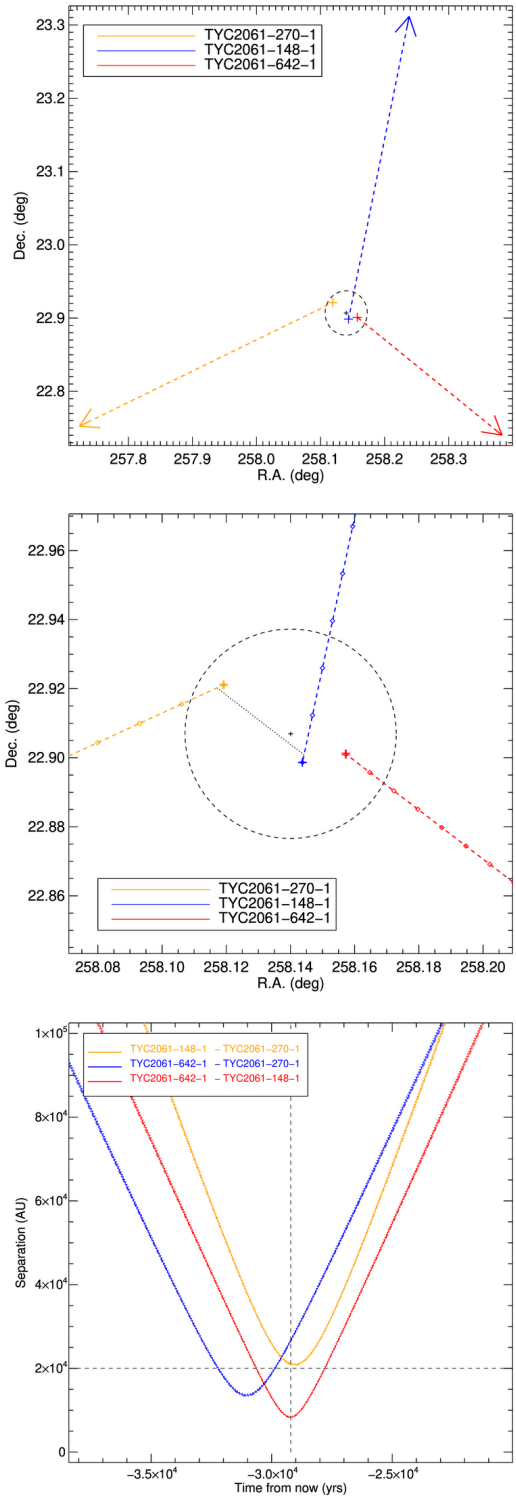

Figure 3.7: *Top panel:* Same as the top panel of Figure 3.3 but for the system consisting of TYC 2061-642-1, TYC 2061-148-1, and TYC 2061-270-1. We can see that the three stars are all moving away from each other, each at a wide angle from the other two objects, so we suspect this is likely to just be a chance alignment. *Middle panel:* Same as the middle panel of Figure 3.3 but for the system consisting of TYC 2061-642-1, TYC 2061-148-1, and TYC 2061-270-1. Although the position of the objects prior to the time of close encounter is not shown on the plot, by tracing their current path backwards, it is clear that TYC 2061-642-1 and TYC 2061-270-1 were closer to each other before the time of closest encounter, while TYC 2061-148-1 was further away. Hence, the first interaction of these 3 objects takes place between TYC 2061-642-1 (i.e., red dashed line) and TYC 2061-270-1 (i.e., orange dashed line), then TYC 2061-642-1 interacts with TYC 2061-148-1 (i.e., blue dashed line) at the time of closest encounter, and lastly TYC 2061-148-1 interacts with TYC 2061-270-1 not long after the time of closest encounter. This indicates that TYC 2061-642-1, TYC 2061-148-1, and TYC 2061-270-1 were likely not a system to begin with, and even though it is possible that the interaction causes a change of path for some of the objects, this is not a disintegrating system. *Bottom panel:* Same as the bottom panel of Figure 3.3 but for the system consisting of TYC 2061-642-1, TYC 2061-148-1, and TYC 2061-270-1. There is no indication of any disintegration events taking place and so it is likely for this system to just be a case of chance alignment.

BANYAN, 99.9% of being a field object. This object is a spectroscopic binary, and Gaia resolves the two components. The previously unresolved companion, TYC 3161-434-1B, is an M2.5V based on its Gaia G magnitude and parallax and using Table 5 from Pecaut & Mamajek (2013). We can extract the spectra of the two separate components from the ISIS spectrum, and we measured an RV of -22.2 ± 0.8 km s^{-1}. This value is very different from the RV of the primary, but we believe this is because of the orbital velocity of the companion around the primary. We cannot measure [Fe/H] for this object even though we have a spectrum for it, because iSpec and the models included with iSpec can only be used to fit K-type or warmer stars (i.e. $T_{\rm eff} > 3600$K). Moreover, TYC 3161-434-1A is also in the SUPERWIDE catalog with the name SWB100302. Its companion is an M4.5V based on its Gaia G magnitude and parallax, and using as usual Table 5 from Pecaut & Mamajek (2013). We do not have an ISIS spectrum for the C component of the system, and we did not find RV measurements from the literature. Gaia DR2 gives a metallicity for this object which is [Fe/H]$= -0.6 \pm 0.2$, which is consistent with the metallicity we measure for the primary.

This is a very puzzling system. If solely looking at the [Fe/H], one would think that TYC 3161-177-1 might be the cause for the disintegration of the TYC 3160-1812-1 + TYC 3161-434-1ABC system. However, the top and middle panels of Figure 3.9 suggest that TYC 3160-1812-1 could be the cause of the disintegration of the TYC 3161-177-1 + TYC 3161-434-1ABC system. Although TYC 3160-1812-1 has almost identical [Fe/H] as TYC 3161-434-1A, but the PM of the two objects is in almost opposite directions, which is impossible for a disintegrating multiple system, because it implies a change of path too big for massive stars such as an F5 or a binary K3V + M2.5V. So it could just be a chance alignment between objects that also happen to have a very similar [Fe/H]. The same goes for object TYC 3161-177-1, although its PM is relatively similar to the TYC 3161-434-1ABC system, therefore suggestive of a gentle breakup, its [Fe/H] is completely different, so it is safe to say that this is also just a chance alignment. Looking at the bottom panel of Figure 3.9, we can see that TYC 3161-177-1 first interacts with TYC 3161-434-1C (i.e., the lime green parabola) approximately 6000 years prior to the closest encounter with the rest of the system. However, the minimum separation between them is large, so even though both of them are high-PM objects, this is likely to be just a very gentle dynamical interaction, thus no disintegration occurs in the TYC 3161-434-1ABC system. The next encounter happened between TYC 3160-1812-1 and TYC 3161-434-1C (i.e., the dark green parabola), not too long before the overall system's closest encounter. TYC 3161-177-1 and TYC 3161-434-1AB

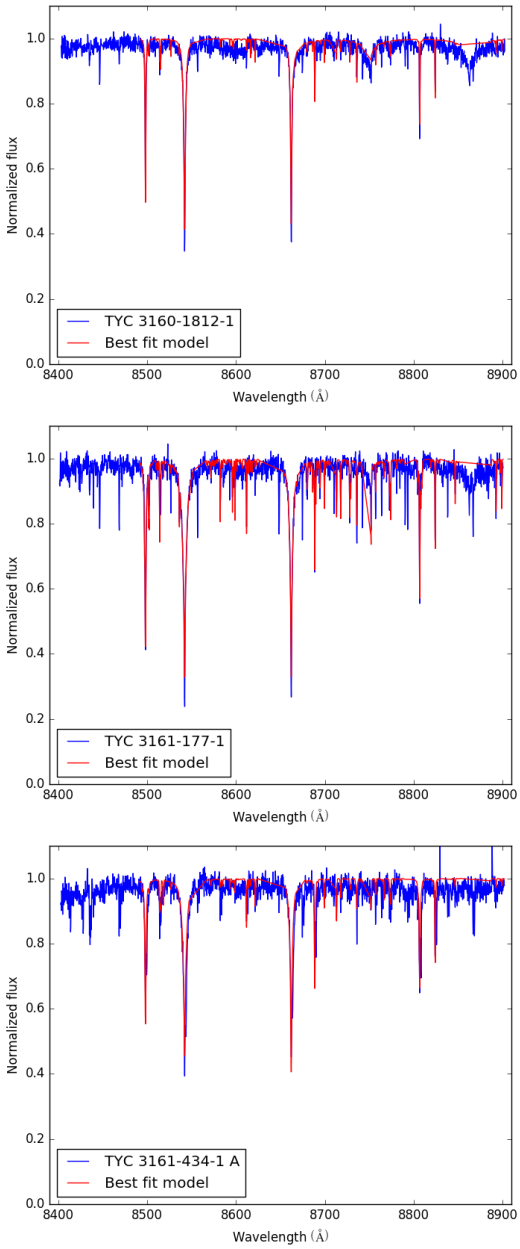

Figure 3.8: *Top panel:* The normalized spectrum of TYC 3160-1812-1 (blue) and the best fit model obtained with iSpec (red). *Middle panel:* The normalized spectrum of TYC 3161-177-1 (blue) and the best fit model obtained with iSpec (red). *Bottom panel:* The normalized spectrum of TYC 3161-434-1 A (blue) and the best fit model obtained with iSpec (red).

(i.e., the dark grey and the dodger blue parabola) also interact at very similar times. The minimum separation between TYC 3161-177-1 and TYC 3161-434-1AB was much smaller in comparison to TYC 3161-177-1 and TYC 3161-434-1C. However, given that TYC 3161-434-1AB is a tight binary, their interaction with TYC 3161-177-1 was just as minor as the one described above. The close encounter between TYC 3160-1812-1 and TYC 3161-434-1A (i.e., the blue parabola) happened literally just before the closest encounter of the overall system. This should also be the same for TYC 3160-1812-1 and TYC 3161-434-1B (i.e., the orange parabola), but it is, however, a little bit later because of the effect of their orbital motion. The final interaction is between TYC 3160-1812-1 and TYC 3161-177-1 (i.e., the red parabola). TYC 3161-434-1A, B, and C (i.e., the brown, purple and black parabola) are still a bound system as demonstrated by their almost flat parabolas (the slope is likely cause by their orbital motions) .Finally, by combining all the information from the [Fe/H] and Figure 3.9, we think this could be an unfortunate chance alignment between TYC 3160-1812-1, TYC 3161-177-1, TYC 3161-434-1ABC, i.e. no disintegration is happening.

Note that even though this is not a disintegrating system, however, TYC 3160-1812-1 and TYC 3161-177-1 come quite close to each other, so if there is any planet and/or brown dwarf orbiting either TYC 3160-1812-1 or TYC 3161-177-1, those could have been ejected. Moreover, TYC 3161-434-1AB could have a brown dwarf or exoplanet companion. Given the data we have is not deep enough to see these possible companions, thus deeper observations are essential, e.g., with the James Webb Space Telescope. We could also further investigate this interaction with dynamical simulations.

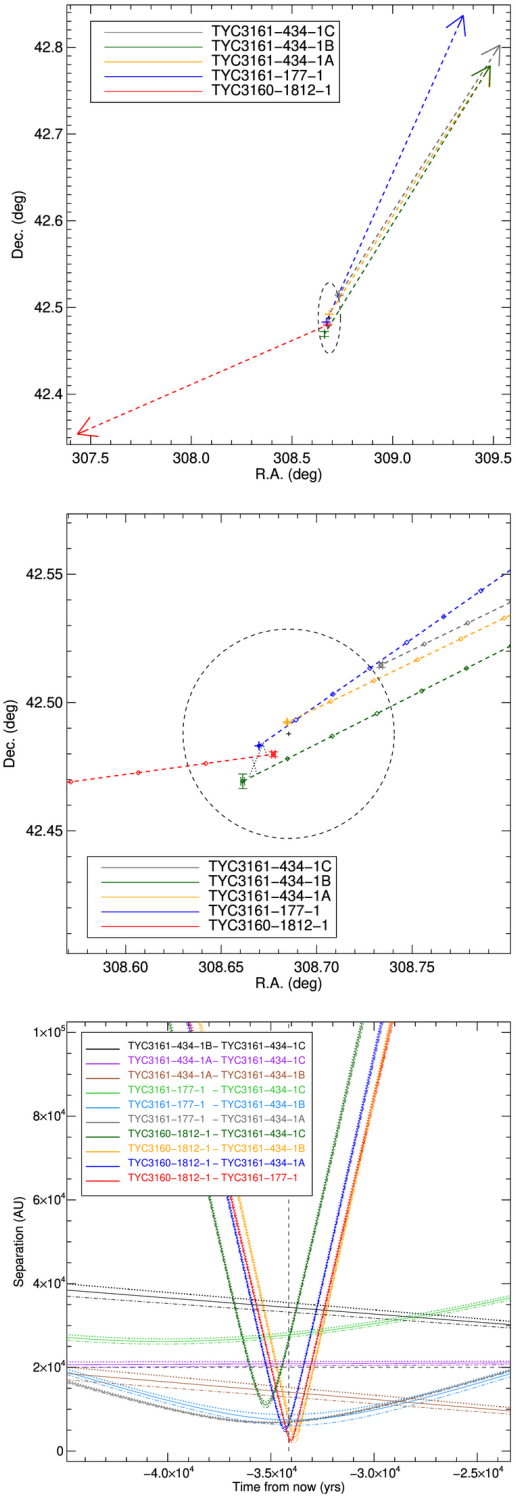

Figure 3.9: *Top panel:* Same as the top panel of Figure 3.3, but for the system consisting of TYC 3160-1812-1, TYC 3161-177-1, and TYC 3161-434-1ABC. We can see that TYC 3160-1812-1 was passing between TYC 3161-177-1 and TYC 3161-434-1ABC, therefore it is likely to cause their disintegration. However, TYC 3161-434-1ABC are still a triple system, because they were not broken apart by the interaction. TYC 3161-434-1A and B seem to be moving closer to each other, which is probably due to orbital motion. *Middle panel:* Same as the middle panel of Figure 3.3, but for the system consisting of TYC 3160-1812-1, TYC 3161-177-1, and TYC 3161-434-1ABC. TYC 3160-1812-1 (i.e., the red dashed line) is likely causing the disintegration of the TYC 3161-177-1 + TYC 3161-434-1ABC system (i.e., the blue, orange, dark green and dark grey dashed line) by first interacting with TYC 3161-177-1 right after the time of closest encounter of the system, then with TYC 3161-434-1AB and last with TYC 3161-434-1C. *Bottom panel:* Same as the bottom panel of Figure 3.3, but for the system consisting of TYC 3160-1812-1, TYC 3161-177-1, and TYC 3161-434-1ABC. TYC 3161-177-1 has its initial encounter with TYC 3161-434-1C (i.e., the lime green parabola) approximately 6000 years prior to the closest encounter with the rest of the system, but given the separation between them is large this is just a very gentle dynamical interaction. The next encounter happened between TYC 3160-1812-1 and TYC 3161-434-1C (i.e., the dark green parabola). TYC 3161-177-1 and TYC 3161-434-1AB (i.e., the dark grey and the dodger blue parabola) also interact at very similar times. The separation at the close encounter between TYC 3161-177-1 and TYC 3161-434-1AB is much smaller in comparison to TYC 3161-177-1 and TYC 3161-434-1C, however given TYC 3161-434-1AB is a tight binary their interaction with TYC 3161-177-1 is likely just as minor as the one described above. The encounter between TYC 3160-1812-1 and TYC 3161-434-1A (i.e., the blue parabola) happened literally just before the closest encounter of the overall system, as should also be the same for TYC 3160-1812-1 and TYC 3161-434-1B (i.e., the orange parabola) after the removal of their orbital motions. The last close encounter was between TYC 3160-1812-1 and TYC 3161-177-1 (i.e., the red parabola). TYC 3161-434-1A, B, and C (i.e., the brown, purple and black parabola) are still a bound system as demonstrated by their almost flat parabolas (the slope is likely caused by their orbital motions). The interaction described here, combined with the inconsistent metallicities, indicate the possibility that both TYC 3160-1812-1 and TYC 3161-177-1 are just chance alignments with the TYC 3161-434-1ABC system.

CHAPTER 4

Identification of additional ultracool dwarf components

To further our understanding of the orbital population (i.e., VLMSs, BDs and GESPs), in this chapter we attempt to find low-mass ejected components from disintegrating multiple systems. This allows us to overcome the challenge caused by the glare of the much brighter parent star. Observing very dim objects companions is proven to be an extremely tough task that requires cutting-edge instruments and enormous amounts of telescope time, consequently it is tremendously costly to observe these very low-mass members via the technical route (i.e. blocking the light of the parent star). These challenges can be avoided altogether by searching for systems where the low-mass companions are being ejected dynamically. Additionally, identifying possible disintegrating multiple systems can place further constraints on the formation models for free-floating BDs and GESPs.

4.1 Observation with Dark Energy Camera (DECam)

To search for additional UCD components, too cold and faint to be seen by Gaia, ejected from our disintegrating multiple systems we obtained deep imaging of a large

Table 4.1: Observation details for the systems presented in this paper. For each system we listed the name of the components, the filter used and the exposure time for each filter.

Name	Filter	Exposure time (s)
TYC 6813-1293-1, TYC 6813-286-1, TYC 6813-643-1AB	r	180×7
	i	180×7
	z	50×7
	Y	40×7
TYC 7240-1438-1, TYC 7240-1159-1, TYC 7240-850-1	r	180×7
	i	180×7
	z	50×7
	Y	40×7
TYC 4936-84-1AB, TYC 4933-912-1AB, TYC 4934-796-1	r	180×7
	i	180×7
	z	50×7
	Y	40×7
TYC 9281-3037-1, TYC 9281-2422-1, TYC 9281-1175-1AB?	r	180×7
	i	180×7
	z	50×7
	Y	40×7
TYC 7731-1951-1, TYC 7731-2128-1AB, TYC 7731-1995-1ABC?	r	180×7
	i	180×7
	z	50×7
	Y	40×7

area around each system with the Dark Energy Camera (DECam; Flaugher et al., 2015) on the Blanco 4m Telescope. We observed each system with the r, i, z and Y filters obtaining 7 exposures on a dithered pattern with offset of 60 arcsecs. The total exposure time for each filter is given in Table 4.1. The exposure times were chosen to reach a S/N=10 depth of $r\sim$24 mag, $i\sim$24 mag, $z\sim$22 mag and $Y\sim$21 mag. For calibration we obtained dome flats, biases and darks. We observed 3 photometric standard fields at different airmass for photometric calibration: SDSSJ1048-0000, SDSSJ0933-0005 and SDSSJ0843-0000.

4.2 Data reduction

The images were processed using the DECam Community Pipeline (Valdes et al., 2014), while the photometry was obtained from the images with a custom pipeline based on the PSF-fitting algorithm DAOPHOTII/ALLSTAR (Stetson, 1987). The final catalog includes only stellar-shaped objects with $|sharpness| \leq 0.5$ to avoid, as much as possible, the presence of non-stellar sources and background galaxies in our analysis.

We converted the instrumental magnitude to calibrated magnitude using the following equation:

$$\begin{aligned} r(\mathrm{AB}) =& 0.998170(\pm 0.000067) \times M_{\mathrm{apcor}} - 0.04394(\pm 0.00029) \times \\ & \mathrm{Airmass} + 0.37797 \end{aligned} \tag{4.1}$$

$$\begin{aligned} i(\mathrm{AB}) =& 0.996426(\pm 0.000071) \times M_{\mathrm{apcor}} - 0.03293(\pm 0.00030) \times \\ & \mathrm{Airmass} + 0.31727 \end{aligned} \tag{4.2}$$

$$\begin{aligned} z(\mathrm{AB}) =& 0.99785(\pm 0.00012) \times M_{\mathrm{apcor}} - 0.04291(\pm 0.00041) \times \\ & \mathrm{Airmass} - 0.07681 \end{aligned} \tag{4.3}$$

$$\begin{aligned} Y(\mathrm{AB}) =& 1.016258(\pm 0.00035) \times M_{\mathrm{apcor}} - 0.03754(\pm 0.00010) \times \\ & \mathrm{Airmass} - 1.479324 \end{aligned} \tag{4.4}$$

Where M_{apcor} is the aperture-corrected instrumental magnitude.

4.3 Measuring PMs

We also calculated PM for the stars in our DECam images. To do that we cross-matched our DECam observations with the Visible and Infrared Survey Telescope for Astronomy (VISTA) Hemisphere Survey (VHS; McMahon et al., 2021), the United Kingdom Infrared Telescope (UKIRT) Infrared Deep Sky Survey (UKIDSS; Lawrence et al., 2007) and 2MASS. We calibrated the measured position for our DECam objects using Gaia DR2 as a reference. First we cross-matched the DECam observations with Gaia DR2 with a radius of 5 arcsec and we kept only Gaia matches that have a measured PM. Then we used the Gaia PM to move each Gaia reference star to the epoch of our DECam observations. We then calculated adjustment to the World Co-ordinate System (WCS) of the DECam images using a least square fit with 3σ outlier rejection. Finally we measured the PM with a linear fit to the positions in the available data,

i.e. combining our DECam epoch with the VHS, UKIDSS, and 2MASS data. Figure 4.1 shows an example for a promising UCD candidate member of the system consisting of TYC 7731-1951-1, TYC 7731-2128-1AB, and TYC 7731-1995-1ABC? (see Section 4.6.5). The top panel shows the VHS J-band image, the middle panel shows our DECam z-band image, and the bottom panel shows the two positions used to measure the PM. In the two images we indicate with a red cross the position of the object at the two epochs. The motion is small but significant, and the PM we measure for this source is consistent with the PM measured by the CatWISE2020 catalog, although the CatWISE2020 PM has bigger uncertainties than our measurement.

4.4 Selection of ultracool dwarf candidates

We search for additional low-mass component of our disintegrating multiple systems using the photometry and PM measured with our DECam data (see Section 4.3 for details). First we used the PMs to calculate the distance that each object in the DECam images had from the centre of the disintegrating system at the time of closest encounter (i.e. column 9 in Table 2.1). We selected only objects that were within 20,000 AU of the centre of the system, since this is the separation of the widest binaries containing UCDs known to date (see e.g. Day-Jones, 2009). We calculated the uncertainty on the separation as a function of time by propagating the uncertainty on the measured position and PM using a Monte Carlo method as follows. For each object, we generate 10,000 "copies" with coordinates and PM taken from a Gaussian distribution centered on the measured values, and with σ equal to the measurement uncertainties. We then computed the separation as a function of time for all of those 10,000 "copies". We assumed as uncertainty the standard deviation of the distribution of 10,000 values. We then looked at the direction of the motion for all of the objects and compared with the direction of the motion of the stellar components of the system. We retained only those objects where the direction of motion is consistent with having been ejected after the close encounter.

4.4.1 Cross-matching with external surveys

To obtain additional photometry for the objects in the DECam images we cross-matched all of the sources with a number of publicly available large-area surveys. The surveys we used are briefly described in the following sections. To cross-match

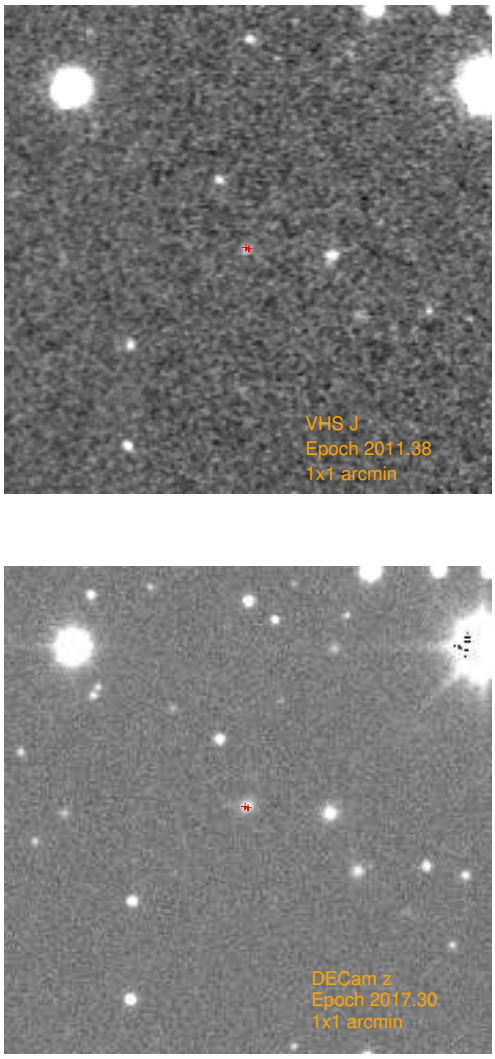

Figure 4.1: An example PM measurements for a promising UCD candidate member of the system consisting of TYC 7731-1951-1, TYC 7731-2128-1AB, and TYC 7731-1995-1ABC? (see Section 4.6.5). *Top panel:* the VHS J-band image. The position of the object in this image and in the DECam image is marked with a red cross. *Middle panel:* the DECam z-band image. The position of the object in this image and in the VHS image is marked with a red cross. *Bottom panel:* The two positions measured from the VHS and DECam images shown above, which were used to measure the PM. Our measurement for this object (see Table 4.2) is consistent with the measurement from the CatWISE2020 catalog, but the CatWISE2020 PM has larger uncertainty ($\mu_\alpha^* = -52 \pm 51$ mas yr^{-1} and $\mu_\delta = -35 \pm 57$ mas yr^{-1}).

the DECam objects, first we downloaded the respective data from the survey archives. For each survey, we downloaded all the data available over the area covered by our DECam images. Then, we used TOPCAT (Taylor, 2005) to perform the cross-match. We used a matching radius of 1 arcsec to minimize the number of false matches. For CatWISE2020 (Marocco et al., 2021) we increased the matching radius to 3 arcsec because of the larger errors on the measured positions in CatWISE2020, especially for the fainter objects. We kept the detections but also the non-detections, because the coldest BDs can be undetected in some of the survey we used, especially those that observe the sky at shorter wavelengths (e.g. PanSTARRS; Chambers et al. 2016) or those that have relatively shallow images (e.g. 2MASS; Skrutskie et al. 2006).

CatWISE

CatWISE (Eisenhardt et al., 2020; Marocco et al., 2021) is an all-sky infrared catalog based on the data from the survey data of of AllWISE (Cutri et al., 2013) as well as the Near Earth Objects WISE (NEOWISE; Mainzer et al., 2011). AllWISE is based on the first year of data from the Wide-field Infrared Survey Explorer (WISE; Wright et al., 2010) and it is in turn a combination of the All-Sky and 3 Bands Cryo data releases. The All-Sky data is in band W1, W2, W3 and W4, while the 3 Bands Cryo data release is only in band W1, W2, and W3. NEOWISE which is a rename of WISE, it is post-cryogenic compared to WISE, and it is still ongoing. All of the NEOWISE observations are at W1 and W2. The Preliminary CatWISE catalog uses all data from 2010 to 2016, and later another two years of data (up to 2018) were added to create the CatWISE2020 catalog. In comparison to AllWISE, CatWISE contains dimmer sources as well as offering much more accurate measurements of their motions. This is due to a much larger span in operation time compared to the original baseline, resulting in an addition of 6 times as many exposures to the AllWISE dataset.

UK Infrared Deep Sky Survey (UKIDSS)

The UK Infrared Deep Sky Survey's (UKIDSS; Lawrence et al., 2007) operation period was between May 2005 to the end of 2011. It has surveyed 7500 square degrees of the Northern sky, extending over both high and low Galactic latitudes. UKIDSS observed in three bands, called J, H, and K, to a depth of $K = 18.3$, which is four magnitudes deeper than its predecessor, 2MASS, thus its image quality is superior and can see fainter stars in comparison (2MASS is considered the predecessor because both cover

the same wavelengths). In addition, it can also be viewed as an extension to the existing SDSS, which observed at a short wavelength (UV and optical) and together they constructed a more complete and clearer map of the Galactic plane. Note that there are five surveys that combine into UKIDSS. Two of them are deep extra-Galactic surveys, with one of them covering 35 square degrees to $K = 21$, and the other covering 0.77 square degrees up to 2 magnitudes deeper, or $K = 23$. The objective of UKIDSS was to discover some of the farthest known objects in the Universe, as well as some of the nearest object to the Sun (outside of our solar system). To search for the nearest and coolest BDs, galaxy clusters and elliptical galaxies at redshift 1<z<2, highest-redshift quasars, at z=7, and high-redshift dusty starburst galaxies are the four prime goals of the UKIDSS. The UKIRT Wide-Field CAMera (WFCAM; Casali et al., 2007) is the survey instrument used to achieve these ambitions. It is mounted on the UK Infrared Telescope (UKIRT) in Hawaii (USA). It has four Rockwell devices (2048X2048) at 94% spacing. It has an exposed solid angle of 0.21 square degrees with a 0.4 arcsec/pixel scale.

Visible and Infrared Survey Telescope for Astronomy Hemisphere survey (VHS)

The Vista Hemisphere Survey (VHS; McMahon et al. 2013) is a near-infrared (NIR) survey that is in the same wavebands (i.e. J and K_s), approximately 30 times deeper than the 2MASS. Its objective is to perform a NIR survey of the whole southern hemisphere (an area of approximately 20 000 square degrees) in at least the two bands mentioned above. In order to yield a median 5σ point source (Vega) limits of J=20.2 and Ks = 18.1, an exposure time of 60 seconds per waveband was required. Additionally, H band were also included in the imaging of the whole South Galactic Cap of approximately 5000 square degrees. A median 5σ point source limiting magnitudes of J = 20.6, H = 19.8 and K_s = 18.5 were the products of a deeper imaging with an exposure time of 120 seconds. Furthermore, the Dark Energy Survey (DES; Abbott et al. 2018) have too provided the deep multi-band optical ($grizY$) imaging data in this region of the sky. The remainder of the high Galactic latitude ($|b| > 30^o$) sky have been imaged in $YJHK_s$ with an exposure time of 60 seconds per band. It then has been combined with the Very Large Telescope Survey Telescope ATLAS survey (VST ATLAS survey; Shanks et al. 2015) which consist of $ugriz$ waveband observations. Finally, by also combining with data such as VISTA Kilo-Degree Infrared Galaxy Survey (VIKING; Edge et al. 2013) from the other Visible and Infrared Survey Telescope for Astronomy

(VISTA) public surveys, the whole area is then being totally covered.

Two Micron All Sky Survey (2MASS)

The Two Micron All Sky Survey (2MASS; Skrutskie et al., 2006) mapped the entire sky in three near-infrared photometric bands: J, H, and K_s. The survey was conducted from 1997 to 2001 and it used two 1.3m telescopes, one in the north hemisphere at the Fred Lawrence Whipple Observatory on Mt. Hopkins (USA) and one in the south hemisphere at the Cerro Tololo Inter-American Observatory (CTIO, Chile). Each telescope was equipped with a 3-channel camera using 256x256 arrays of HgCdTe detectors. The limiting magnitudes achieved by 2MASS were $J = 15.8$, $H = 15.1$, and $K_s = 14.3$.

Panoramic Survey Telescope and Rapid Response System (PanSTARRS)

The Panoramic Survey Telescope and Rapid Response System (PanSTARRS; Chambers et al., 2016) used a dedicated 1.8m telescope located at Haleakala Observatories (HO) on the island of Maui (USA). It performed a large area survey of the sky, covering a total area of 3π steradians north of declination -30 degrees, i.e. 3/4 of the full sky. The survey is done in five bands, g, r, i, z, and Y, and achieved a sensitivity of 23.3, 23.2, 23.1, 22.3, 21.4 magnitude in each band respectively. Observations began in May of 2010 and were completed in April 2014. The latest data release from PanSTARRS is DR2, which was made publicly available in January 2019 (Flewelling et al., 2020).

4.4.2 Colour-colour diagrams and colour-magnitude diagrams

Next we used the DECam photometry and any additional NIR magnitude from the literature to construct a series of colour-magnitude diagrams (hereafter CMD) and used those to select UCD candidates. We used the CMDs from Best et al. (2018), Best et al. (2021), and Kirkpatrick et al. (2011) as reference to estimate the spectral type of our candidates based on their colours. We also derived spectral type estimates using the colour to spectral type and absolute magnitude to spectral type relations from Kirkpatrick et al. (2021), estimating the absolute magnitude of the UCD candidates by assuming that they were at the same distance as the stars in the disintegrating systems. Finally, we also estimated spectral types for the UCD candidates by comparing their colours with the reference colours from Table 1 of Skrzypek et al. (2015). Objects with consistent spectral types from all methods are our most promising candidates. Given

the uncertainties in the measured magnitudes and the large intrinsic scatter among the population of UCDs, we keep objects with spectral types consistent within ∼4 subtypes.

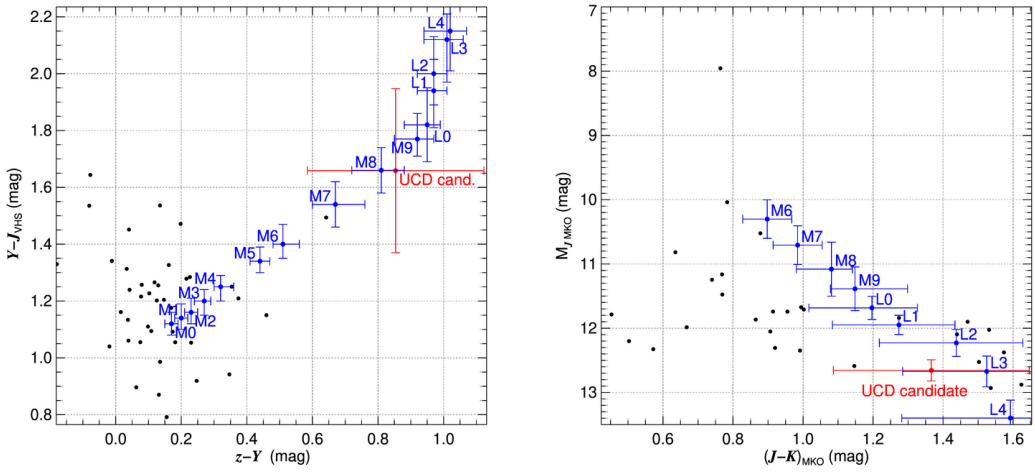

Figure 4.2: Colour-colour diagram (left panel) and colour-magnitude diagram (right panel) for the candidate additional components of the system composed of TYC 7731-1951-1, TYC 7731-2128-1AB, and TYC 7731-1995-1ABC?. The more promising candidate is highlighted in red, whereas initial candidates that were subsequently rejected because of their inconsistent colours and magnitudes are plotted in black. To improve the clarity of the Figure, we omit the error bars on rejected candidates. The uncertainty on the absolute magnitude of the UCD candidate is based on the J magnitude uncertainty and the parallax error of the primary, i.e. TYC 7731-2128-1AB. In blue we mark the median colours and the 1-σ scatter listed in Best et al. (2018). The z and Y magnitude are from our DECam observation, the J magnitude is from the VHS.

4.5 New ultracool dwarf candidates

With the analysis above we identified one very promising UCD candidate associated with the disintegrating system consisting of TYC 7731-1951-1, TYC 7731-2128-1 AB, and TYC 7731-1995-1ABC?. Figure 4.2 shows two examples of colour-colour and colour-magnitude diagrams used for the selection. The left panel shows the z-Y vs Y-J colour-colour diagram, while the right panel shows the M_J vs J-K colour-magnitude diagram. We highlight in red the position of our most promising candidate UCD. In both plots, its colours and magnitude are consistent with the location of late-M and

Table 4.2: Coordinates, PM, and photometry for the new candidate UCD.

Property	Value	Units	Ref.
R.A.	162.299799$\pm(12 \times 10^{-5})$	(deg)	This paper
Dec.	-41.866472$\pm(3.4 \times 10^{-5})$	(deg)	This paper
μ^*_α	-59 ± 24	(mas yr^{-1})	This paper
μ_δ	-25 ± 24	(mas yr^{-1})	This paper
z	21.93±0.13	(mag)	This paper
Y	21.08±0.24	(mag)	This paper
J	19.42±0.16	(mag)	VHS
K	18.08±0.23	(mag)	VHS
$W1$	16.862±0.043	(mag)	CatWISE2020
$W2$	17.37±0.21	(mag)	CatWISE2020

early-L dwarfs, and the spectral types estimates we get from the Kirkpatrick et al. (2021) polynomials and the Skrzypek et al. (2015) colours are all consistent with this object having a spectral type in the range M8–L2. Note that this UCD candidate might have a lower metallicity in comparison to other late-M/early-L dwarfs as it appears to be a bit blue, in comparison, in the W1–W2 colour-colour diagram. We discuss further this object and the system that contains it in Section 4.6.5.

All other UCD candidates in the disintegrating systems presented here are discarded either because their colours and magnitudes lead to inconsistent spectral types, or because visual inspection of their PM and separation as a function of time are inconsistent with them being associated with the main sequence stars in the system. It would be good to obtain spectra for the candidates rejected based on their colors, to check if the selection method used is not rejecting real UCDs that simply happen to have peculiar colors.

4.6 Discussion on individual systems

4.6.1 TYC 6813-1293-1, TYC 6813-286-1 and TYC 6813-643-1AB

A very interesting system in our sample is the one that contains TYC 6813-1293-1, TYC 6813-286-1, and TYC 6813-643-1AB.

TYC 6813-1293-1 is in the catalog of accelerating stars (Brandt, 2021), which means that it is probably an unresolved binary. Its spectral type is F5 (Houk & Smith-Moore, 1988), and it has a metallicity approximately 2 times higher than the other two stars in the system ([Fe/H]=-0.05$\pm$0.2; Gaia Collaboration et al. 2022b). Its RV is also smaller than the other two objects (RV=-46.6$\pm$0.3 km s^{-1}) (Gaia Collaboration et al., 2018a). It has a probability of 99% to be in the thin disk. The probability was computed following the method described in Section 3.4.1. We also checked the probability of the target being in a moving group using BANYAN (Gagné et al., 2018). It has a probability of 99.9% to be a field object.

TYC 6813-286-1 is also known to be a spectroscopic binary (Houk & Smith-Moore, 1988). Its spectral type is F7+A(pSr) (Houk & Smith-Moore, 1988). Its metallicity is 2 times lower than TYC 6813-1293-1 but almost the same as the other object in this system ([Fe/H]=-0.11$\pm$0.04) (Allen & Barbuy, 2006). Its RV is also very similar to the other object in the system (RV=-69$\pm$5 km s^{-1}; Gaia Collaboration et al. 2018a). The RV error is pretty big, which we speculate is due to TYC 6813-286-1 being an unresolved binary. It has a probability of 88% to be in the thin disk, and a probability of 99.9% to be in the field according to BANYAN (Gagné et al., 2018).

TYC 6813-643-1 is resolved by Gaia in two components which form a common-proper-motion-pair. The spectral type for the primary (hereafter A) is K0IV (Pickles & Depagne, 2010), and we estimate the spectral type of the companion (hereafter B) to be M3.5V using the Gaia magnitude and parallax and using Table 5 from Pecaut & Mamajek (2013)[1]. The RV and metallicity of A are very similar to those of TYC 6813-286-1, but with a smaller uncertainty – RV=-61.2$\pm$0.3 km s^{-1} (Buder et al., 2021), [Fe/H]=-0.10$\pm$0.05 (Buder et al., 2021). There is no RV and no metallicity measurement for B. A has a probability of 95% to be in the thin disk, and a probability of 99.9% of being a field object according to BANYAN (Gagné et al., 2018). Because we don't have RV for B we cannot calculate those probabilities for it.

So, overall we assume that TYC 6813-286-1 and TYC 6813-643-1, each of which is a binary, used to form a quadruple system, as confirmed by their nearly identical RV and metallicity. Then they had a close encounter with TYC 6813-1293-1, which did not belong to the original system as demonstrated by its very different RV and metallicity. Now the quadruple is disintegrating. Figure 4.3 shows this more clearly. As one can see in the top and middle panels, TYC 6813-1293-1 (the red arrow and dashed line) passes between the other three objects involved during the close encounter causing

[1] `http://www.pas.rochester.edu/~emamajek/EEM_dwarf_UBVIJHK_colors_Teff.txt`

the disintegration. In particular, the middle panel of Figure 4.3 shows that the interaction between TYC6813-1293-1 and TYC6813-643A and B happens first, followed by the interaction between TYC6813-1293-1 and TYC6813-286-1 (approximately 2,000 years after the system closest encounter). TYC6813-286-1 and TYC6813-643-1A and B interact with each other approximately 5,000-6,000 years after the time of closest encounter. This can also be seen in the bottom panel of Figure 4.3. The red, blue, and orange parabola, which represent the distance between TYC 6813-1293-1 and the other three objects in the system lie below the dark grey and dark green parabolas. In other words, at the time of closest encounter TYC 6813-1293-1 is closer to the other three objects than they are to each other. In particular, we think the interaction that causes the disintegration is the one between TYC 6813-1293-1 and TYC 6813-286-1, because the red parabola reaches the minimum and then, shortly thereafter, the disintegration begins (i.e. the dark grey and dark green parabolas start increasing). Only the binary composed of TYC 6813-643-1 A and B survives the encounter, because the separation between them is significantly smaller than the distance between them and TYC 6813-1293-1, so their gravitational bond is strong enough to prevent the disintegration.

Examining further Figure 4.3, we can see that the parabola of objects TYC 6813-643-1 A and B (i.e. the dodger blue parabola) has a downward slope, seemingly implying that the two objects were further away from each other during the close encounter than they are now. We don't think this is real, and it cannot be explained by the errors on the Gaia PMs because they are too small, i.e. even accounting for the dotted and dash-dotted lines the parabola still does not appear flat. So, we assume it is a result of the fact that the PMs measured by Gaia include the orbital motion, which we cannot remove because we don't know the orbit of the binary. So when we propagate the position back in time this orbital motion causes TYC 6813-643-1 A and B to appear to move closer to each other. To quantify this we can do a quick calculation. We take one object with the same position, PM, and parallax as TYC 6813-643-1 A. We add 1 km s^{-1} orbital velocity to the tangential velocity of this hypothetical star and assume that the orbital velocity only affects the μ_α^* and recalculate the "contaminated" PM for this hypothetical star. We then use this contaminated PM to calculate the position that this star would have at the time of closest encounter, and we find that the 1 km s^{-1} orbital velocity is enough to cause a shift of $\sim$56 arcsec in the observed position, which corresponds to $\sim$6300 AU. We also note that many parabolas reach their minima after the time of closest encounter, and this is probably due to the orbital motion as well. A similar situation we suspect is happening in the top panel of Figure 4.3 with

TYC 6813-286-1. As seen, TYC 6813-286-1 (the blue cross) seems to be outside of the dotted circle at the time of closest encounter, which is the 20,000 AU radius that we used originally to select the candidate disintegrating systems. When we originally selected the candidates we used the TGAS (Gaia Collaboration et al., 2016b) PMs, but now we are using the Gaia DR3 (Gaia Collaboration et al., 2021) PMs. We suspect that because of orbital motion due to the object being an unresolved binary the TGAS (Gaia Collaboration et al., 2016b) and Gaia DR3 (Gaia Collaboration et al., 2021) PMs are slightly different, so the object now seems to be outside of the circle.

Overall, this is a very interesting system, because it could be a quadruple + binary encounter, leading to the disintegration of the quadruple.

4.6.2 TYC 7240-1438-1, TYC 7240-1159-1 and TYC 7240-850-1

TYC 7240-1438-1 is an F3V star (Houk, 1982), TYC 7240-1159-1 is an F8V star (Pickles & Depagne, 2010), and TYC 7240-850-1 is a G5V star (Pickles & Depagne, 2010). All three objects have approximately solar metallicity (0.0$\pm$0.2, Gaia Collaboration et al. 2022b; 0.05$\pm$0.06, Kunder et al. 2017; 0.07$\pm$0.07, Kunder et al. 2017), although the [Fe/H] measurement for TYC 7240-1438-1 has large uncertainties. The three objects all have different RV from each other and all have good measurements with relatively small uncertainties. TYC 7240-1438-1 has RV = 12.4$\pm$0.3 km s^{-1}, TYC 7240-1159-1 has RV = -9.4$\pm$0.5 km s^{-1}, and TYC 7240-850-1 has RV = 20.7$\pm$0.2 km s^{-1} (all measurements are from Gaia Collaboration et al., 2022b). All three stars have a probability >97% of belonging to the thin disk (see description of methodology in Section 3.4.1) and, according to BANYAN (Gagné et al., 2018), all three stars have a probability of 99.9% of being field objects. None of the three objects is flagged to be a possible unresolved binary.

We can see in the top panels of Figure 4.4 that TYC 7240-1438-1 passes between the other two objects, so it could be the cause of the disintegration of the system. However, we see in the bottom panel of Figure 4.4 that the separation between TYC 7240-1159-1 and TYC 7240-850-1 (i.e. the orange parabola) starts increasing before the interaction between TYC 7240-1438-1 and the other two objects. In other words, the orange parabola reaches the minimum before the red and blue parabolas. So, it appears that the possible binary formed by TYC 7240-1159-1 and TYC 7240-850-1 was already disintegrating at the time of closest encounter with TYC 7240-1438-1. This

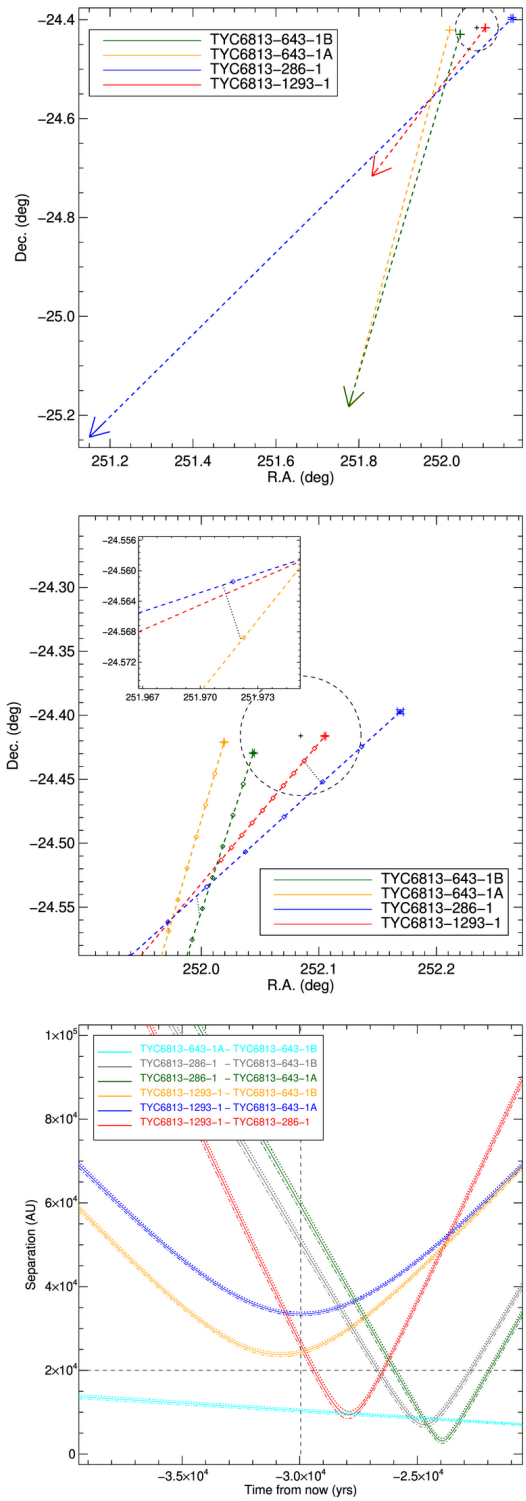

Figure 4.3: *Top panel:* the position of TYC 6813-1293-1, TYC 6813-286-1 and TYC 6813-643-1 AB now and at the time of closest encounter of the system. For each object, the arrow indicates the current direction of motion, the dashed line connects the current position with the position at the time of closest encounter, marked by a cross. The small black cross is the centre of the system at the time of closest encounter, and the black dashed circle has a radius of 20,000 AU. TYC 6813-1293-1 passes between the other three objects, likely causing their disintegration. *Middle panel:* same as the top panel, but zoomed in on the position of closest encounter. Symbols and colours are the same as the top panel, and we added diamonds to show the position of each object in intervals of 1,000 years after the time of closest encounter, up to a maximum of 10,000 years. For pairs of objects that did not reach their mutual minimum separation at the time of closest encounter for the system, a dark grey dotted line shows the position and the time when their interaction took place. TYC6813-1293-1 (red dashed line) is likely causing the disintegration of TYC6813-286-1 (blue dashed line) and TYC6813-643-1AB (orange and dark green dashed lines) by first interacting with TYC6813-643-1AB, and later interacting with TYC6813-286-1. The interactions between TYC6813-643-1B and TYC6813-286-1 and between TYC6813-643-1A and TYC6813-286-1 happened later on. *Bottom panel:* The separation between the components of the system as a function of time. The vertical dashed line marks the time of closest encounter while the horizontal dashed lines indicates a separation of 20,000 AU. The dotted and dash-dotted line above and below each parabola indicate the one-sigma uncertainty range. TYC 6813-1293-1 comes to a closer separation from TYC 6813-286-1 and TYC 6813-643-1AB than the separation between TYC 6813-286-1 and TYC 6813-643-1 AB (i.e. the red parabola is at smaller separation than the dark grey and dark green parabolas at the time of closest encounter), causing the breakup of the system. TYC 6813-643-1 AB, however, survives the encounter and continues onward as a binary (i.e. the dodger blue parabola, see Section 4.6.2 for discussion of its slope). The dark grey and dark green parabola do not reach the minimum at the same time, contrary to what one might expect from a binary. However, we think this is due to orbital motion for the binary.

leaves us with two possible explanations – either TYC 7240-1159-1 and TYC 7240-850-1 were not a binary to begin with but just two objects passing near each other, or TYC 7240-1159-1 and TYC 7240-850-1 were a binary, but their disintegration is caused by another, yet unseen, object.

4.6.3 TYC 4936-84-1 AB, TYC 4933-912-1 AB, and TYC 4934-796-1

TYC 4936-84-1 is a K1III star (Pickles & Depagne, 2010) with a slightly low metallicity ([Fe/H] = -0.12±0.09; Kunder et al. 2017) and a small RV (RV = -1.80±0.80 km s^{-1}; Gaia Collaboration et al., 2018a). It has a probability of 99% of belonging to the thin disk. Gaia DR3 resolves a fainter companion, for which we estimate a spectral type of M4.5V using its absolute *G* magnitude, parallax, and its colours (i.e. *G-BP*, *G-RP*, *BP-RP*) with Table 5 from Pecaut & Mamajek (2013). No metallicity estimate or measurement is available for the companion. We will refer to this binary as TYC 4936-84-1 AB. TYC 4933-912-1 is a K0V star (Pickles & Depagne, 2010) with a slightly high measured metallicity ([Fe/H] = 0.19±0.05; Buder et al. 2021) and a measured RV = 15.90±0.07 km s^{-1} (Buder et al., 2021). We compute a probability of 98% of belonging to the thin disk. This object is listed in the SUPERWIDE catalog (Hartman & Lépine, 2020) as SWB11354. Its companion is a K8V which we will call TYC 4933-912-1 B. The spectral type was estimated by us using the absolute *G* magnitude, parallax, and the Gaia DR3 colours, as described above. The parallax, PM, and RV of the two objects agree very well (RV = 17.3±0.8 km s^{-1}; Gaia Collaboration et al., 2022b), so it is highly likely that this object is a real binary, however, the metallicity measurement for TYC 4933-912-1 B is [Fe/H] = 0.02±0.07 (Kunder et al., 2017), which is not consistent with the metallicity for TYC 4933-912-1 A. This is puzzling since one would expect that the two components of a binary have the same metallicity since they formed from the same material. Given our analysis in Section 2.1.7, we do not think this is due to a systematic difference between GALAH and RAVE leading to a spurious difference between the two components. Another more exotic explanation is that the metallicity of the two objects is different because the two stars did not form together but the K0V captured at some point the K8V. Further followup is needed to clarify the nature of this pair. TYC 4934-796-1 is a K0V (Pickles & Depagne, 2010) with a high metallicity ([Fe/H] = 0.29±0.05; Buder et al. 2021), and a measured RV = -19.89±0.06 km s^{-1} (Buder et al., 2021). Gaia DR2 reports a RV of -19.2 ± 0.5 km s^{-1}, while Tsantaki et al.

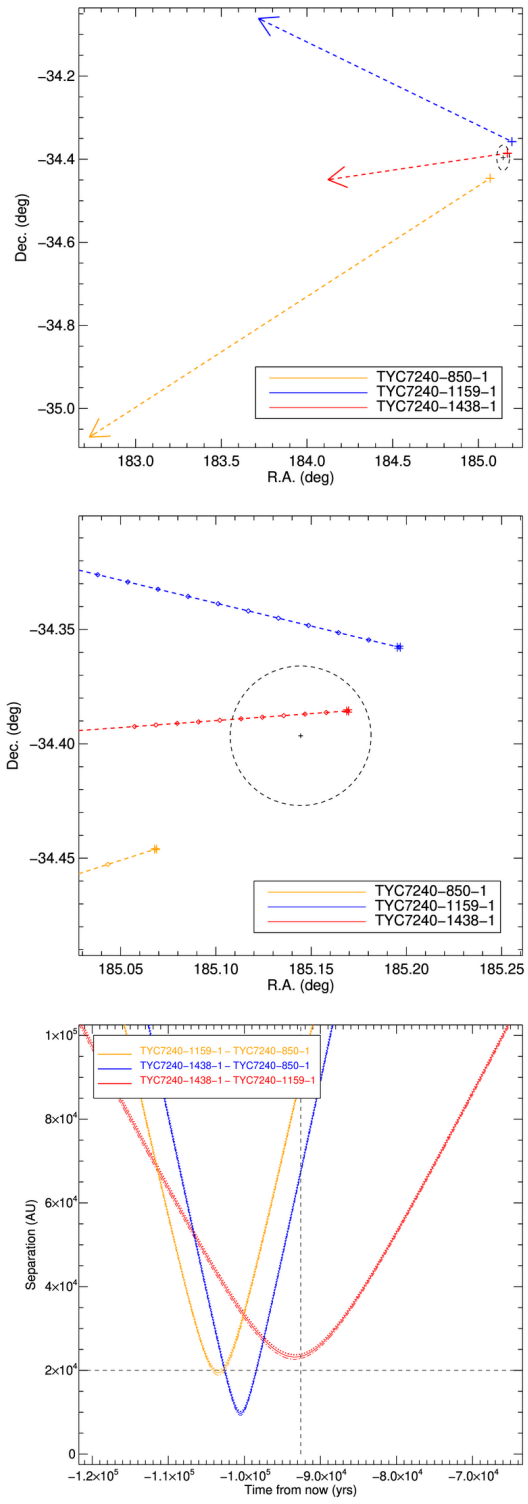

Figure 4.4: *Top panel:* Same as the top panel of Figure 4.3, but for the system consisting of TYC 7240-1438-1, TYC 7240-1159-1 and TYC 7240-850-1. TYC 7240-1438-1 passes between the other two objects, so it could be causing their disintegration. *Middle panel:* same as the middle panel of Figure 4.3 but for the system consisting of TYC 7240-1438-1, TYC 7240-1159-1 and TYC 7240-850-1. All objects in this system have their initial interaction at the time of closest encounter of the system (marked by a cross). As shown in the top panel, TYC 7240-1438-1 (the red dashed line) passes between TYC 7240-1159-1 (the blue dashed line) and TYC 7240-850-1 (the orange dashed line), possibly triggering the disintegration of the binary. *Bottom panel:* Same as the bottom panel of Figure 4.3, but for the system consisting of TYC 7240-1438-1, TYC 7240-1159-1 and TYC 7240-850-1. The separation between TYC 7240-1159-1 and TYC 7240-850-1 (orange parabola) reaches its minimum before the separation between them and TYC 7240-1438-1 (red and blue parabola), meaning that the system was already disintegrating before the close encounter.

(2022) reports a RV of -20.8 ± 0.7 km s^{-1}. Both measurements are consistent with the one from Buder et al. (2021). It has a probability of 99% of belonging to the thin disk, regardless of which RV we use for the calculation. All of these five objects have a probability of 99.9% of being field objects according to BANYAN (Gagné et al., 2018).

The true nature of this system is unclear. Looking at the top panels of Figure 4.5 we can see that the two binaries (TYC 4936-84-1 AB and TYC 4933-912-1 AB) and TYC 4934-796-1 are going in three different directions, almost perpendicular to each other. This can be interpreted as a simple close encounter between three unrelated systems, with no visible disintegration occurring. However, it is still possible that there could be unseen low-mass objects ejected by one of the three systems. Another possibility is that TYC 4933-912-1 AB and TYC 4934-796-1 used to be a triple system, and now, after the interaction with TYC 4936-84-1 AB, they are disintegrating. This hypothesis comes from the fact that TYC 4934-796-1 and TYC 4933-912-1 A have metallicity which is consistent with each other within their errors but, as we discussed above, the metallicity of TYC 4933-912-1 A and B need further investigation to explain their inconsistency. The bottom panel of Figure 4.5 could help explain the nature of this system. The red and brown parabolas represent TYC 4936-84-1 AB and TYC 4933-912-1 AB, which are still bound together, so their separation does not increase with time. We note that both parabolas have a shallow slope to them, most likely due to the unaccounted orbital motion of the pairs. In practice, since the Gaia astrometric solution assumes that these objects are singles and not binaries, it does not separate the PM of the object from its orbital motion. The measured PM in the Gaia catalogue is, therefore, the sum of the PM and the orbital motion, and this makes it appear as if the two objects are moving closer to each other. Figure 4.5 shows that the two binaries interact first, i.e. the blue, orange, dark grey, and dodger blue parabola reach their minima first, with minimum separation of $\lesssim$5,000 AU. This could be causing the ejection of TYC 4934-796-1 from the TYC 4933-912-1 AB system. The separation between these three objects, represented by the purple and black parabola, starts increasing just after the interaction between the two binaries. However, the current direction of motion for TYC 4933-912-1 AB and TYC 4934-796-1 are almost exactly opposite to each other, and it is unlikely for the interaction to have caused such a large change of course for an object as massive as a K0V star. Finally, TYC 4934-796-1 has a close encounter with the TYC 4936-84-1 AB (i.e. the dark green and lime green parabola) approximately 3,000 years after the disintegration began or approximately 1,000 years after the time of closest encounter of the full system (see bottom and middle panels of Figure 4.5).

Further analysis of this system, in particular of the discrepancy between the metallicity of TYC 4933-912-1 A and B could help clarify the nature of this system.

4.6.4 TYC 9281-3037-1, TYC 9281-2422-1, and TYC 9281-1175-1AB?

TYC 9281-3037-1 is a G0V star (Pickles & Depagne, 2010) with a very low metallicity of -2.3±0.1 (Buder et al., 2021) and a very high PM and RV (238.1±0.9 km s^{-1}, Buder et al., 2021). Because of its high PM and RV, this object has a probability of 100% of belonging to the halo (see methodology above), which is consistent with its low metallicity. We found that Gaia DR3 has a slightly discrepant RV = 230.4±2.4 km s^{-1}, but even if we assume the Gaia value instead of the Buder et al. (2021) value the probability to belong to the halo remains 100%. TYC 9281-2422-1 is a G5V star (Pickles & Depagne, 2010) with an estimated metallicity which is consistent with solar, but with large uncertainties ([Fe/H] = 0.2±0.4; Ammons et al. 2006). It has a relatively low RV, but its measurement also has large uncertainty (RV = 16±6 km s^{-1}, Gaia Collaboration et al., 2022b). We speculate that this large uncertainty could be due to this object being an unresolved binary, i.e. the large uncertainty could be a result of line broadening due to the orbital velocity of the pair with the orbital plane being almost aligned with the line of sight. Gaia does not resolve the possible system. Despite the large RV uncertainty, this object has a probability of 99% of belonging to the thin disk. TYC 9281-1175-1A is an F8V star (Pickles & Depagne, 2010) with a well measured metallicity of 0.06±0.08 (Buder et al., 2021) and a well measured RV = -5.2±0.1 km s^{-1} (Buder et al., 2021). Gaia DR3 reports a RV of -5.0 ± 0.2 km s^{-1} and Tsantaki et al. (2022) reports a RV of -4.9 ± 0.3 km s^{-1}, which are consistent with the Buder et al. (2021) value. Gaia resolves the object in two separate sources, but does not provide parallax nor PM measurement for the secondary, so we cannot conclude if this secondary source is a real companion or just a chance alignment with a background source. If we assume that the secondary is at the same distance as the primary, then we can use its Gaia *G* magnitude to estimate its spectral type to be M5V. TYC 9281-1175-1AB? has a probability of 99% of belonging to the thin disk, regardless of which RV we use for the calculation. According to BANYAN (Gagné et al., 2018) all of the stars are members of the field with a probability of 99.9%.

We speculate that TYC 9281-2422-1 and TYC 9281-1175-1AB? used to form a binary because their similar [Fe/H] and somewhat similar kinematic, and that TYC 9281-

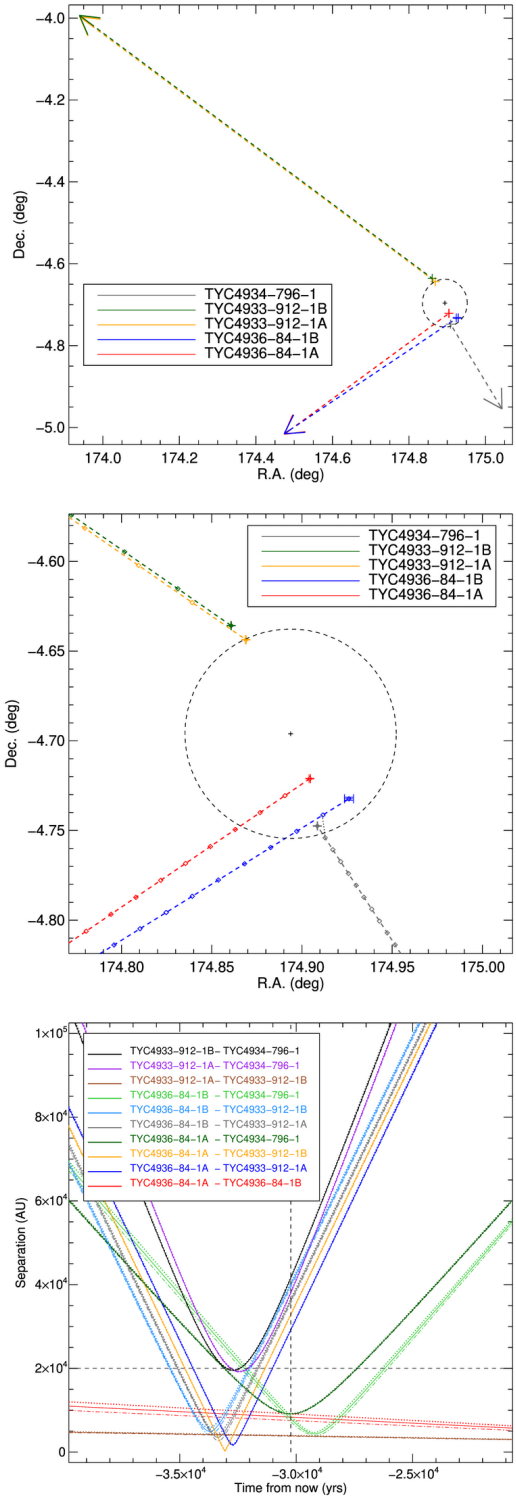

Figure 4.5: *Top panel:* Same as the top panel of Figure 4.3, but for the system consisting of TYC 4936-84-1 AB, TYC 4933-912-1 AB, and TYC 4934-796-1. The direction of motion of the two binaries and TYC 4934-796-1 are almost perpendicular to each other, so it is likely that these systems were unrelated to each other, and this is just a close encounter without any visible disintegration. *Middle panel:* same as the middle panel of Figure 4.3, but for the system consisting of TYC 4936-84-1AB, TYC 4933-912-1AB and TYC 4934-761-1. All objects in this system have their initial interaction at the time of closest encounter of the system (marked by a cross) except for TYC 4936-84-1B (the blue dashed line) and TYC 4934-796-1 (the dark grey dashed line) which first interacted around 1,000 years after the system closest encounter. This candidate system appears to be just a chance alignment. *Bottom panel:* Same as the bottom panel of Figure 4.3, but for the system consisting of TYC 4936-84-1 AB, TYC 4933-912-1 AB, and TYC 4934-796-1. The two binaries have a close encounter first (i.e. the blue, orange, dark grey, and dodger blue parabola reach their minima first), then the separation between TYC 4933-912-1 AB and TYC 4934-796-1 start increasing (purple and black parabola), so this could be a sign of the disintegration of the system. However, the current direction of motion of TYC 4933-912-1 AB and TYC 4934-796-1 are almost opposite to each other, and it is unlikely for an interaction to have caused such a dramatic change of path. TYC 4936-84-1 AB and TYC 4933-912-AB remain bound as binaries, however their parabolas (red and brown) appear to show that the components are moving closer to each other. We attribute this to unaccounted orbital motion (see Section 4.6.3 for further discussion)

3037-1, a halo star, caused their breakup. Looking at the top panels of Figure 4.6 we can see that TYC 9281-3037-1 (red arrow and dashed line) passes between TYC 9281-2422-1 (blue arrow and dashed line) and TYC 9281-1175-1A (orange arrow and dashed line), so this interaction could be the cause of the disintegration. The bottom panel of the same Figure confirms this, as we can see that TYC 9281-3037-1 comes quite close with TYC 9281-1175-1A first (i.e. the blue parabola reaches its minimum first), then interacts with TYC 9281-2422-1 (i.e. the red parabola reaches its minimum second). We can also see that this appears to be a more "gentle" breakup compared to the other systems studied here, since the separation between TYC 9281-2422-1 and TYC 9281-1175-1A increases slowly (i.e. the orange parabola is almost flat).

Deep AO imaging and/or RV monitoring of TYC 9281-2422-1 and TYC 9281-1175-1AB? could be useful to understand if either of those object is itself a tight binary.

4.6.5 TYC 7731-1951-1, TYC 7731-2128-1AB, and TYC 7731-1995-1ABC?.

TYC 7731-1951-1 is a G5V star (Pickles & Depagne, 2010) with a low estimated metallicity, but with large uncertainties ([Fe/H] = -0.3±0.2; Gaia Collaboration et al. 2022b). Using its well measured RV (RV = 32.6±0.3 km s^{-1}; Gaia Collaboration et al., 2022b) we find that this object has a probability of 97% of belonging to the thin disk. TYC 7731-2128-1 is a G0V star (Pickles & Depagne, 2010) with an estimated metallicity of [Fe/H] = 0.3±0.3 (Ammons et al., 2006). This star has a low RV = 0.6±0.2 km s^{-1} (Gaia Collaboration et al., 2022b) but because of its high PM, it has a probability of 76% of belonging to the thick disk, and only 24% of belonging to the thin disk. We found that it has a close companion resolved by Gaia (Gaia Collaboration et al., 2021), with parallax and PM consistent with being a companion to TYC 7731-2128-1. So we call the primary TYC 7731-2128-1 A and this new companion TYC 7731-2128-1 B. We estimate the spectral type of the new companion using its absolute *G* magnitude, parallax, and the Table 5 from Pecaut & Mamajek (2013), and find that this is an M3V. There are no [Fe/H] nor RV measurements for TYC 7731-2128-1 B. TYC 7731-1995-1A is a K0III (Houk, 1978). The estimated [Fe/H] is 0.2±0.2 (Gaia Collaboration et al., 2022b), and its RV is 5.3±0.1 km s^{-1} (Gaia Collaboration et al., 2018a). Using the parallax, PM, and RV we estimate a probability of 99% of belonging to the thin disk. This object is also in the catalog of accelerations (Brandt, 2021) indicating that it could be an unresolved binary. Its measured RV has small uncertainties, but this could be due to the fact that

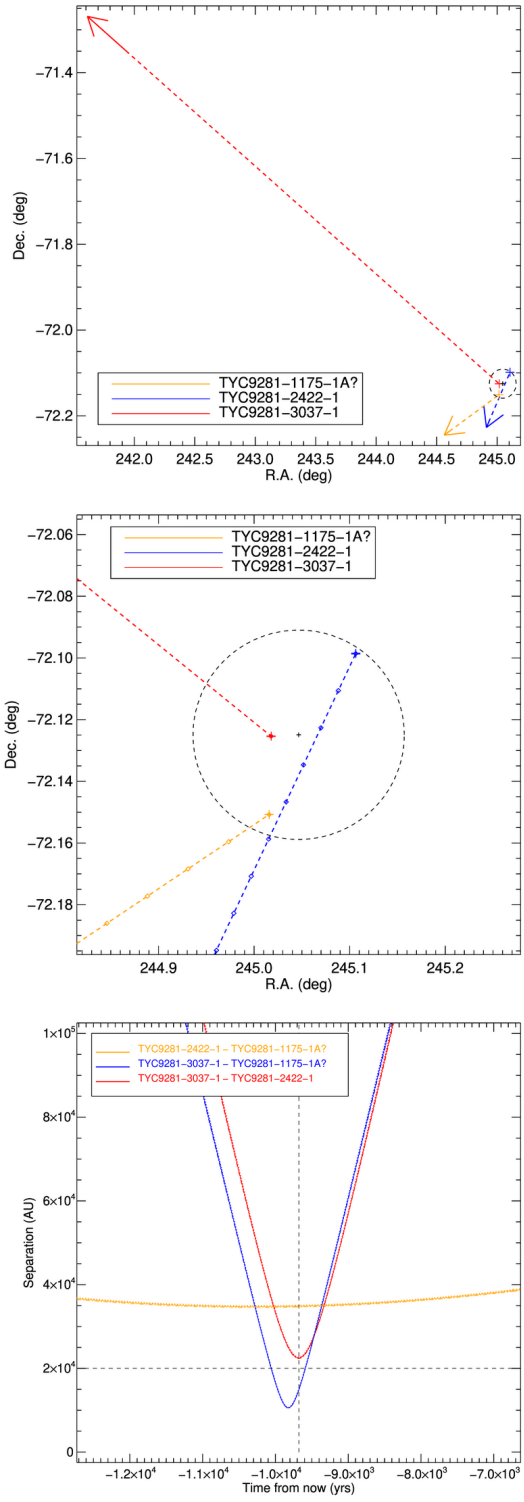

Figure 4.6: *Top panel:* Same as the top panel of Figure 4.3, but for the system consisting of TYC 9281-3037-1, TYC 9281-2422-1, and TYC 9281-1175-1A?. The possible unresolved companion to TYC 9281-1175-1A? is not shown because there is no PM measurement available for it. TYC 9281-3037-1 passes between the other two objects, so it could be causing their disintegration. *Middle panel:* same as the middle panel of Figure 4.3, but for the system consisting of TYC 9281-3037-1, TYC 9281-2422-1 and TYC 9281-1175-1A?. All objects in this system have their initial interaction at the time of closest encounter of the system (marked by a cross). The fast moving TYC 9281-3037-1 leaves the area shown in less than 1,000 yr, so there is no red diamond in the plot. As shown in the top panel, TYC 9281-3037-1 (the red dashed line) passes between TYC 9281-2422-1 (the blue dashed line) and TYC 9281-1175-1A? (the orange dashed line), so it is likely to be the cause of the disintegration of the binary/triple. *Bottom panel:* Same as the bottom panel of Figure 4.3, but for the system consisting of TYC 9281-3037-1, TYC 9281-2422-1, and TYC 9281-1175-1A?. The possible unresolved companion to TYC 9281-1175-1A? is not shown because there is no PM measurement available for it. TYC 9281-3037-1 passes between the other two objects, as shown by the red and blue parabolas reaching a smaller separation than the orange parabola. This interaction could be the cause of the disintegration of the system. The disintegration in this case is "gentle" as shown by the orange parabola being almost flat, i.e. the separation between TYC 9281-2422-1 and TYC 9281-1175-1A? increases slowly.

the orbital plane of the binary is perpendicular to the line of sight, so the orbital velocity does not contribute much to the RV uncertainty. Using ALADIN (Bonnarel et al., 2000), we see that there is another object very close to this target, but Gaia DR3 (Gaia Collaboration et al., 2021) does not report the parallax nor the PM of this other object, so we cannot establish if this new object is a companion to TYC 7731-1995-1A (hence the cause of its acceleration) or just a background star. If we assume that this new star is at the same distance as the K0III, we estimate its spectral type to be M3V. According to BANYAN, TYC 7731-1951-1, TYC 7731-2128-1 AB, and TYC 7731-1995-1ABC? are all field objects.

Even though we do not have good [Fe/H] measurement to establish which object were previously associated, we can still use Figure 4.7 to interpret the close encounter. The top panels of Figure 4.7 show that TYC 7731-1951-1 comes close to TYC 7731-2128-1 AB and TYC 7731-1995-1AB? and then move on. The bottom panel of Figure 4.7 gives us a more complete picture of the interaction. TYC 7731-1951-1 interacts with TYC 7731-2128-1 AB (red and blue parabolas) but comes closer to TYC 7731-2128-1 B. Shortly thereafter, the disintegration between TYC 7731-2128-1 AB and TYC 7731-1995-1AB? begins (dark grey and dodger blue parabolas, see also the inset of the middle panel). So we conclude that the interaction between TYC 7731-1951-1 and TYC 7731-2128-1 AB is the cause of the disintegration of the triple system (or maybe quadruple). We note that the dark grey and dodger blue parabola are slightly different from each other even though in theory they should be identical (because TYC 7731-2128-1 A and B are binary) and we think that this difference is due to the orbital motion of the binary. We can also see that TYC 7731-2128-1 AB is still a binary because the separation between the two components is constant (dark green parabola). We can also see that TYC 7731-1951-1 and TYC 7731-1995-1AB? come close to each other $\sim$2000 yr after the disintegration began, so this interaction cannot be the cause (see the orange parabola in the bottom panel as well as the middle panel of Figure 4.7).

Better metallicity measurements for all objects in this system would help us confirm the scenario we think is likely. A measurement of the parallax and PM for the newly discovered object near TYC 7731-1995-1AB? is needed to find out is these two objects form a binary or if it is just a chance alignment.

The analysis described in Section 4.4 revealed a possible additional ejected UCD component of this system. The left panel of Figure 4.8 shows that the PM for the new UCD is well aligned with the PM of TYC 7731-2128-1 AB, suggesting that the UCD candidate could have formed a triple system with those two stars. We note that the

PM measurement for this UCD is based on the DECam observation combined with the VHS J data. The right panel of Figure 4.8 shows that the parabola for the UCD reaches its minimum very close to the time of closest encounter, marked by a vertical dashed line. Even though the errors on the UCD candidate parabola are larger than those on the TYC stars, the maximum separation at the time of closest encounter is $\lesssim 3.5 \times 10^4$ AU, therefore it is plausible that this object was initially part of the system and is being ejected as a result of the disintegration of the system. The UCD is well detected in our DECam z image, but only barely detected in the Y image. Moreover, the UCD candidate is also well detected in the VHS J and K data, as well as the WISE $W1$ data, but only barely detected in the $W2$ image. It is undetected in Gaia DR3. Further inspection of DSS2 B images reveal a faint detection at the location of the UCD. This detection is puzzling and in disagreement with the fact that this source does not appear in Gaia DR3, since the Gaia G and $G_{\rm BP}$ filters both overlap the DSS2 B filter, and Gaia DR3 is much deeper than DSS2. We propose three possible explanations for this puzzling detection. The first possible explanation is that the DSS2 detection is spurious, i.e. an image artifact. The second possible explanation is that the DSS2 detection is real, but it is not associated with our UCD candidate. The fact that this source does not appear in Gaia DR3 can be explained assuming that the DSS2 source is a transient (e.g. a nova, or a long-period variable source). If this is the case, since this source is only detected in DSS2 B but not in DSS2 R and IR, we can assume that it does not contaminate the photometry and astrometry of our UCD, which is based only on near-infrared data. The third possible explanation is that the DSS2 detection is real and it is actually associated with our UCD candidate. This would mean that our candidate is not a UCD but instead some background object with peculiar colours, and probably variable at short wavelength. Using the available photometry (excluding the puzzling DSS2 B detection), assuming that the object is at the same distance as the TYC stars, and employing the method described in Section 4.4, we find that this UCD candidate is likely an early-L dwarf. Looking at the left panel of Figure 4.2 we can see that given the relatively large error bars the $z - Y$ colour is consistent with spectral type M7–L4, while the $Y - J_{\rm VHS}$ colour is consistent with spectral type M6–L1 (but we note that the 1-σ error bars for the UCD candidate also overlap the 1-σ scatter range for M5 and L2). The right panel of Figure 4.2 shows that the $(J - K)_{\rm MKO}$ colour is consistent with spectral type M8–L4. The strongest constraint on the spectral type comes from the $M_{J\rm MKO}$ which is consistent with L3. This estimate however is a bit inconsistent with the estimate that comes from the $Y - J_{\rm VHS}$ colour. Overall, we conclude that this could

be a slightly underluminous and slightly blue L2–L3 dwarf. Its properties are listed in Table 4.2. Additional imaging would help to further improve the photometry and the PM measurement for this object, and spectroscopy is desirable to confirm or refute its nature, thus clarifying the mystery surrounding the DSS2 *B* detection.

If this additional object is confirmed to be a UCD, it would be the first example of an ejected UCD benchmark.

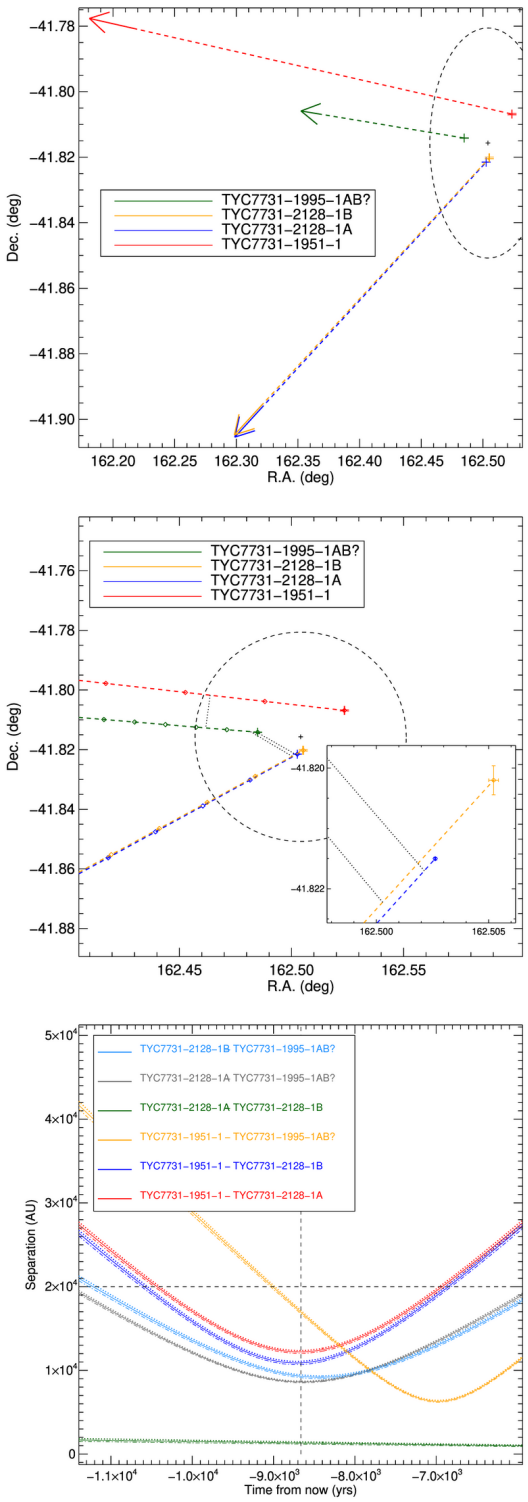

Figure 4.7: *Top panel:* Same as the top panel of Figure 4.3, but for the system consisting of TYC 7731-1951-1, TYC 7731-2128-1 AB, and TYC 7731-1995-1AB?. The possible companion to TYC 7731-1995-1AB? is not shown because there is no PM measurement available for it. The interaction between TYC 7731-1951-1 and TYC 7731-2128-1 AB is likely to cause the breakup of the TYC 7731-2128-1 AB and TYC 7731-1995-1AB? system. *Middle panel:* same as the middle panel of Figure 4.3, but for the system consisting of TYC 7731-1951-1, TYC 7731-2128-1AB and TYC 7731-1995-1AB?. All objects in this system have their initial interaction at the time of closest encounter of the system (marked by a cross) except for TYC 7731-1951-1 (the red dashed line) and TYC 7731-1995-1AB? (the dark green dashed line) which interact just before the 2,000 years mark, TYC 7731-2128-1A (the blue dashed line) and TYC 7731-1995-1AB? as well as TYC 7731-2128-1B (the orange dashed line) and TYC 7731-1995-1AB? which have their interaction shortly after the closest encounter of the system. TYC 7731-1951-1 (red dashed line) is likely causing the disintegration of TYC 7731-2128-1AB and TYC 7731-1995-1AB? (blue, orange and dark green dashed lines) by first interacting with TYC 7731-2128-1AB, then later interacting with TYC 7731-1995-1AB? (the dark green dashed line). *Bottom panel:* Same as the bottom panel of Figure 4.3, but for the system consisting of TYC 7731-1951-1, TYC 7731-2128-1 AB, and TYC 7731-1995-1AB?. The possible companion to TYC 7731-1995-1AB? is not shown because there is no PM measurement available for it. TYC 7731-1951-1 passes very close to TYC 7731-2128-1 AB (red and blue parabolas) likely triggering the disintegration of the TYC 7731-2128-1 AB and TYC 7731-1995-1AB? system (dark grey and dodger blue parabolas). TYC 7731-2128-1 AB survives the encounter (dark green parabola).

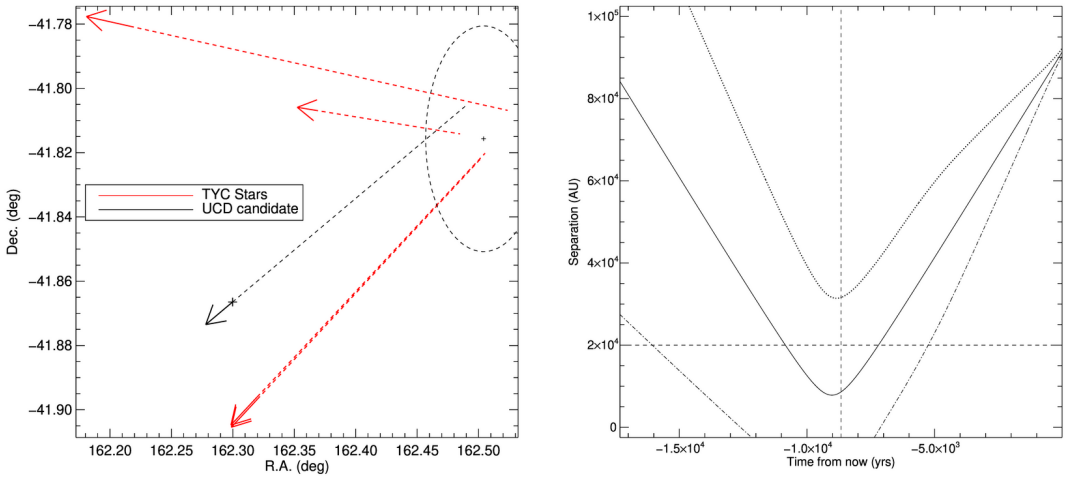

Figure 4.8: *Left panel:* Same as the top panel of Figure 4.7, but highlighting the possible UCD ejected component discovered here. The TYC stars are plotted in red, while the UCD is plotted in black. *Right panel:* Same as the bottom panel of Figure 4.7, but showing only the possible new UCD ejected component discovered here. The solid parabola shows the separation as a function of time between the UCD and the center point of the disintegrating system at the time of closest encounter. The dotted and dash-dot parabolas are the upper and lower 1σ uncertainties.

CHAPTER 5

Conclusions and Future work

5.1 Conclusions

One of the longtime main research interests in the LMSs and BDs research community is to gain more knowledge on the dominant formation mechanism of ultra-cool objects. Observational constraints are vital in improving various suggested formation models, especially those on the binary fraction and the IMF (e.g. Stamatellos et al., 2012). Furthermore, the initial requirements for capture and even the origin of some of the free-floating field planetary-mass objects could also gain some insight or even be answered through the study of disintegrating multiple systems.

The method used in this project to search for candidate disintegrating systems in the TGAS catalogue was first described in Yip et al. (2016). In general, the principle of this method is to first make sure all components within each candidate system share a common distance (reducing possible selection of chance alignment) via the use of distance measurements and constraints from trigonometric parallax and spectrophotometric techniques. The next step is to select possible systems that do not have CPM (hence that are likely to be disintegrating) by using their relative PMs and their associated measurement uncertainties. The last step is to fine tune the selection of more genuine candidate disintegrating systems with the aid of relative component positions that are tracked back and projected forward through time. In this thesis I proved not only that this method works, but also that it is robust, as demonstrated by the 20

possible disintegrating multiple systems uncovered here.

Though in consideration that disintegration can be a complex process, I began with the investigation of two main types of break up. The first type is when the group is completely disintegrating due to more violent interactions. Hence, all objects have broken away from the original system, i.e., the disintegrating multiple system consists of associations where all three components are moving away from each other (hereafter Group A – 15 systems). The other type is when the group has only one object that is breaking away while the rest of the system remains bound because of a gentler interaction, i.e., the disintegrating multiple system consists of a possible binary and a third object that is moving away from the binary (hereafter Group B – 5 systems). In this project, then I explored 9 of these candidate systems, which are all from Group A. Aiming to search for possible UCD/s that could be part of the disintegrating system, I lead a proposal to follow-up 5 of these systems with the use of DECam. The proposal (ID 2017A-0918) was awarded one night via the CNTAC. The observations were carried out in visitor mode by myself and my advisor, Prof. Radostin G. Kurtev. The other 4 candidate systems were followed up with ISIS, to measure the [Fe/H] and RV information needed to further confirm their likelihood of being genuine disintegrating systems. This was done through a proposal to ING (ID SW2017a08) which was awarded 5 hours. The observations were conducted in service mode. The remaining 6 candidate systems that were not investigated are solely because of them being unobservable at the time.

The outcome is that 3 out of 5 of the disintegrating systems from the DECam group and 2 out of 4 of the candidate systems from the ISIS group are likely to be genuine. From this I can deduce the contamination rate to be 4 out of 9 or 44.4%. Given these disintegrating multiple systems are not trivial to find, the contamination rate is acceptable. Even though numerical simulations predict that 50% to 95% of non-hierarchical triple systems and 10% of hierarchical triple systems undergo an ejection at some point in their evolution (e.g. Anosova, 1990; Valtonen et al., 2003), there are currently only 10 known disintegrating system candidates in the literature (Li et al., 2009). So, my 5 new promising candidates represent a 50% increase over the current population.

I will now briefly summarize the properties of the five genuine disintegrating systems. The first system consists of TYC 6813-1293-1, TYC 6813-286-1 and TYC 6813-643-1AB and could be at least a possible sextuple (due to one of the objects being in the Catalog of Accelerations and another object being a spectroscopic binary) i.e. a quadruple+binary disintegrating system. Next, the system consisting of TYC 9281-

3037-1, TYC 9281-2422-1 and TYC 9281-1175-1AB? could be a quadruple (one of the components needs confirmation that it is indeed part of this system) i.e. a triple+single star candidate disintegrating system. TYC 7731-1951-1, TYC 7731-2128-1AB and TYC 7731-1995-1ABC? is the third system and it could be a sextuple (due to one of the objects being in the Catalog of Accelerations and another component yet to be confirmed if it is indeed part of this system) i.e. a quintuple+single star candidate disintegrating multiple system. The fourth system consists of TYC 3023-1691-1, TYC 3024-1493-1 and TYC 3023-1688-1ABC? (one of the objects is yet to be confirmed as part of this system) and could be a quintuple i.e. a quadruple+single star candidate system. Finally, TYC 3440-338-1, TYC 3441-520-1 and TYC 3440-300-1AB is the fifth system which could be at least a sextuple (due to two of the components being in the Catalog of Accelerations) i.e. a quadruple+binary disintegrating system. Overall, there are 3 possible sextuples (2 of which are quadruple+binary systems and 1 is a quintuple+single star system), 1 quintuple and 1 quadruple candidate disintegrating systems.

Furthermore, it is even harder to find additional low-mass components that are missed by Gaia. After rigorous assessment with the aid of various CMDS, I identified a promising UCD candidate in one of the systems from the DECam sample. The system consists of TYC 7731-1951-1, TYC 7731-2128-1AB, and TYC 7731-1995-1ABC?, and began its possible disintegration approximately 9000 years ago. It includes a promising novel early L dwarf candidate, with a spectral type estimate in the range M8–L2. I have ruled out the presence of UCD candidates in the other 2 out of the 3 genuine systems followed up with DECam.

In addition, I also established a reliable method to use iSpec to measure the [Fe/H] and $v \sin i$ of AFGK stars. Using the ISIS spectra, I have also measured the RVs for all objects observed. The combination of validating as well as further study of these candidate disintegrating multiple systems could lead to the disclosure of the full range of components during disintegration, hence new constraints then can be placed on the typically unseen constituents of multiple systems. Moreover, the rate at which these disintegrating systems interact in the Galactic disk can be determined from the observed frequency of those disintegrators. Further, the identifiable disintegrating components in the low-mass range can be extended through supplementary analysis of longer wavelength observations (e.g. the data on the *Spitzer Heritage Archive*).

5.2 Future work

All 20 candidate disintegrating systems from both Group A and Group B would require follow-up observations to obtain high quality parallax, PM, RV, and [Fe/H] for all members that are currently lacking such measurements. RV monitoring or adaptive optics observations are desirable to verify if objects in the Catalogue of Acceleration are real binaries or multiple systems. Once the distance, PM and RV for all counterparts in these disintegrating systems have been acquired, by also obtaining the 3-D velocities, dynamical simulation then can be performed to provide additional confirmation of whether these candidate systems are in fact gravitationally unbound or not. Additional lower mass components could potentially be released as results of the dynamical interactions thus become detectable as they become widely separated from their original host. Hence, follow-up with even deeper observations, in particular of the 5 more promising disintegrating multiple systems, is necessary. A deep near-infrared imaging in the region of those candidate systems could aim to investigate if there are any/additional fainter ejected objects which were previously undetectable that are also involved in the disintegration process, i.e., T and Y dwarfs and even exoplanets.

It is also essential to confirm the nature, characterize as well as to obtain the RV measurement of the candidate UCD from the disintegrating system consisting of TYC 7731-1951-1, TYC 7731-2128-1AB and TYC 7731-1885-1ABC? by following it up with near-infrared spectroscopy. It may be also beneficial to obtain spectra for a few of the rejected UCD candidates, to make sure that the selection method is not removing real UCDs. Further, a good parallax measurement for the candidate UCD is also crucial in validating if it is indeed a part of this candidate disintegrating system.

Moreover, a continuous expansion to the existing list of candidate systems with even higher quality candidate systems would also be an imperative part of the future work, given that Gaia DR3 provides extremely accurate parallaxes and PMs for main-sequence stars and UCDs down to G=20.7 mag. For the selection of photometric UCD candidates, beyond the current surveys and facilities such as the UHS (Dye et al., 2018), PanSTARRS (Chambers et al., 2016), VHS (McMahon et al., 2013), WISE (Wright et al., 2010), UKIDSS (Lawrence et al., 2007) and SDSS (York et al., 2000), other infrared surveys will soon be available and can be used for a much larger sample of UCD companion/s that could be part of this new list of disintegrating systems, e.g. EUCLID (Laureijs et al., 2011; Euclid Collaboration et al., 2022) and the Nancy Grace Roman

Space Telescope (Spergel et al., 2013). LSST (Ivezić et al., 2019) will provide repeated observations for the candidate UCDs identified this way, and therefore allow me to measure their PM and parallaxes and determine if they are members of the system. SPHEREX (Korngut et al., 2018) will provide low-resolution spectra for the candidates, therefore enabling me to confirm the nature of the candidates and characterize them right away. Finally, NEOSurveyor (Kirkpatrick et al., 2019) will provide data at longer wavelengths, to search for even colder ejected components.

Overall, the combination of future large area surveys and facilities will greatly expand the possibility to identify disintegrating multiple systems, and will facilitate the identification and characterization of ejected low-mass components, therefore allowing for a more comprehensive study of the population of these intriguing objects.

Bibliography

Aarseth S. J., 2003, in Makino J., Hut P., eds, IAU Symposium Vol. 208, Astrophysical Supercomputing using Particle Simulations. p. 295 (arXiv:astro-ph/0110148)

Aarseth S. J., 2004, in Allen C., Scarfe C., eds, Revista Mexicana de Astronomia y Astrofisica Conference Series Vol. 21, Revista Mexicana de Astronomia y Astrofisica Conference Series. pp 156–162

Abbott T. M. C., et al., 2018, ApJS, 239, 18

Abt H. A., 1983, ARA&A, 21, 343

Adams F. C., Ruden S. P., Shu F. H., 1989, ApJ, 347, 959

Ahmic M., Jayawardhana R., Brandeker A., Scholz A., van Kerkwijk M. H., Delgado-Donate E., Froebrich D., 2007, ApJ, 671, 2074

Aitken R. G., 1935, The binary stars

Allard F., 2014, in Booth M., Matthews B. C., Graham J. R., eds, Vol. 299, Exploring the Formation and Evolution of Planetary Systems. pp 271–272, doi:10.1017/S1743921313008545

Allard F., Homeier D., Freytag B., Schaffenberger W., Rajpurohit A. S., 2013, Memorie della Societa Astronomica Italiana Supplementi, 24, 128

Allen P. R., 2007, ApJ, 668, 492

Allen D. M., Barbuy B., 2006, A&A, 454, 895

Allende Prieto C., 2010, in Cunha K., Spite M., Barbuy B., eds, Vol. 265, Chemical Abundances in the Universe: Connecting First Stars to Planets. pp 304–312 (arXiv:0911.3598), doi:10.1017/S1743921310000785

Almeida A., Monteiro H., Dias W. S., 2023, MNRAS,

Ammons S. M., Robinson S. E., Strader J., Laughlin G., Fischer D., Wolf A., 2006, ApJ, 638, 1004

Anderson E., Francis C., 2012, Astronomy Letters, 38, 331

Anosova J. P., 1989, Highlights of Astronomy, 8, 143

Anosova Z. P., 1990, Celestial Mechanics and Dynamical Astronomy, 48, 357

Antonov V. A., Latyshev I. N., 1972, in Chebotarev G. A., Kazimirchak-Polonskaia E. I., Marsden B. G., eds, Vol. 45, The Motion, Evolution of Orbits, and Origin of Comets. p. 341

Arenou F., et al., 2017, A&A, 599, A50

Armitage P. J., Bonnell I. A., 2002, MNRAS, 330, L11

Bailer-Jones C. A. L., Rybizki J., Andrae R., Fouesneau M., 2018, VizieR Online Data Catalog, pp J/A+A/616/A37

Basri G., Reiners A., 2006, AJ, 132, 663

Basri G., Marcy G. W., Graham J. R., 1996, ApJ, 458, 600

Bate M. R., 2012, MNRAS, 419, 3115

Becklin E. E., Zuckerman B., 1988, Nature, 336, 656

Bédard A., Bergeron P., Brassard P., Fontaine G., 2020, ApJ, 901, 93

Bensby T., Feltzing S., Lundström I., 2003, A&A, 410, 527

Bergeron P., et al., 2011, ApJ, 737, 28

Berriman G., Reid N., 1987, MNRAS, 227, 315

Best W. M. J., et al., 2018, ApJS, 234, 1

Best W. M. J., Liu M. C., Magnier E. A., Dupuy T. J., 2021, AJ, 161, 42

Blanco-Cuaresma S., 2019, MNRAS, 486, 2075

Blanco-Cuaresma S., Soubiran C., Heiter U., Jofré P., 2014, A&A, 569, A111

Blanton M. R., et al., 2017, AJ, 154, 28

Bodenheimer P., 1978, ApJ, 224, 488

Bodenheimer P., 1992, in Kondo Y., Sistero R., Polidan R. S., eds, Vol. 151, Evolutionary Processes in Interacting Binary Stars. p. 9

Bodenheimer P., Ruzmajkina T., Mathieu R. D., 1993, in Levy E. H., Lunine J. I., eds, Protostars and Planets III. p. 367

Bonnarel F., et al., 2000, A&AS, 143, 33

Boss A. P., 1986, ApJS, 62, 519

Boss A. P., 1988, Comments on Astrophysics, 12, 169

Boss A. P., 1991, Nature, 351, 298

Boss A. P., 1993, in Sahade J., McCluskey G. E., Kondo Y., eds, Astrophysics and Space Science Library Vol. 177, Astrophysics and Space Science Library. p. 355, doi:10.1007/978-94-011-2416-4˙19

Bouy H., Brandner W., Martín E. L., Delfosse X., Allard F., Basri G., 2003, AJ, 126, 1526

Brandt T. D., 2021, ApJS, 254, 42

Brandt T. D., Dupuy T. J., Bowler B. P., 2019, AJ, 158, 140

Buder S., et al., 2018, MNRAS, 478, 4513

Buder S., et al., 2021, MNRAS, 506, 150

Burgasser A. J., et al., 2000, ApJ, 531, L57

Burgasser A. J., Kirkpatrick J. D., Reid I. N., Brown M. E., Miskey C. L., Gizis J. E., 2003a, ApJ, 586, 512

Burgasser A. J., Kirkpatrick J. D., Liebert J., Burrows A., 2003b, ApJ, 594, 510

Burgasser A. J., Kirkpatrick J. D., Lowrance P. J., 2005, AJ, 129, 2849

Burgasser A. J., Geballe T. R., Leggett S. K., Kirkpatrick J. D., Golimowski D. A., 2006, ApJ, 637, 1067

Burgasser A. J., Reid I. N., Siegler N., Close L., Allen P., Lowrance P., Gizis J., 2007, in Reipurth B., Jewitt D., Keil K., eds, Protostars and Planets V. p. 427 (arXiv:astro-ph/0602122), doi:10.48550/arXiv.astro-ph/0602122

Burgasser A. J., Cruz K. L., Cushing M., Gelino C. R., Looper D. L., Faherty J. K., Kirkpatrick J. D., Reid I. N., 2010, ApJ, 710, 1142

Burkert A., Bodenheimer P., 1996, MNRAS, 280, 1190

Burningham B., et al., 2009, MNRAS, 395, 1237

Burningham B., et al., 2013, MNRAS, 433, 457

Burrows A., Hubbard W. B., Lunine J. I., Liebert J., 2001, Reviews of Modern Physics, 73, 719

Burrows A., Sudarsky D., Lunine J. I., 2003, ApJ, 596, 587

Caballero J. A., 2010, A&A, 514, A98

Caballero J. A., Martín E. L., Dobbie P. D., Barrado Y Navascués D., 2006, A&A, 460, 635

Casali M., et al., 2007, A&A, 467, 777

Casewell S. L., Dobbie P. D., Hodgkin S. T., Moraux E., Jameson R. F., Hambly N. C., Irwin J., Lodieu N., 2007, MNRAS, 378, 1131

Casewell S. L., et al., 2012, ApJ, 759, L34

Chabrier G., 2005, in Corbelli E., Palla F., Zinnecker H., eds, Astrophysics and Space Science Library Vol. 327, The Initial Mass Function 50 Years Later. p. 41 (arXiv:astro-ph/0409465), doi:10.1007/978-1-4020-3407-7˙5

Chabrier G., Baraffe I., 2000, ARA&A, 38, 337

Chambers K. C., et al., 2016, arXiv e-prints, p. arXiv:1612.05560

Choi J., Dotter A., Conroy C., Cantiello M., Paxton B., Johnson B. D., 2016, ApJ, 823, 102

Chulkov D., Malkov O., 2022, MNRAS, 517, 2925

Clarke C. J., Pringle J. E., 1991a, MNRAS, 249, 584

Clarke C. J., Pringle J. E., 1991b, MNRAS, 249, 588

Close L. M., et al., 2007, ApJ, 660, 1492

Cummings J. D., Kalirai J. S., Tremblay P. E., Ramirez-Ruiz E., Choi J., 2018, ApJ, 866, 21

Cushing M. C., et al., 2011, ApJ, 743, 50

Cutri R. M., et al., 2013, Explanatory Supplement to the AllWISE Data Release Products, Explanatory Supplement to the AllWISE Data Release Products, by R. M. Cutri et al.

Day-Jones A. C., 2009, PhD thesis, University of Hertfordshire, UK

Day-Jones A. C., et al., 2011, MNRAS, 410, 705

De Rosa R. J., et al., 2014, MNRAS, 437, 1216

Deacon N. R., et al., 2014, ApJ, 792, 119

Delorme P., Lagrange A. M., Chauvin G., Bonavita M., Lacour S., Bonnefoy M., Ehrenreich D., Beust H., 2012, A&A, 539, A72

Dupuy T. J., Liu M. C., 2012, ApJS, 201, 19

Dupuy T. J., Liu M. C., 2017, ApJS, 231, 15

Dupuy T. J., Liu M. C., Bowler B. P., Cushing M. C., Helling C., Witte S., Hauschildt P., 2010, ApJ, 721, 1725

Duquennoy A., Mayor M., 1991, A&A, 248, 485

Durisen R. H., Gingold R. A., Tohline J. E., Boss A. P., 1986, ApJ, 305, 281

Dye S., et al., 2018, MNRAS, 473, 5113

Edge A., Sutherland W., Kuijken K., Driver S., McMahon R., Eales S., Emerson J. P., 2013, The Messenger, 154, 32

Eisenhardt P. R. M., et al., 2020, ApJS, 247, 69

Eisenstein D. J., et al., 2011, AJ, 142, 72

El-Badry K., Rix H.-W., 2018, MNRAS, 480, 4884

El-Badry K., Rix H.-W., Heintz T. M., 2021, MNRAS, 506, 2269

Elliott P., Bayo A., 2016, MNRAS, 459, 4499

Euclid Collaboration et al., 2022, A&A, 662, A112

Faherty J. K., Burgasser A. J., West A. A., Bochanski J. J., Cruz K. L., Shara M. M., Walter F. M., 2010, AJ, 139, 176

Faherty J. K., Beletsky Y., Burgasser A. J., Tinney C., Osip D. J., Filippazzo J. C., Simcoe R. A., 2014, ApJ, 790, 90

Faherty J. K., et al., 2016, ApJS, 225, 10

Faigler S., Mazeh T., 2011, MNRAS, 415, 3921

Fekel F. C. J., 1981, ApJ, 246, 879

Fischer D. A., Marcy G. W., 1992, ApJ, 396, 178

Flaugher B., et al., 2015, AJ, 150, 150

Flewelling H. A., et al., 2020, ApJS, 251, 7

Fontaine G., Brassard P., Bergeron P., 2001, PASP, 113, 409

For B. Q., et al., 2010, ApJ, 708, 253

Fouchard M., Froeschlé C., Valsecchi G., Rickman H., 2006, Celestial Mechanics and Dynamical Astronomy, 95, 299

Fouesneau M., et al., 2022, arXiv e-prints, p. arXiv:2206.05992

Fregeau J. M., Cheung P., Portegies Zwart S. F., Rasio F. A., 2004, MNRAS, 352, 1

French J. R., Casewell S. L., Dupuy T. J., Debes J. H., Manjavacas E., Martin E. C., Xu S., 2023, MNRAS, 519, 5008

Gagné J., Lafrenière D., Doyon R., Malo L., Artigau É., 2014, ApJ, 783, 121

Gagné J., Lafrenière D., Doyon R., Malo L., Artigau É., 2015, ApJ, 798, 73

Gagné J., et al., 2018, ApJ, 856, 23

Gagné J., Moranta L., Faherty J. K., Kiman R., Couture D., Larochelle A. R., Popinchalk M., Morrone D., 2023, ApJ, 945, 119

Gaia Collaboration et al., 2016a, A&A, 595, A1

Gaia Collaboration et al., 2016b, A&A, 595, A2

Gaia Collaboration et al., 2018a, A&A, 616, A1

Gaia Collaboration et al., 2018b, A&A, 616, A1

Gaia Collaboration et al., 2021, A&A, 649, A1

Gaia Collaboration et al., 2022a, arXiv e-prints, p. arXiv:2206.05595

Gaia Collaboration et al., 2022b, arXiv e-prints, p. arXiv:2208.00211

Gardner J. P., et al., 2006, Space Sci. Rev., 123, 485

Geballe T. R., et al., 2002, ApJ, 564, 466

Georgakarakos N., 2008, Celestial Mechanics and Dynamical Astronomy, 100, 151

Gizis J. E., Kirkpatrick J. D., Wilson J. C., 2001a, AJ, 121, 2185

Gizis J. E., Kirkpatrick J. D., Burgasser A., Reid I. N., Monet D. G., Liebert J., Wilson J. C., 2001b, ApJ, 551, L163

Glebocki R., Gnacinski P., 2005, VizieR Online Data Catalog, p. III/244

Gliese W., Jahreiß H., 1979, A&AS, 38, 423

Gray R. O., 1999, SPECTRUM: A stellar spectral synthesis program, Astrophysics Source Code Library, record ascl:9910.002 (ascl:9910.002)

Guenther E. W., Wuchterl G., 2003, A&A, 401, 677

Gustafsson B., Edvardsson B., Eriksson K., Jørgensen U. G., Nordlund Å., Plez B., 2008, A&A, 486, 951

Guszejnov D., Hopkins P. F., 2015, MNRAS, 450, 4137

Guszejnov D., Hopkins P. F., Krumholz M. R., 2017, MNRAS, 468, 4093

Hacar A., Tafalla M., Kauffmann J., Kovács A., 2013, A&A, 554, A55

Halbwachs J. L., 1987, A&A, 183, 234

Harrison T. E., Howell S. B., Huber M. E., Osborne H. L., Holtzman J. A., Cash J. L., Gelino D. M., 2003, AJ, 125, 2609

Hartman Z. D., Lépine S., 2020, ApJS, 247, 66

Hawkins K., et al., 2020, MNRAS, 492, 1164

Heggie D. C., 1975, MNRAS, 173, 729

Heisler J., Tremaine S., 1986, , 65, 13

Heller C. H., 1991, PhD thesis, Yale University, Connecticut

Helling C., Casewell S., 2014, A&A Rev., 22, 80

Helling C., Dehn M., Woitke P., Hauschildt P. H., 2008, ApJ, 675, L105

Hills J. G., 1976, MNRAS, 175, 1P

Hills J. G., Day C. A., 1976, Astrophys. Lett., 17, 87

Hinkle K., Wallace L., Valenti J., Harmer D., 2000, Visible and Near Infrared Atlas of the Arcturus Spectrum 3727-9300 A

Hiranaka K., Cruz K. L., Douglas S. T., Marley M. S., Baldassare V. F., 2016, ApJ, 830, 96

Houk N., 1978, Michigan catalogue of two-dimensional spectral types for the HD stars

Houk N., 1982, Michigan Catalogue of Two-dimensional Spectral Types for the HD stars. Volume_3. Declinations -40_f0 to -26_f0.

Houk N., Smith-Moore M., 1988, Michigan Catalogue of Two-dimensional Spectral Types for the HD Stars. Volume 4, Declinations -26°.0 to -12°.0.. Vol. 4

Hubbard W. B., 1977, , 30, 305

Hurley J. R., Tout C. A., Pols O. R., 2002, MNRAS, 329, 897

Ivezić Ž., et al., 2019, ApJ, 873, 111

Jeans J. H., 1919, Problems of cosmogony and stellar dynamics

Jeans J. H., 1929, The universe around us

Joergens V., 2006, A&A, 446, 1165

Joergens V., 2008, A&A, 492, 545

Jofré P., et al., 2014, A&A, 564, A133

Jofré P., Heiter U., Tucci Maia M., Soubiran C., Worley C. C., Hawkins K., Blanco-Cuaresma S., Rodrigo C., 2018, Research Notes of the American Astronomical Society, 2, 152

Jönsson H., et al., 2020, AJ, 160, 120

Kirk B., et al., 2016, AJ, 151, 68

Kirkpatrick J. D., 2005, ARA&A, 43, 195

Kirkpatrick J. D., 2008, in van Belle G., ed., Astronomical Society of the Pacific Conference Series Vol. 384, 14th Cambridge Workshop on Cool Stars, Stellar Systems, and the Sun. p. 85 (arXiv:0704.1522), doi:10.48550/arXiv.0704.1522

Kirkpatrick J. D., Henry T. J., McCarthy Donald W. J., 1991, ApJS, 77, 417

Kirkpatrick J. D., Henry T. J., Liebert J., 1993, ApJ, 406, 701

Kirkpatrick J. D., et al., 1999, ApJ, 519, 802

Kirkpatrick J. D., et al., 2011, ApJS, 197, 19

Kirkpatrick J. D., et al., 2012, ApJ, 753, 156

Kirkpatrick J. D., et al., 2019, BAAS, 51, 108

Kirkpatrick J. D., et al., 2021, ApJS, 253, 7

Kley W., Dirksen G., 2006, A&A, 447, 369

Kobulnicky H. A., Fryer C. L., 2007, ApJ, 670, 747

Konopacky Q. M., Ghez A. M., Barman T. S., Rice E. L., Bailey J. I. I., White R. J., McLean I. S., Duchêne G., 2010, ApJ, 711, 1087

Kordopatis G., et al., 2011, A&A, 535, A107

Korngut P. M., et al., 2018, in Lystrup M., MacEwen H. A., Fazio G. G., Batalha N., Siegler N., Tong E. C., eds, Society of Photo-Optical Instrumentation Engineers (SPIE) Conference Series Vol. 10698, Space Telescopes and Instrumentation 2018: Optical, Infrared, and Millimeter Wave. p. 106981U, doi:10.1117/12.2312860

Kunder A., et al., 2017, AJ, 153, 75

Kurosawa R., Harries T. J., Littlefair S. P., 2006, MNRAS, 372, 1879

Kurucz R. L., 2005, Memorie della Societa Astronomica Italiana Supplementi, 8, 14

Kurucz R. L., 2017, ATLAS9: Model atmosphere program with opacity distribution functions, Astrophysics Source Code Library, record ascl:1710.017 (ascl:1710.017)

Lada C. J., 2006, ApJ, 640, L63

Larson R. B., 1990, in Capuzzo-Dolcetta R., Chiosi C., di Fazio A., eds, Astrophysics and Space Science Library Vol. 162, Physical Processes in Fragmentation and Star Formation. pp 389–399, doi:10.1007/978-94-009-0605-1˙34

Lattanzi M. G., Casertano S., Jancart S., Morbidelli R., Pourbaix D., Pannunzio R., Sozzetti A., Spagna A., 2005, in Turon C., O'Flaherty K. S., Perryman M. A. C., eds, ESA Special Publication Vol. 576, The Three-Dimensional Universe with Gaia. p. 251

Lattanzio J. C., Henriksen R. N., 1988, MNRAS, 232, 565

Laureijs R., et al., 2011, arXiv e-prints, p. arXiv:1110.3193

Lawrence A., et al., 2007, MNRAS, 379, 1599

Leggett S. K., et al., 2008, ApJ, 682, 1256

Li P. J., Fu Y. N., Sun Y. S., 2009, A&A, 504, 277

Liebert J., Boroson T. A., Giampapa M. S., 1984, ApJ, 282, 758

Lindblad B., 1925, Arkiv for Matematik, Astronomi och Fysik, 21, 1

Lodieu N., Dobbie P. D., Hambly N. C., 2011, A&A, 527, A24

Lubow S. H., Seibert M., Artymowicz P., 1999, ApJ, 526, 1001

Lucas P. W., Roche P. F., Tamura M., 2005, MNRAS, 361, 211

Lucas P. W., et al., 2010, MNRAS, 408, L56

Luhman K. L., McLeod K. K., Goldenson N., 2005, ApJ, 623, 1141

Luhman K. L., Burgasser A. J., Bochanski J. J., 2011, ApJ, 730, L9

Luo A. L., Zhao Y. H., Zhao G., et al. 2019, VizieR Online Data Catalog, p. V/164

Ma B., Ge J., 2014, MNRAS, 439, 2781

Mainzer A., et al., 2011, ApJ, 731, 53

Majewski S. R., et al., 2017, AJ, 154, 94

Malkov O. Y., Tamazian V. S., Docobo J. A., Chulkov D. A., 2012, A&A, 546, A69

Malmberg D., de Angeli F., Davies M. B., Church R. P., Mackey D., Wilkinson M. I., 2007, MNRAS, 378, 1207

Marchal C., 1990, The three-body problem. Elsevier

Marley M. S., Leggett S. K., 2009, in Astrophysics in the Next Decade. p. 101 (arXiv:0803.1476), doi:10.1007/978-1-4020-9457-6˙4

Marocco F., et al., 2021, ApJS, 253, 8

Martell S. L., et al., 2017, MNRAS, 465, 3203

Martín E. L., Brandner W., Bouvier J., Luhman K. L., Stauffer J., Basri G., Zapatero Osorio M. R., Barrado y Navascués D., 2000, ApJ, 543, 299

Martín E. L., Barrado y Navascués D., Baraffe I., Bouy H., Dahm S., 2003, ApJ, 594, 525

Mathieu R. D., 1992, in Kondo Y., Sistero R., Polidan R. S., eds, Vol. 151, Evolutionary Processes in Interacting Binary Stars. p. 21

Maxted P. F. L., Jeffries R. D., 2005, MNRAS, 362, L45

Maxted P. F. L., Marsh T. R., North R. C., 2000, MNRAS, 317, L41

Maxted P. F. L., Marsh T. R., Heber U., Morales-Rueda L., North R. C., Lawson W. A., 2002, MNRAS, 333, 231

Maxted P. F. L., Jeffries R. D., Oliveira J. M., Naylor T., Jackson R. J., 2008, MNRAS, 385, 2210

Mazeh T., 2008, in Goupil M. J., Zahn J. P., eds, EAS Publications Series Vol. 29, EAS Publications Series. pp 1–65 (arXiv:0801.0134), doi:10.1051/eas:0829001

McDonald I., et al., 2021, MNRAS, 505, 5584

McLean I. S., McGovern M. R., Burgasser A. J., Kirkpatrick J. D., Prato L., Kim S. S., 2003, ApJ, 596, 561

McMahon R. G., Banerji M., Gonzalez E., Koposov S. E., Bejar V. J., Lodieu N., Rebolo R., VHS Collaboration 2013, The Messenger, 154, 35

McMahon R. G., Banerji M., Gonzalez E., Koposov S. E., Bejar V. J., Lodieu N., Rebolo R., VHS Collaboration 2021, VizieR Online Data Catalog, p. II/367

Meisner A. M., et al., 2020a, ApJ, 889, 74

Meisner A. M., et al., 2020b, ApJ, 899, 123

Michalik D., Lindegren L., Hobbs D., 2015, A&A, 574, A115

Mikkola S., 1983, MNRAS, 203, 1107

Miyama S. M., Hayashi C., Narita S., 1984, ApJ, 279, 621

Moe M., Di Stefano R., 2017, ApJS, 230, 15

Moeckel N., Veras D., 2012, MNRAS, 422, 831

Mohanty S., Basri G., Jayawardhana R., Allard F., Hauschildt P., Ardila D., 2004a, ApJ, 609, 854

Mohanty S., Jayawardhana R., Basri G., 2004b, ApJ, 609, 885

Monaghan J. J., Lattanzio J. C., 1984, , 5, 493

Moon B., Jeong D.-G., Oh S., Sohn J., 2017, Journal of Astronomy and Space Sciences, 34, 99

Morgan W. W., Keenan P. C., Kellman E., 1943, An atlas of stellar spectra, with an outline of spectral classification

Morley C. V., Fortney J. J., Marley M. S., Visscher C., Saumon D., Leggett S. K., 2012, ApJ, 756, 172

Morley C. V., Marley M. S., Fortney J. J., Lupu R., Saumon D., Greene T., Lodders K., 2014, ApJ, 787, 78

Morris S. L., 1985, ApJ, 295, 143

Mróz P., et al., 2020, ApJ, 903, L11

Munari U., et al., 2014, AJ, 148, 81

Nakajima T., Oppenheimer B. R., Kulkarni S. R., Golimowski D. A., Matthews K., Durrance S. T., 1995, Nature, 378, 463

Nelson R. P., 2018, in Deeg H. J., Belmonte J. A., eds, , Handbook of Exoplanets. p. 139, doi:10.1007/978-3-319-55333-7˙139

Niedzielski A., Deka-Szymankiewicz B., Adamczyk M., Adamów M., Nowak G., Wolszczan A., 2016, A&A, 585, A73

Niu Z., Yuan H., Wang S., Liu J., 2021, ApJ, 922, 211

Offner S. S. R., Moe M., Kratter K. M., Sadavoy S. I., Jensen E. L. N., Tobin J. J., 2022, arXiv e-prints, p. arXiv:2203.10066

Oppenheimer B. R., Kulkarni S. R., Matthews K., van Kerkwijk M. H., 1998, ApJ, 502, 932

Paegert M., Stassun K. G., Collins K. A., Pepper J., Torres G., Jenkins J., Twicken J. D., Latham D. W., 2022, VizieR Online Data Catalog, p. IV/39

Patience J., Ghez A. M., Reid I. N., Matthews K., 2002, AJ, 123, 1570

Pavlenko Y. V., Jenkins J. S., Jones H. R. A., Ivanyuk O., Pinfield D. J., 2012, MNRAS, 422, 542

Pearce L. A., Kraus A. L., Dupuy T. J., Mann A. W., Newton E. R., Tofflemire B. M., Vanderburg A., 2020, ApJ, 894, 115

Pecaut M. J., Mamajek E. E., 2013, ApJS, 208, 9

Penoyre Z., Belokurov V., Evans N. W., 2022, MNRAS, 513, 5270

Perryman M. A. C., et al., 1997, A&A, 500, 501

Pickles A., Depagne É., 2010, PASP, 122, 1437

Pinfield D. J., Dobbie P. D., Jameson R. F., Steele I. A., Jones H. R. A., Katsiyannis A. C., 2003, MNRAS, 342, 1241

Pinfield D. J., Jones H. R. A., Lucas P. W., Kendall T. R., Folkes S. L., Day-Jones A. C., Chappelle R. J., Steele I. A., 2006, MNRAS, 368, 1281

Pinfield D. J., et al., 2012, MNRAS, 422, 1922

Piskunov N., Valenti J. A., 2017, A&A, 597, A16

Piskunov N. E., Kupka F., Ryabchikova T. A., Weiss W. W., Jeffery C. S., 1995, A&AS, 112, 525

Plez B., 2012, Turbospectrum: Code for spectral synthesis, Astrophysics Source Code Library, record ascl:1205.004 (ascl:1205.004)

Pols O. R., Tout C. A., Schroder K.-P., Eggleton P. P., Manners J., 1997, MNRAS, 289, 869

Prantzos N., 2008, A&A, 489, 525

Pringle J. E., 1989, MNRAS, 239, 361

Prša A., et al., 2011, AJ, 141, 83

Raghavan D., et al., 2010, ApJS, 190, 1

Rasio F. A., Ford E. B., 1996, Science, 274, 954

Rebolo R., Zapatero Osorio M. R., Martín E. L., 1995, Nature, 377, 129

Rebolo R., Martin E. L., Basri G., Marcy G. W., Zapatero-Osorio M. R., 1996, ApJ, 469, L53

Reed M. D., et al., 2010, Ap&SS, 329, 83

Reid I. N., Gizis J. E., 1997, AJ, 113, 2246

Reid I. N., Burgasser A. J., Cruz K. L., Kirkpatrick J. D., Gizis J. E., 2001, AJ, 121, 1710

Reid I. N., Kirkpatrick J. D., Liebert J., Gizis J. E., Dahn C. C., Monet D. G., 2002, AJ, 124, 519

Reipurth B., 2000, AJ, 120, 3177

Retterer J. M., King I. R., 1982, ApJ, 254, 214

Robin A. C., et al., 2012, A&A, 543, A100

Roeser S., Bastian U., 1988, A&AS, 74, 449

Ruzmaikina T. V., 1981a, Advances in Space Research, 1, 49

Ruzmaikina T. V., 1981b, Soviet Astronomy Letters, 7, 104

Rybicki G. B., Lightman A. P., 1979, Radiative processes in astrophysics

Saslaw W. C., Valtonen M. J., Aarseth S. J., 1974, ApJ, 190, 253

Sasselov D. D., Rucinski S. M., 1990, ApJ, 351, 578

Saumon D., Marley M. S., 2008, ApJ, 689, 1327

Saumon D., Bergeron P., Lunine J. I., Hubbard W. B., Burrows A., 1994, ApJ, 424, 333

Saumon D., Marley M. S., Abel M., Frommhold L., Freedman R. S., 2012, ApJ, 750, 74

Shanks T., et al., 2015, MNRAS, 451, 4238

Shu F. H., Tremaine S., Adams F. C., Ruden S. P., 1990, ApJ, 358, 495

Skrutskie M. F., et al., 2006, AJ, 131, 1163

Skrzypek N., Warren S. J., Faherty J. K., Mortlock D. J., Burgasser A. J., Hewett P. C., 2015, A&A, 574, A78

Smalley B., 2005, Memorie della Societa Astronomica Italiana Supplementi, 8, 130

Sneden C., Bean J., Ivans I., Lucatello S., Sobeck J., 2012, MOOG: LTE line analysis and spectrum synthesis, Astrophysics Source Code Library, record ascl:1202.009 (ascl:1202.009)

Söderhjelm S., 1999, A&A, 341, 121

Soubiran C., Le Campion J. F., Cayrel de Strobel G., Caillo A., 2010, A&A, 515, A111

Soubiran C., Le Campion J.-F., Brouillet N., Chemin L., 2016a, A&A, 591, A118

Soubiran C., Le Campion J.-F., Brouillet N., Chemin L., 2016b, A&A, 591, A118

Spergel D., et al., 2013, arXiv e-prints, p. arXiv:1305.5425

Stamatellos D., Herczeg G. J., 2015, MNRAS, 449, 3432

Stamatellos D., Hubber D. A., Whitworth A. P., 2007, MNRAS, 382, L30

Stamatellos D., Whitworth A. P., Hubber D. A., 2012, MNRAS, 427, 1182

Stauffer J. R., Hamilton D., Probst R. G., 1994, AJ, 108, 155

Steele P., Burleigh M., Barstow M., Jameson R., Dobbie P., 2009, in Journal of Physics Conference Series. p. 012058, doi:10.1088/1742-6596/172/1/012058

Steinmetz M., et al., 2006, AJ, 132, 1645

Steinmetz M., et al., 2020a, AJ, 160, 82

Steinmetz M., et al., 2020b, AJ, 160, 83

Stetson P. B., 1987, PASP, 99, 191

Strom S., 1991, S&T, 82, 18

Struve O., Huang S. S., 1958, Spectroscopic Binaries. Springer Berlin Heidelberg, Berlin, Heidelberg, pp 243–273, doi:10.1007/978-3-642-45906-1˙8, https://doi.org/10.1007/978-3-642-45906-1_8

Szebehely V., 1972, AJ, 77, 169

Tal-Or L., Faigler S., Mazeh T., 2015, in European Physical Journal Web of Conferences. p. 06063 (arXiv:1410.3074), doi:10.1051/epjconf/201510106063

Tassoul J.-L., 1978, Theory of rotating stars

Taylor M. B., 2005, in Shopbell P., Britton M., Ebert R., eds, Astronomical Society of the Pacific Conference Series Vol. 347, Astronomical Data Analysis Software and Systems XIV. p. 29

Tody D., 1986, in Crawford D. L., ed., Society of Photo-Optical Instrumentation Engineers (SPIE) Conference Series Vol. 627, Instrumentation in astronomy VI. p. 733, doi:10.1117/12.968154

Toonen S., Hamers A., Portegies Zwart S., 2016, Computational Astrophysics and Cosmology, 3, 6

Torres G., 1992, PASP, 104, 1108

Tremblay P. E., Bergeron P., Gianninas A., 2011, ApJ, 730, 128

Tsantaki M., et al., 2022, A&A, 659, A95

Udry S., Santos N. C., 2007, ARA&A, 45, 397

Valdes F., Gruendl R., DES Project 2014, in Manset N., Forshay P., eds, Astronomical Society of the Pacific Conference Series Vol. 485, Astronomical Data Analysis Software and Systems XXIII. p. 379

Valenti J. A., Piskunov N., 1996, A&AS, 118, 595

Valtonen M. J., Mülläri A. A., Orlov V. V., Rubinov A. V., 2003, Astronomy Letters, 29, 41

Veras D., Tout C. A., 2012, MNRAS, 422, 1648

Veras D., Crepp J. R., Ford E. B., 2009, ApJ, 696, 1600

Veras D., Evans N. W., Wyatt M. C., Tout C. A., 2014, MNRAS, 437, 1127

Vieira K., Korchagin V., Carraro G., Lutsenko A., 2023, Galaxies, 11, 77

Wang C., Huang Y., Yuan H., Zhang H., Xiang M., Liu X., 2022, ApJS, 259, 51

Ward-Duong K., et al., 2015, MNRAS, 449, 2618

Weinberg M. D., Shapiro S. L., Wasserman I., 1987, ApJ, 312, 367

Wootten A., 1989, ApJ, 337, 858

Wright E. L., et al., 2010, AJ, 140, 1868

Xiang M., et al., 2019, ApJS, 245, 34

Yip A. K. P., Pinfield D. J., Kurtev R., Gromadzki M., Marocco F., 2016, in 19th Cambridge Workshop on Cool Stars, Stellar Systems, and the Sun (CS19). Cambridge Workshop on Cool Stars, Stellar Systems, and the Sun. p. 137 (arXiv:1608.00888), doi:10.5281/zenodo.59237

Yip A. K. P., Kurtev R., Pinfield D. J., Marocco F., Gromadzki M., Carballo-Bello J. A., 2023, MNRAS, 522, 1669

York D. G., et al., 2000, AJ, 120, 1579

Zacharias N., Finch C. T., Girard T. M., Henden A., Bartlett J. L., Monet D. G., Zacharias M. I., 2013, AJ, 145, 44

Zapolsky H. S., Salpeter E. E., 1969, ApJ, 158, 809

Zhang Z. H., et al., 2010, MNRAS, 404, 1817

Zhang Z. H., Burgasser A. J., Gálvez-Ortiz M. C., Lodieu N., Zapatero Osorio M. R., Pinfield D. J., Allard F., 2019, MNRAS, 486, 1260

Zieliński P., Niedzielski A., Wolszczan A., Adamów M., Nowak G., 2012, A&A, 547, A91

dal Ponte M., et al., 2020, MNRAS, 499, 5302

van Leeuwen F., 2007, Hipparcos, the New Reduction of the Raw Data. Astrophysics and Space Science Library Vol. 350, Springer Science+Business Media B.V., doi:10.1007/978-1-4020-6342-8

van den Berk J., Portegies Zwart S. F., McMillan S. L. W., 2007, MNRAS, 379, 111